

UNIVERSITÀ DEGLI STUDI DI PADOVA

INDUSTRIAL ENGINEERING DIPARTMENT

MASTER'S DEGREE IN CHEMICAL AND

INDUSTRIAL PROCESSES ENGINEERING

**Master's Degree Thesis in Chemical and Industrial
Processes Engineering**

Development and Implementation of Techniques to
Characterize Solid Oxide Fuel Cells

Supervisor: Prof. Paolo Canu

Student: Gisela Auxiliadora Cepeda Arque

ACADEMIC YEAR 2016 – 2017

UNIVERSITÀ DEGLI STUDI DI PADOVA
DIPARTIMENTO DI INGEGNERIA INDUSTRIALE
CORSO DI LAUREA MAGISTRALE IN INGEGNERIA CHIMICA E
DEI PROCESSI INDUSTRIALI

Tesi di Laurea Magistrale in
Ingegneria Chimica e dei Processi Industriali

Sviluppo e Applicazione di Tecniche per la Caratterizzazione
di Celle a Combustibili Ceramiche

Relatore: Prof. Paolo Canu

Laureanda: Gisela Auxiliadora Cepeda Arque

ANNO ACCADEMICO 2016 – 2017

Riassunto

Uno dei più grandi problemi della società odierna è la necessità di trovare fonti alternative di energia a quelle attualmente a disposizione. Oltre alla sua limitata quantità, i combustibili fossili rilasciano anche dei gas che non solo sono pericolosi per la salute ma contribuiscono anche all'effetto serra.

Negli ultimi anni diverse proposte sono state considerate per la produzione di energia pulita. Tra queste si possono trovare le così dette fuel cell o celle combustibili, dispositivi capaci di erogare energia tramite una reazione chimica che avviene al suo interno.

Il presente studio pretende di rivisitare delle tecniche e dei materiali per un certo tipo di FC: celle combustibili ceramiche (SOFC). Rispetto ad altre tipologie di celle combustibili, le SOFC offrono dei vantaggi considerevoli. Tuttavia, limitazioni sulla scelta dei materiali e le alte temperature (800°C-900°C) a cui operano rendono difficoltoso il loro uso.

Lo scopo di questa indagine è l'analisi di nuovi materiali ceramici che presentino proprietà paragonabili a quelle già esistenti, ma che lavorano a temperature più basse (500°C-600°C), così da poter superare i problemi sopra riportati.

Per raggiungere l'obiettivo sono state usate due tecniche di utilizzo comune per la caratterizzazione delle FC. La prima parte di questo lavoro prevede l'uso della spettroscopia elettrochimica d'impedenza per valutare come variano diversi fenomeni di reazione all'interno delle celle, mentre la seconda parte comprende misure di conducibilità ionica sui medesimi materiali a diverse temperature.

Sebbene queste due tecniche sono di gran lunga conosciute, i metodi presentati in seguito rappresentano delle alternative alle applicazioni più tradizionali.

Abstract

One of the biggest problems of today's society is the need of finding alternative energy resources to those currently available. Besides their limited quantity, fossil fuels release gases that are not only noxious to human health but also contribute to the greenhouse effect.

During the last years, different proposals have been considered for the production of green energy. Among them fuel cells, devices capable of producing energy due to a reaction taking place within them, can be found.

The present study aims to revisit techniques and materials for a certain type of FC: solid oxide fuel cells (SOFC). With respect to other types of fuel cells, SOFCs offer considerable advantages. Yet, the limitation when it comes to materials selection and the high temperatures (800°C-900°C) at which they work render difficult their usage.

The purpose of this investigation is the analysis of new ceramic materials having similar properties to those already in existence, but working at lower temperatures (500°C-600°C) in order to overcome the aforementioned problems.

In order to reach this objective, diverse common techniques were used for the characterization of the FC. The first part of this work case envisages the use of electrochemical impedance spectroscopy to evaluate how different phenomena vary while a reaction is taking place, while the second part consists in ionic conductivity measurements at different temperatures.

Even if these two techniques are well known, the methods that will be followed-up represent a new alternative to the most traditional applications.

Index

INTRODUCTION	1
1.1 Fuel and Electrolytic Cells.....	1
1.1.1 Overview	1
1.1.2 Thermodynamic considerations in a Fuel Cell:.....	4
1.2 Solid Oxide Fuel Cells (SOFC)	5
1.3 Materials for Cell Components.....	8
1.3.1 Electrolytes.....	8
1.3.2 Cathodes	11
1.3.3 Anodes.....	13
1.4 Mixed Ionic and Electronic Conductivity (MIEC)	15
1.4.1 MIEC Principles	15
1.4.2 Ionic Conductivity from Literature	17
TECHNIQUES AND INSTRUMENTATION	20
2.1 Elecetrochemical Impedance Spectroscopy - EIS	20
2.1.1 Introduction to EIS	20
2.1.2 Data Presentation.....	22
2.1.3 Data Interpretation: The Electrical Equivalent Circuit Theorem	24
2.2 Equipment for EIS Data Acquisition	27
2.2.1 Traditional Instrumentation.....	27
2.2.2 Electronic Load as a Measurement Alternative	30
2.3 Ionic Conductivity Measurements	34
2.3.1 Conductivity in MIEC Materials.....	34
2.3.2 Permeation Cell Setup.....	36
2.3.3 Principles of Gas Chromatography	38
EXPERIMENTAL AND RESULTS.....	41
3.1 Implementation of EIS using an E-load.....	41
3.1.1 Validation of the Method through Synthetic Waves.....	41
3.2 Real Systems Measurements	48
3.2.1 Analysis of Real Circuital Elements	48
3.2.2 Analysis on Batteries.....	53

3.2.3 EIS analysis of SOFC with novel materials	55
3.2 Conductibility Measurements	82
3.2.1 Gas Chromatography Setup	82
3.2.2 Experimental Measurements and its Problematics.....	85
CONCLUSIONS	88
CONCLUSIONI.....	89
NOMENCLATURE AND ABBREVIATIONS	90
BIBLIOGRAPHY	93
APPENDIX A.....	96
EIS_test.....	96
freqrespmeasure	97
Impedenza.....	99
EIS_measurement_1	100
Model.....	106

CHAPTER 1

INTRODUCTION

1.1 Fuel and Electrolytic Cells

1.1.1 Overview

During the last decades, fuel cells have been one of the most researched devices as an alternative form of energy production. The necessity of finding sources different from those deriving from fossil fuel is diverse in motives. Among them there is undoubtedly the finite fossil fuel resource available and the environmental pollution created by its use. Combustion of fossil fuel releases dangerous gases for the environment that are harmful for the human health and that at the same time contribute to the Greenhouse Effect.

Fuel cells are basically a type of battery containing an oxidant and a reducing agent that converts chemical energy into electrical energy. Theoretically, they are capable of producing energy as long as the reactants are fed into the device, which means that ideally, they can operate indefinitely. However, in reality, degradation or malfunctioning of the components may limit the working life of these batteries. ⁽¹⁾

Historically, Sir William Grove is credited as the creator of the first fuel cell in 1839. Grove conducted a series of experiments with what he termed a gas voltaic battery, which ultimately proved that electric current could be produced from an electrochemical reaction between hydrogen and oxygen over a platinum catalyst.

However, the concept of a fuel cell had effectively been demonstrated in the early nineteenth century by Humphry Davy and its concept was subsequently developed by the scientist Christian Friedrich Schönbein in 1838. Yet, the term fuel cell was not used until 1889 when Charles Langer and Ludwig Mond, who researched fuel cells using coal gas as a fuel, coined the term.

In 1932, Cambridge engineering professor Francis Bacon modified Mond and Langer's equipment to develop the first AFC but it was not until 1959 that Bacon demonstrated a practical 5 kW fuel cell system.

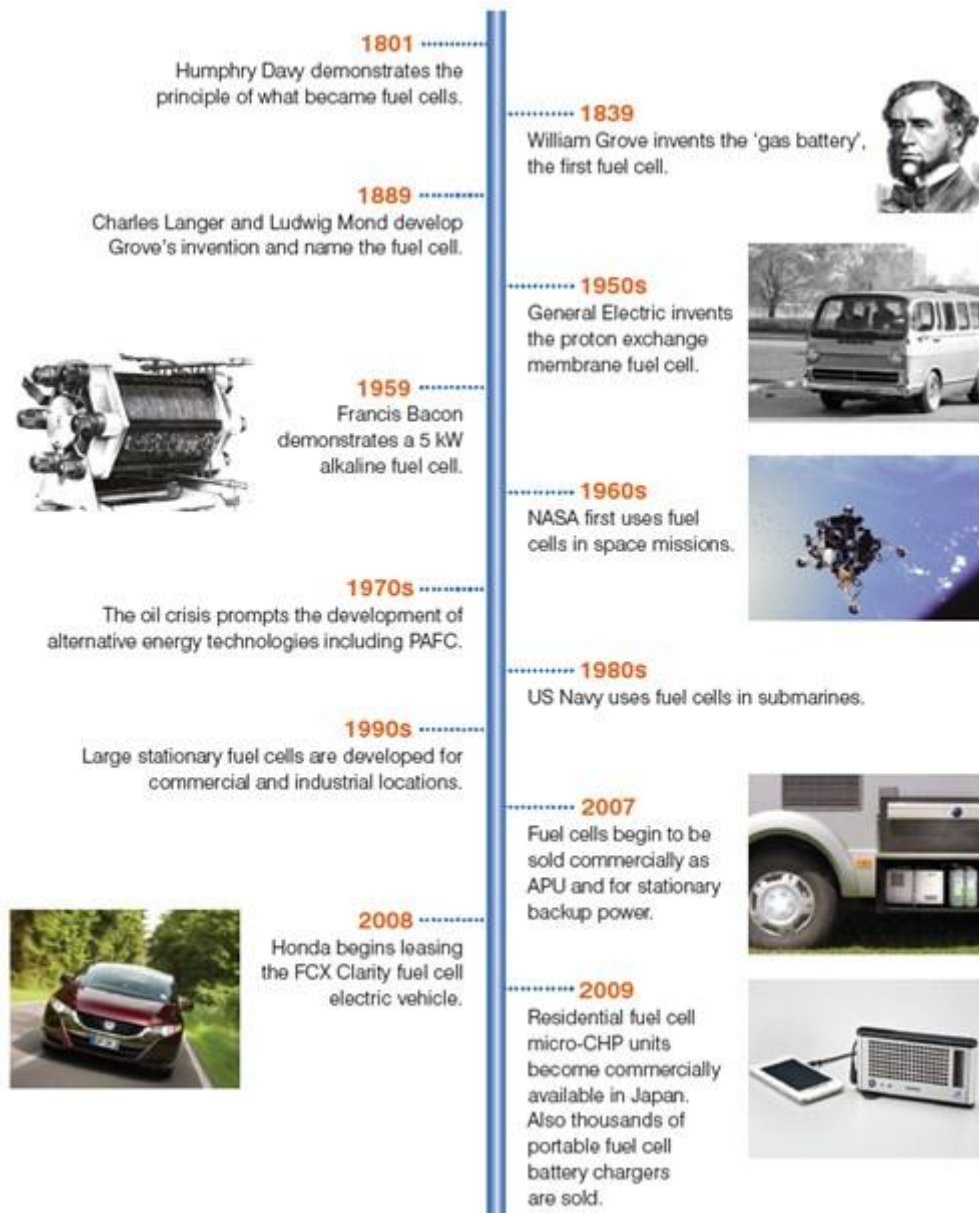


Figure 1.1 Brief History of Fuel Cells (2)

Nowadays there are several types of fuel cell in commerce and each one has its own operational characteristics. Yet, in the most general way, a fuel cell can be described as follows: hydrogen molecules enter at the anode where an electrochemical reaction strips them of their electrons, producing protons that dissolve in an electrolyte. The negative electrons provide the current through wires in order to do work.

Oxygen enters at the cathode and there it combines with the electrons returning from the electrical circuit and the hydrogen that has traveled through the electrolyte from the anode.

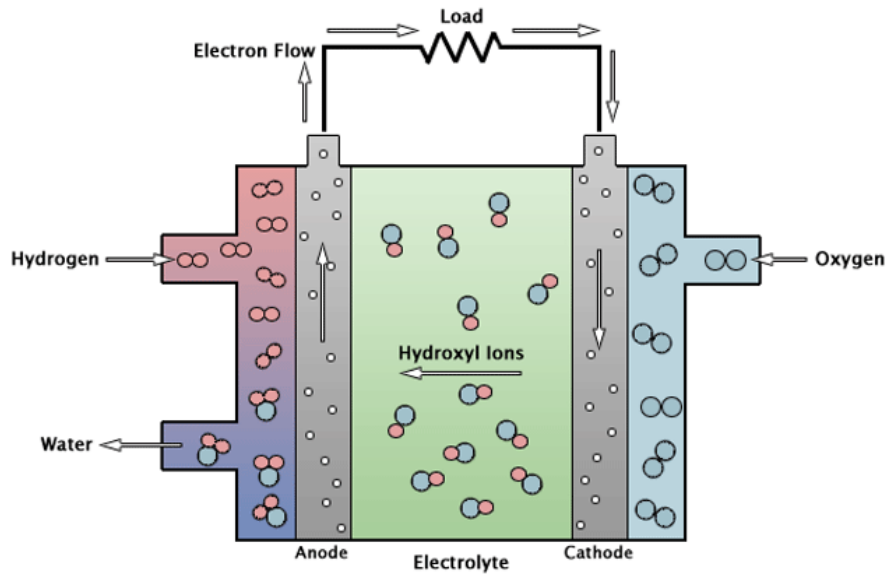


Figure 1. 2 Structure of a FC ⁽³⁾

The electrolyte plays a key role within a fuel cell. It must permit only the appropriate ions to pass between the anode and the cathode or vice versa. If free electrons or other substances travel through the electrolyte, there would be a disruption of the electrochemical reaction. ⁽⁴⁾

The following figure summarizes the different types of FC available and their main characteristics ⁽⁵⁾:

Fuel Cell Type	Common Electrolyte	Operating Temperature	Typical Stack Size	Efficiency	Applications	Advantages	Challenges
Polymer Electrolyte Membrane (PEM)*	Perfluoro sulfonic acid	50-100°C 122-212°F	1 kW-250 kW	60% transportation 35% stationary	<ul style="list-style-type: none"> Backup power Portable power Distributed generation Transportation Specialty vehicles 	<ul style="list-style-type: none"> Solid electrolyte reduces corrosion & electrolyte management problems Low temperature Quick start-up 	<ul style="list-style-type: none"> Expensive catalysts Sensitive to fuel impurities
Alkaline (AFC)	Aqueous solution of potassium hydroxide soaked in a matrix	90-100°C 19-212°F	10-100 kW	60%	<ul style="list-style-type: none"> Military Space 	<ul style="list-style-type: none"> Cathode reaction faster in alkaline electrolyte, leads to high performance Low cost components 	<ul style="list-style-type: none"> Sensitive to CO₂ in fuel and air Electrolyte management
Phosphoric Acid (PAFC)	Phosphoric acid soaked in a matrix	150-200°C 302-392°F	400 kW 100 kW module	40%	<ul style="list-style-type: none"> Distributed generation 	<ul style="list-style-type: none"> Higher temperature enables CHP Increased tolerance to fuel impurities 	<ul style="list-style-type: none"> Pt catalyst Long start up time S sensitivity
Molten Carbonate (MCFC)	Solution of lithium, sodium, and/or potassium carbonates, soaked in a matrix	600-700°C 1112-1292°F	300 kW-3 MW 300 kW module	50-60%	<ul style="list-style-type: none"> Electric utility Distributed generation 	<ul style="list-style-type: none"> High efficiency Fuel flexibility Can use a variety of catalysts Suitable for CHP 	<ul style="list-style-type: none"> High temperature corrosion and breakdown of cell components Long start up time Low power density
Solid Oxide (SOFC)	Yttria stabilized zirconia	600-1000°C 1112-1832°F	1 kW-2 MW	50-60%	<ul style="list-style-type: none"> Auxiliary power Electric utility Distributed generation 	<ul style="list-style-type: none"> High efficiency Fuel flexibility Can use a variety of catalysts Solid electrolyte Suitable for CHP & CHHP Hybrid/GT cycle 	<ul style="list-style-type: none"> High temperature corrosion and breakdown of cell components HT operation requires long start up time and limits shutdowns

*Direct Methanol Fuel Cells (DMFC) are a subset of PEM typically used for small portable power applications with a size range of about a subwatt to 250 W and operating at 60-90°C.

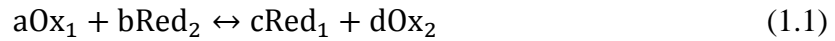
Figure 1. 3 Classification of Fuel Cells

Electrolytic cells, on the other hand, perform the opposite action of FC. It is an electrochemical cell that undergoes a redox reaction when electrical energy is applied to it in order to decompose the chemical compounds fed to the system.

All considerations that will be furtherly done on fuel cells can also be applied to electrolytic cells by bearing in mind the conceptual different these two dispositive present.

1.1.2 Thermodynamic considerations in a Fuel Cell:

The overall reaction that takes place is:



The total voltage of the cell, ΔE , is given by the difference of two semi-reactions while the equilibrium potential of each semi-reaction is given by the Nernst equation.

$$E = E^\circ + \frac{RT}{nF} \ln \frac{[Ox]}{[Red]} \quad (1.2)$$

The term E° is the standard electrode potential and $[red]$ ($[ox]$) is the activity of reducing (oxidizing) species. Consequently, the voltage of the cell in absence of current is given by equation 1.3:

$$E = E_1 - E_2 = E_1^\circ - E_2^\circ + \frac{RT}{nF} \ln \frac{[Ox_1]^a [Red_2]^b}{[Red_1]^c [Ox_2]^d} \quad (1.3)$$

Variation of Gibbs free energy for the same reaction can be defined as:

$$\Delta G = \Delta G^\circ + RT \ln \frac{[Ox_1]^a [Red_2]^b}{[Red_1]^c [Ox_2]^d} \quad (1.4)$$

The cell voltage and the Gibbs free energy can be related by means of the equation:

$$\Delta G = -nFE \quad (1.5)$$

As said before, each electrochemical reaction is characterized by the Nernst equation. Nevertheless, all the previous thermodynamics were under the hypothesis of no current flow. When current flows electrical work is performed, which leads to a deviation of the potential from equilibrium occurs. The deviation from the equilibrium values is called the over potential η .

For a redox reaction at one electrode the current j is given -in the simplest case- by the Butler-Vollmer equation:

$$j = j_0 \left[\exp \left(\frac{(1-\alpha)nF\eta}{RT} \right) - \exp \left(\frac{-\alpha nF\eta}{RT} \right) \right] \quad (1.6)$$

J_0 is the exchange current density and α is the electron transfer coefficient. The equation holds when the charge transfer dominates the reaction at small values of j and η .

Other limiting factors, like mass transport hindrance of temperature effects, are present on real systems and are described in terms of potential losses. ⁽⁶⁾

1.2 Solid Oxide Fuel Cells (SOFC)

The technology of ceramic membranes offers remarkable economic advantages due to their structural, conductive, electrical and electrolytic properties. Furthermore, they also give way to more secure and environmental friendly processes. ⁽⁷⁾

Solid Oxide Fuel Cells come in different formats, yet they can be divided into two main categories: supported and self-supporting structures. For the supported design a substrate is used to provide the cell with the necessary mechanical stability while the self-supported concept is based on the possibility of using either the anode or the cathode as the support.

Among the most popular designs the following can be found:

- Siemens-Westing tubular
- Sulzer-Hexis tubular
- Monolithic
- Planar

Tubular designs have a self-sealing structure which improves thermal stability. However, the planar configuration is more efficient and cheaper than the tubular one. The best of all is the monolithic planar cell because it combines both the tubular and the planar characteristics. Figure 1.4 shows the different aforementioned designs. ⁽⁶⁾

Up until about six years ago, SOFCs were being developed for operation primarily in the temperature range of 900 to 1000°C. In addition to the capability of internally reforming hydrocarbon fuels (e.g., natural gas), such high temperature provide high quality exhaust heat for cogeneration, and when pressurized, can be integrated with a gas turbine to further increase the overall efficiency of the power system.

However, reduction of the SOFC operating temperature by 200 °C or more allows using a broader set of materials, is less-demanding on the seals and the balance-of-plant components, simplifies thermal management, aids in faster start up and cool down, and results in less degradation of cell and stack components.

Because of these advantages, activity in the development of SOFCs capable of operating in the temperature range of 650°C to 800 °C has increased dramatically in the last few years. However, at lower temperatures, electrolyte conductivity and electrode kinetics decrease significantly. In order to overcome these drawbacks, alternative cell materials and designs are being extensively investigated.

A SOFC essentially consists of two porous electrodes separated by a dense, oxide ion conducting electrolyte. The operating principle of such a cell is illustrated in Figure 1.5. Oxygen supplied at the cathode (air electrode) reacts with incoming electrons from the external circuit to form oxide ions, which migrate to the anode (fuel electrode) through the oxide ion conducting electrolyte.

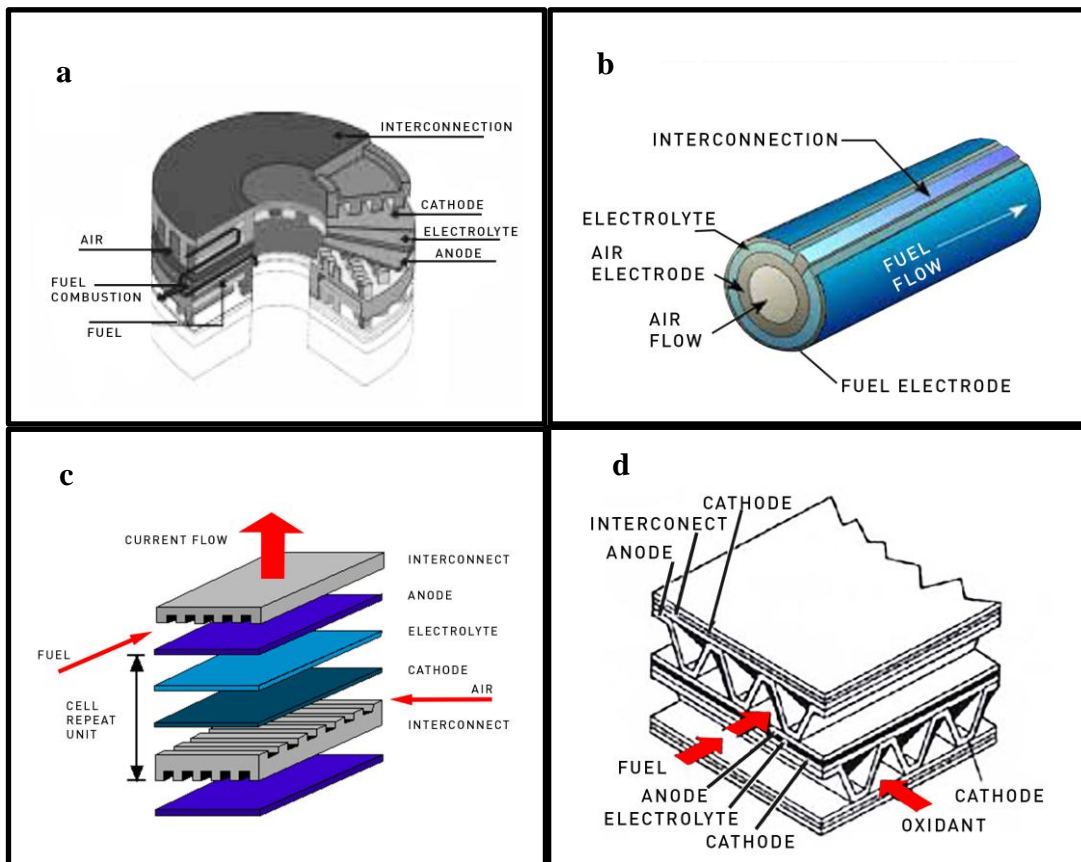


Figure 1.4 SOFC configuration: a) Sulzer-Hexis tubular, b) Siemens-Westing tubular, c) Planar, d) Monolithic

At the anode, oxide ions combine with H₂ (and/or CO) in the fuel to form H₂O (and/or CO₂), liberating electrons. Electrons flow from the anode through the external circuit to the cathode. ⁽⁸⁾

The main function of the electrode is to support the reaction between the reactant (fuel or oxygen) and the electrolyte, without itself being consumed or corroded. It must also bring into contact the three phases, i.e., the gaseous fuel, the solid electrolyte and the electrode itself.

The anode, used as the negative post of the fuel cell, disperses the hydrogen gas equally over its whole surface and conducts the electrons, that are freed from hydrogen molecule, to be used as a useful power in the external circuit.

The cathode, the positive post of the fuel cell, distributes the oxygen fed onto its surface and conducts the electrons back from the external circuit where they can recombine with oxygen ions, passed across the electrolyte, and hydrogen to form water.

The electrolyte determines the operating temperature of the fuel cell and is used to prevent the two electrodes to come into electronic contact by blocking the electrons. It also allows the flow of charged ions from one electrode to the other to maintain the overall electrical charge balance. ⁽⁹⁾

The materials for the cell components are selected based on suitable electrical conducting properties required of these components to perform their intended cell functions; adequate chemical and structural stability at high temperatures encountered during cell operation as well as during cell fabrication; minimal reactivity and inter diffusion among different components; and matching thermal expansion among different components. ⁽⁸⁾

SOFC display several technical advantages with respect to other typologies of fuel cells such as the absence of catalysts due to the high temperatures and the use of a stable electrolytic solid, which eliminates corrosion and evaporation problems. Components, being all solid, allow for a very compact assemblage that cannot be achieved with the use of liquid electrolyte.

Theoretically, any gas that shows oxidant or reductive can be used as fuel or oxidant. Oxygen is the most common oxidant since it can be found in air, while hydrogen is the most utilized fuel due to its reactivity and high calorific value.

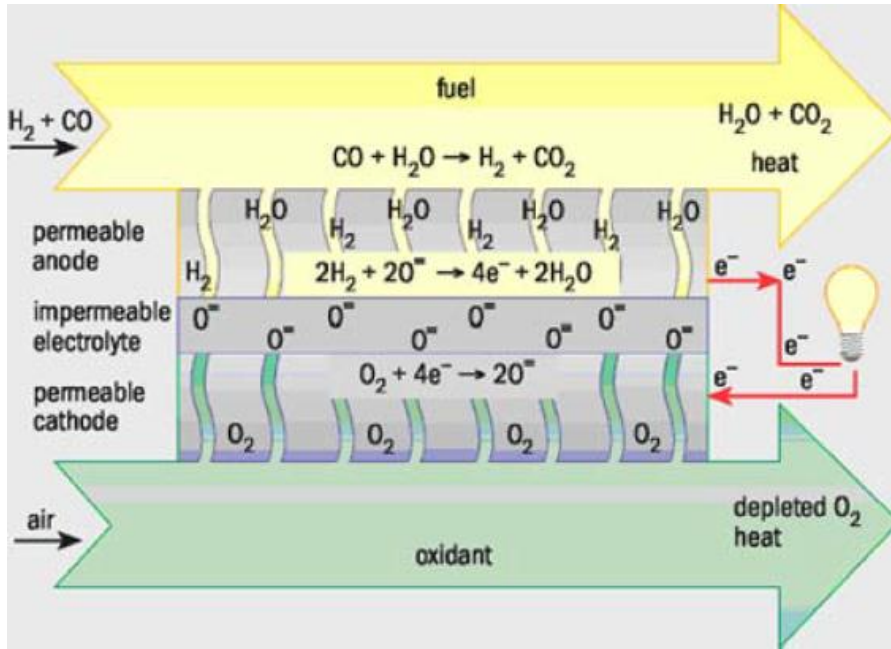


Figure 1.5 Reactions inside a FC

The use of ceramic materials and the high temperatures allows for a feed of hydrocarbons. The production of H₂ takes place inside through a fuel reforming reaction while the oxidation of CO to CO₂ occurs with a water-gas shift reaction. ⁽¹⁰⁾



1.3 Materials for Cell Components

1.3.1 Electrolytes

The key requirement for the solid electrolyte is that it has to have a good ionic conduction to minimize cell impedance, but also little or no electronic conduction in order to minimize leakage currents. Consequently, control of the concentration and mobility of ionic and electronic charge carriers is critical. The electrolyte material must also be chemically and mechanically (e.g. thermal expansion) compatible with other fuel cell components.

A major impetus for the development of new electrolyte materials is in reducing the operating temperature to 500°C–800 °C for intermediate temperature Solid Oxide Fuel

Cells. Such an intermediate operating temperature will relax some of the requirements related to high-temperatures operation, while maintaining a sufficiently high temperature to retain good fuel flexibility. ⁽¹¹⁾

As the SOFC performance is dominated mainly by the ohmic loss of the electrolyte, optimizing the electrical properties of the sintered electrolytes is of significant importance.

Y₂O₃-stabilized-ZrO₂ (YSZ) is one of the most popular materials employed as electrolyte in SOFC because of its attractive ionic conductivity, stability in dual environment (oxidizing and reducing) and stability against the electrode materials. ⁽¹²⁾

YSZ is manufactured by doping ZrO₂ with the acceptor Y₂O₃. Zirconia exists in three phases, monoclinic up to 1100°C, tetragonal with distorted fluorite structure up to 2400°C and a cubic fluorite structure above 2400°C.

The cubic fluorite structure has a face-centered cubic (FCC) zirconia lattice and a cubic oxygen lattice placed in the FCC lattice. The Zr⁴⁺ cations occupy the tetrahedral sites and the O²⁻ anions the octahedral sites. The remaining octahedral sites are occupied by the Zr⁴⁺ cations, see Figure 1.6.

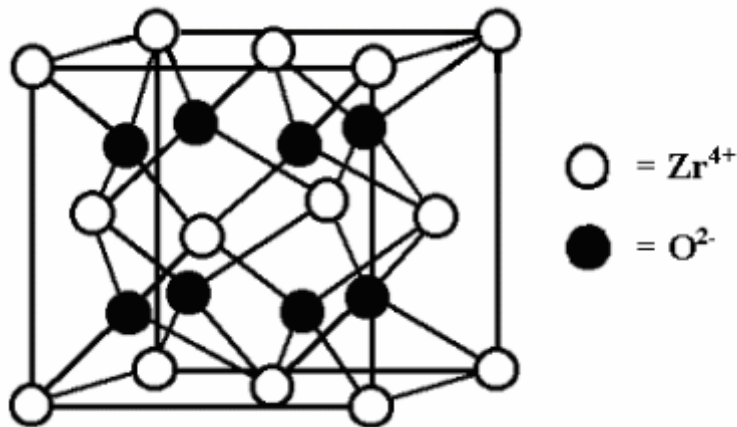


Figure 1.6 Structure YSZ

The ionic conductivity of stabilized zirconia depends on the dopant concentration and the size of the acceptors. A minimum activation energy is found for acceptors with an ionic radius that closely matches that of the Zr⁴⁺ ion, of which Y³⁺ is one. The addition of Y₂O₃ stabilizes the zirconia cubic fluorite structure to room temperature and changes the non-conducting zirconia into an ion conducting material.

When doping ZrO_2 with Y_2O_3 , the Zr^{4+} cations in the ZrO_2 lattice are substituted by the Y^{3+} cations thereby forming oxygen vacancies to maintain charge neutrality in the lattice. The oxygen vacancies make it possible for oxygen ions to move through the electrolyte by hopping from vacancy to vacancy in the lattice.

The oxygen vacancies are mobile at high temperatures and give rise to high oxygen ionic conductivity. More than 99% of the current through YSZ is carried by oxide ions. The oxygen vacancies experience two types of interactions in the lattice, the repulsion between the oxygen vacancies themselves and other positively charged carriers, and the attraction between oxygen vacancies and the acceptor Y.

The maximum ionic conductivity lies around 8%-9% mol Y_2O doping. At higher doping the attraction between the oxygen vacancies and the yttria will result in the formation of complexes and decreases the mobility of the oxygen vacancies. The complex has a positive effective charge when an oxygen vacancy is bonded to only one cation.

A further increase of the yttria concentration, and thereby the vacancy concentration, gives more complex associations, which can form clusters. In these clusters the oxygen vacancy is bonded to two cations, decreasing the oxygen vacancies' mobility further. This complex is electrostatically neutral.

Besides a good ionic conductivity, YSZ exhibits a high micro hardness, is corrosion resistant, has a low thermal conductivity and is chemically stable at high temperatures. (13)

YSZ, however, is not the only material that can be used as electrolyte for SOFCs. Recently, ceria-based solid oxides have received increasing attention as electrolyte material for low-temperature solid oxide fuel cells. The low-temperature operation provides an economic benefit through possible replacement of some of the expensive ceramic components of the cell by relatively cheaper metallic alternatives. It can also eliminate problems caused by the reaction of the electrolyte with other cell components.

On the other hand, ceria-based electrolytes easily develop n-type electronic conduction at high temperatures and low oxygen partial pressures. This is one of the constraints for them to be used as the electrolyte material for SOFCs. Some efforts have been made to suppress the electronic conductivity and to extend the electrolyte domain of the ceria-based electrolytes. (14)

Depending upon the dopants, ceria acts as either oxygen ionic-conductor or ionic-electronic mixed conductor. For the enhancement of ionic conductivity, dopants which have ionic radii very close to ceria are normally selected. Doping with R^{3+} ions ($R=\text{Gd}, \text{Sm}, \text{Nd}, \text{Y}, \text{Pr}, \text{etc.}$) in the crystal structure of ceria was found to increase the number of extrinsic oxygen vacancies due to the reduction of Ce^{4+} to Ce^{3+} that ultimately enhance the bulk ionic conductivity of ceria at the end.

Gd^{3+} ion doped ceria, particularly 10% mol Gd^{3+} ion ($\text{Ce}_{0.9}\text{Gd}_{0.1}\text{O}_{1.95}$) is paid more attention because it has been already approved as a potential electrolyte for fuel cells with low operating temperatures. Since a high dense membrane electrolyte is needed, nanocrystalline Gd^{3+} ion doped ceria powders are being processed. ⁽¹⁵⁾

Another material which is currently under investigation is lanthanum gallate. LaGaO_3 ceramics that have been doped with strontium and/or magnesium are known to have superior oxygen-ion-conducting properties, in comparison, for instance, to yttria-stabilized zirconia electrolytes. ⁽¹⁶⁾

But the poor chemical compatibility of the LSGM with the anode materials makes fabrication of the anode-supported cells very difficult. ⁽¹⁷⁾

1.3.2 Cathodes

Cathode materials should possess high electrical conductivity and high electro catalytic activity for the oxygen reduction reaction. Furthermore, the compatibility with adjacent cell components and the chemical and dimensional stability during cell operation are very important factors.

Moreover, the cathode material should also be sufficiently porous to facilitate transport of the oxidant to the cathode/electrolyte interface. In addition, the perovskites should be stable at the intermediate and lower temperatures used for operation of fuel cells and in CO_2 containing atmospheres. ⁽¹⁸⁾

The majority of perovskite-type oxides currently considered as cathodes are based on either the $\text{La}_{1-x}\text{Sr}_x\text{CoO}_3$ or $\text{La}_{1-x}\text{Sr}_x\text{MnO}_3$ materials. Therefore, it is sensible to deal with these two classes of materials individually, and examine the performance of the related materials.

The use of lanthanum cobaltate materials as possible cathodes has been widely investigated in recent years. Initially, of most interest were $\text{La}_{1-x}\text{Sr}_x\text{Co}_{3-\delta}$ (LSC) perovskites, which it was found possessed considerable oxide ion conductivity and sufficient electronic conductivity to make them of interest as mixed ionic- electronic conductors.

It has been noted that the use of LSC as a cathode material, although attractive when the conductivity is considered, becomes less so when the performance of the oxide under operating conditions is evaluated. ⁽¹⁹⁾

Doped lanthanum manganese (LaMnO_3) is the most commonly used. It is a p-type perovskite oxide, which can have a range of oxygen stoichiometries depending on processing history, temperature, and the ambient oxygen partial pressure. Although LaMnO_3 is stable under oxidizing conditions, it dissociates under highly reducing conditions ($P_{\text{O}_2} \leq 10^{-14}$ bar at 1000°C).

It has intrinsic p-type conductivity due to the formation of cation vacancies, and electronic conduction arises from a mechanism called small polaron hopping. Essentially, this is due to the hopping of an electron hole between the Mn^{3+} and Mn^{4+} valence states. Doping with a lower valence (divalent) ion such as calcium, strontium, barium, or magnesium enhances this effect and is commonly used to obtain higher conductivity in LaMnO_3

The electrical behavior of doped LaMnO_3 is significantly affected by oxygen partial pressure. At about 1000°C the conductivity shows little dependence on oxygen partial pressure. However, the range of oxygen partial pressures over which the conductivity remains constant becomes smaller as temperature increases.

At lower oxygen partial pressures, the conductivity decreases. An abrupt decrease is observed at a critical oxygen partial pressure corresponding to the decomposition of the LaMnO_3 phase. At elevated temperatures, the manganese in LaMnO_3 is known to be mobile species and can, when diffused in the electrolyte, change its electrical properties. ⁽²⁰⁾

1.3.3 Anodes

In order for an anode material to achieve the best performance for being applied to an SOFC, it should satisfy the following criteria: (a) high electrical conductivity; (b) stability under reducing environment; (c) thermal expansion and chemical compatibility with electrolyte and other components; (d) sufficient porosity to maintain the three-phase boundary (TPB) among electrolyte, electrode, and gas phase, which can act as an electrochemically active site for the electrode reaction.

Porous Ni/YSZ cermets have been extensively studied as anodes for SOFCs, as they not only meet the above-mentioned requirements but also have low cost. While Ni serves as an excellent reforming catalyst and electro catalyst for oxidation of hydrogen as well as the electronically conducting phase, YSZ is added in order to support Ni particles, inhibit coarsening of the Ni, and provide a thermal expansion coefficient similar to that of zirconia-based electrolytes. Additionally, YSZ also offers a significant ionic contribution to the overall conductivity, effectively broadening the TPB.

The properties of Ni/YSZ anodes are highly dependent on the particle size and the microstructure of the cermet. Microstructural modifications during operation, like agglomeration and sintering of Ni particles, and carbon deposition, due to the internal reforming of hydrocarbons, are the main causes of anode performance degradation.

The agglomeration of nickel particles leads to a significant reduction in TPB and an increase in the electrode polarization resistance. The carbon formation could obstruct gas access and degrade anode performance by blocking the catalyst active sites. Usually, large quantities of steam are added to hydrocarbon fuels to avoid carbon deposition. However, the addition of excess steam leads to accelerated coarsening of Ni particles and reduction of the electrochemical potential according to the Nernst equation. Thus, it is essential to optimize the morphological and structural properties of the cermets in order to improve the activity and operational stability of Ni/YSZ anodes. ⁽²¹⁾

Carbon formation is usually thermodynamically favored with hydrocarbon fuels at the low O₂ fugacities that exist in the anode compartment, unless there is also a large quantity of steam. Therefore, the conventional approach to avoid carbon formation is to simply add steam or oxygen with the fuel. In addition to the added complexity of a system in

which steam is added with the hydrocarbon, the added steam is effectively a diluent that reduces the anode fuel concentration.

Unfortunately, there is no thermodynamic window of stability at practical temperatures for hydrocarbons other than methane. Therefore, direct oxidation is not in general possible for anodes which contain Ni or other materials that catalyze the approach to equilibrium. ⁽²²⁾

While some progress has been made in improving the hydrocarbon and sulfur tolerance and the redox stability of Ni/YSZ anodes by altering their composition and microstructure, the inherent properties of Ni make these difficult problems to overcome.

One approach to solving these problems that has received much attention in recent years is to replace the Ni in the anode with a much less catalytically active metal, such as Cu, or metal alloys that do not catalyze the formation of carbon from dry hydrocarbons.

For Cu this requires the use of different synthesis techniques, however, since the low melting temperatures of Cu and copper oxides (both melt below 1150 °C) do not allow Cu to be incorporated into the anode using approaches similar to that used for Ni/YSZ anodes which require sintering temperatures in excess of 1200 °C.

YSZ composite anodes containing Cu and CeO₂ have been shown to be active for the direct electrochemical oxidation of hydrocarbons without promoting coke or carbon fiber formation. Anodes of this design exhibit relatively stable performance when operating on hydrocarbon fuels ranging from methane to toluene.

In the anode design Cu is used primarily as the current collector and CeO₂ imparts catalytic activity for the oxidation reactions. An added advantage of Cu/CeO₂/YSZ anodes is that they exhibit very high sulfur tolerance and can operate on fuels with sulfur contents up to ~ 400 ppm without significant loss in performance. These anodes also have inherently high redox stability.

While Cu/CeO₂/YSZ anodes have interesting properties, especially their ability to operate directly with dry hydrocarbon fuels, they undergo slow deactivation at temperatures above 700 °C. This decreases the available three-phase boundary where the electrochemical reactions take place.

Studies of anodes in which electron transport is provided by ceramic components rather than metals are perhaps the most exciting area of SOFC anode research in the last several years. The general idea is that since the metal components of the anode are the ones that exhibit very low tolerance to hydrocarbons and impurities such as sulfur, these problems can be eliminated by removing the metals altogether and using only ceramic components for electron transport and oxidation catalytic activity.

Ideally a mixed, oxide ion and electronic conducting ceramic should be used since the ionic conductivity would serve to increase the effective size of the TPB. The electronic conductivity of the ceramic also needs to be maintained over both reducing and oxidizing conditions in order to allow for operation at both low and high fuel utilizations.

The primary challenge in designing ceramic anodes is that while some materials have a few of the desired materials properties mentioned above, it is hard to identify a single material that has all of the desired properties, particularly redox stability and high electronic conductivity. Materials that have the best compromise of the desired properties, however, tend to be perovskite type ABO_3 oxides in which more than one cation is used on the A and B sites.

A common problem, however, with ceramic anodes which is that while they are stable when operating on hydrocarbons and do not promote carbon deposition, they have very low catalytic activity for hydrocarbon oxidation and thus exhibit poor performance on hydrocarbon fuels. ⁽²³⁾

1.4 Mixed Ionic and Electronic Conductivity (MIEC)

1.4.1 MIEC Principles

For maximization of the active reaction area and hence a lowering of the polarization resistance, SOFC electrodes consists today of interpenetrating ionically and electronically conducting networks. This can be achieved by the use of mixed ionic electronic conductor (MIEC) materials or composite electrodes where one material is a good electronic conductor and the other material a good oxide ion conductor. ⁽²⁴⁾

MIECs are materials that conduct both ions and electronic charge carriers (electrons and/or holes). This definition can be extended to say that a MIEC is a material that conducts matter (ions and/or atoms) and electronic charge carriers.

Normally, MIECs are ionic semiconductors but the definition is not limited to ionically bonded solids and holds also for metallic bonding, nor to crystalline solids and it holds as well for glasses and polymers. In addition to true MIECs, there are also heterogeneous MIECs (H-MIECs) which are mixtures of two phases, one conducting ions the other conducting electrons/holes. An example is Ni-YSZ cermets, which are the common anode in solid oxide fuel cells (which are based on the oxygen ion conductor YSZ).⁽²⁵⁾

While past research concentrated on improvements of oxygen ionic conductor for use in fuel cells, recent efforts are motivated to introduce the electronic conductivity into materials that predominantly are ionic conductors.

A driving force has to be provided for oxygen to permeate through the membrane. This driving force can be either an electrical potential gradient or a chemical potential gradient (i.e. gas component partial pressure). As oxygen is transported in the ionic form, and to fulfill the electric neutrality criteria, there must be a simultaneous flux of electrons in the opposite direction to charge compensate the oxygen flux.

In certain materials that provide only ionic conductivity, electrodes are provided for the electron pathway as depicted in Figure 1.7. A benefit inherent in such a system is the control over the amount of oxygen generated via the application of an electric current.

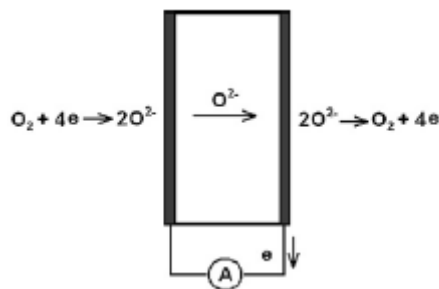


Figure 1.7 Electrode electron pathway

A mixed ionic–electronic membrane, in contrast, requires no electrodes to operate, although it needs the oxygen pressure difference on both sides of the membrane. These membranes do not have to be consisted of one phase only capable for both ionic and electronic conduction.⁽²⁶⁾

MIEC seem to be the best type of electrode materials for electrochemical devices such as SOFC and electrolyzers. However, until now most developers of SOFC do not use effective MIEC electrodes.

For a MIEC to act as both an efficient electrode and current collector several requirements must be fulfilled:

- Ionic conductivity, $\sigma_i \geq 0.1$ S/cm and electronic conductivity, $\sigma_e \geq 100$ S/cm at operating conditions.
- Dimensional and thermodynamic stability over wide ranges of oxygen partial pressure and temperature.
- Good thermal expansion coefficient match with the electrolyte.
- Chemical compatibility with the electrolyte during operation and fabrication
- High electrocatalytic activity for oxygen reduction and fuel oxidation for cathode and anode, respectively. ⁽²⁷⁾

1.4.2 Ionic Conductivity from Literature

In the last couple of decades, research has tried to provide new materials for the use of SOFC. The aim of conductivity measurements is to characterize the properties of the materials to be used in the fuel cells. These new materials have to have comparable features at lower temperatures (500°C-600°C) to those used at higher temperatures (800°C-900°C).

Even though MIEC materials show both electronic and ionic conductivity, it has been proven that only ionic conductivity changes drastically as a function of temperature. For this motive, ionic conductivity is highly evaluated while characterizing SOFC ceramic materials.

The easiest way to analyze this type of conduction is through oxygen permeation. Many techniques on how to measure oxygen permeation can be found in literature, yet most configuration are similar to that depicted in figure 1.8.

In a general way, conductivity can be quantified as follows: air is sent from below the ceramic material while a sweep gas is sent from above. The sweep gas catches the oxygen

that passes through the material and the mixed flow is then analyzed one way or another to determine the concentration of oxygen in the sweep gas.

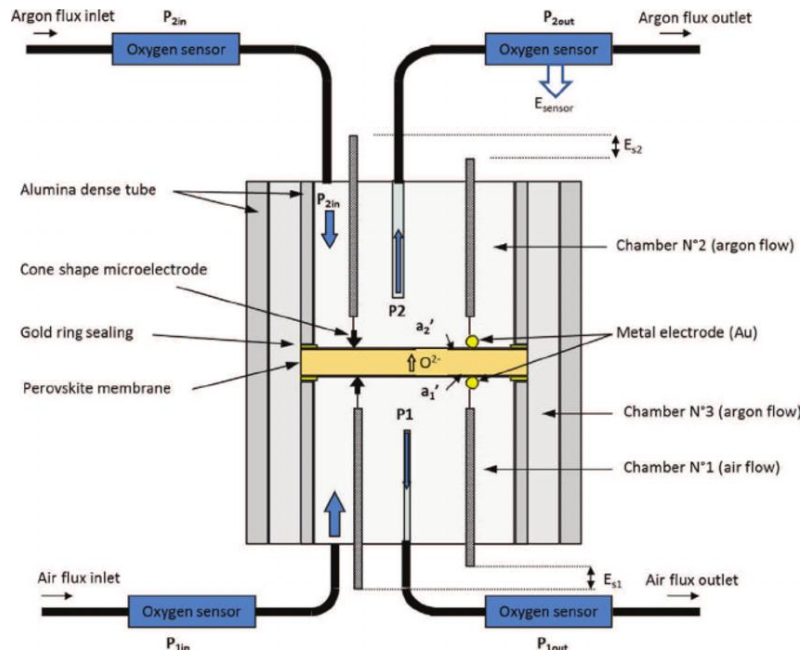


Figure 1.8 Schematic of an oxygen permeation setup

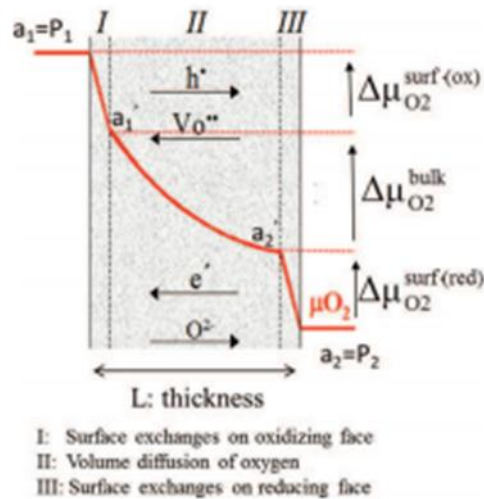


Figure 1.9 Steps of oxygen transport

The oxygen transport can be described in three main steps, as shown on fig. 1.9: (1) surface exchanges on the oxidizing face, (2) oxygen diffusion through the membrane bulk

and, (3) surface exchanges on the reducing face. The knowledge of the oxygen activity profile allows the identification of the rate determining step of the oxygen flux through the membrane. For instance, a large drop of oxygen chemical potential through the membrane volume, $\Delta\mu^{\text{bulk}}_{\text{O}_2}$, corresponds to an oxygen flux governed by oxygen diffusion through the membrane, while a large drop of oxygen chemical potential on the membrane surfaces corresponds to an oxygen flux governed by oxygen surface exchanges. ⁽²⁸⁾

Equations defining O_2 flux through the membrane vary from author to author, consequently such equations must be explicitly defined every time in order to allow the reader to fully understand how calculations were carried.

Yet, it is always expected to obtain a curve that is proportional to the reciprocal of the temperature as shown in figure 1.10. In other words, as temperature is raised conductivity improves. For this reason, it is of consequence to obtain a good trade-off between conductivity and temperature. ⁽²⁹⁾

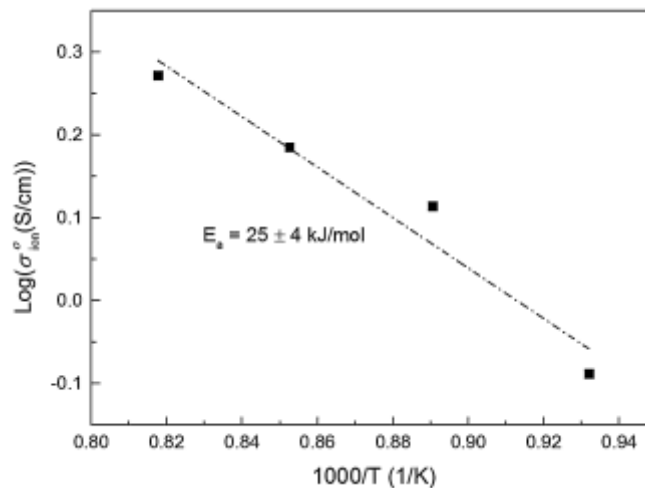


Figure 1.10 Dependence of conductivity on temperature

CHAPTER 2

TECHNIQUES AND INSTRUMENTATION

2.1 Electrochemical Impedance Spectroscopy - EIS

2.1.1 Introduction to EIS

Electrochemical Impedance Spectroscopy (EIS) involves the study of the variation of the impedance of an electrochemical system with the frequency of a small-amplitude AC perturbation. ⁽³⁰⁾

Impedance spectroscopy is a non-destructive technique and so can provide time dependent information about the properties but also about ongoing processes such as corrosion or the discharge of batteries and e.g. the electrochemical reactions in fuel cells, batteries or any other electrochemical process.

Commonly, impedance is known as the ability to resist the flow of an electrical current without limitation of Ohm's law. In a more specific way, impedance can be defined as a complex resistance realized when current flows through a circuit composed of various resistors, capacitors or inductors.

Even though the concept of impedance can be used for systems working both in direct and alternate current, the EIS technique focuses only on systems through which an alternate current pass. Also, as mentioned above, the amplitude of the perturbation that goes through the system has to be small enough in order to maintain linearity.

A linear system is one that possesses the important property of superposition: if the input consists of the weighted sum of several signals, then the output is simply the superposition (weighted sum) of the responses of the system to each of the signals

Most elements that are analyzed using this technique do not show a linear behavior for a wide range of operating conditions. However, for a very small-defined range this property can be used to advantage of the analysis. ⁽³¹⁾

In order to explain the importance of linearity, first the concept of resistance must be defined. Ohm's law defines resistance in terms of the ratio between voltage E and current I.

$$R(t) = \frac{E(t)}{I(t)} \quad (2.1)$$

The relationship is limited to only one circuit element (the ideal resistor). An ideal resistor has several simplifying properties:

- It follows Ohm's Law at all current and voltage levels.
- It's resistance value is independent of frequency.
- AC current and voltage signals through a resistor are in phase with each other.

Circuit elements exhibit much more complex behavior and consequently the simple concept of resistance must be abandoned. In its place impedance is used, which is a more general circuit parameter. Unlike resistance, impedance is not limited by the simplifying properties listed above.

Electrochemical impedance is usually measured by applying an AC potential to an electrochemical cell and measuring the current through the cell.

By applying a sinusoidal potential excitation, an AC current signal response is obtained, containing the excitation frequency and its harmonics. This current signal can be analyzed as a sum of sinusoidal functions (a Fourier series).

In a linear (or pseudo-linear) system, the current response to a sinusoidal potential will be a sinusoid at the same frequency but shifted in phase as shown in figure 2.1.

The excitation signal, expressed as a function of time, has the form of:

$$E(t) = E_0 \cos(\omega t) \quad (2.2)$$

$E(t)$ is the potential at time t , E_0 is the amplitude of the signal, and ω is the radial frequency.

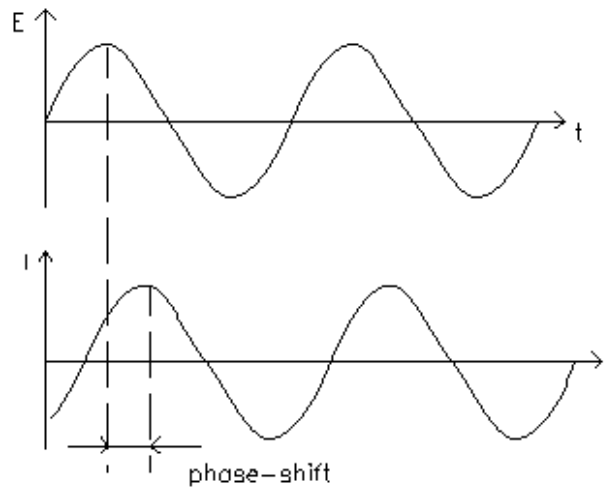


Figure 2.1 Relation between potential input and current output.

In a similar way, the output current I_0 can be expressed in terms of the radial frequency and the phase shift:

$$I(t) = I_0 \cos(\omega t - \phi) \quad (2.3)$$

By using these new definitions of potential and current, an analogous expression to Ohm's law can be written as following: ⁽³²⁾

$$Z(t) = \frac{E(t)}{I(t)} = \frac{E_0 \cos(\omega t)}{I_0 \cos(\omega t - \phi)} = Z_0 \frac{\cos(\omega t)}{\cos(\omega t - \phi)} \quad (2.4)$$

2.1.2 Data Presentation

The data obtained from an EIS analysis can provide 3 main figures that represent the overall behavior of system in question.

The Lissajous curve is the least important between the figures, yet it allows to precisely measure the phase difference between two waves of the same frequency. Lissajous figures are formed when two simple harmonic vibrations are coupled at right angle to each other.

For true Lissajous figures the ratio between the two frequencies is equal to the ratio of maximum intersections of a vertical line and a horizontal one with the figure. ⁽³³⁾ Such a figure is shown in figure 2.2.

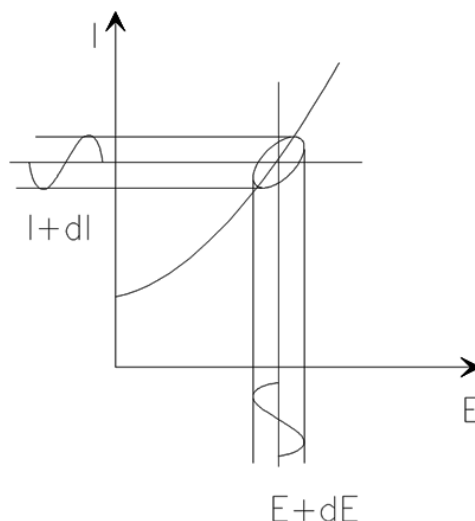


Figure 2.2 Typical Lissajous figure for an EIS ⁽³⁰⁾

The Nyquist plot, on the other hand, is the most widespread figure related to an EIS analysis. The Nyquist diagram, also known as Argand representation or Cole-Cole representation, consists of a series of points, each of which represent the magnitude and direction of the impedance vector of a particular frequency. The diagram is a complex plane of Cartesian coordinates, where the abscissa is the real part (resistive terms) and the ordinate is the imaginary part (capacitive or inductive terms). Impedance data represented on the Cartesian plane under a wide range of frequencies (100 KHz to 10 mHz, usually 10 KHz to 0.1 mHz) generate typical configurations according to the predominant electrochemical mechanism.

The Bode diagram consists of an orthogonal axes plane, that shows two quantities on the ordinate axis: the logarithm of the impedance ($\log|Z|$) in ohms (Ω) and the phase angle (Φ) in degrees; the abscissa axis is scaled accordingly to the logarithm of frequency ($\log f$), with f in Hertz.

In many cases the Bode plot is separated into two plots: one that only provides the variation of the impedance with the frequency while the second one reports the variation in angle shift. ⁽³⁴⁾

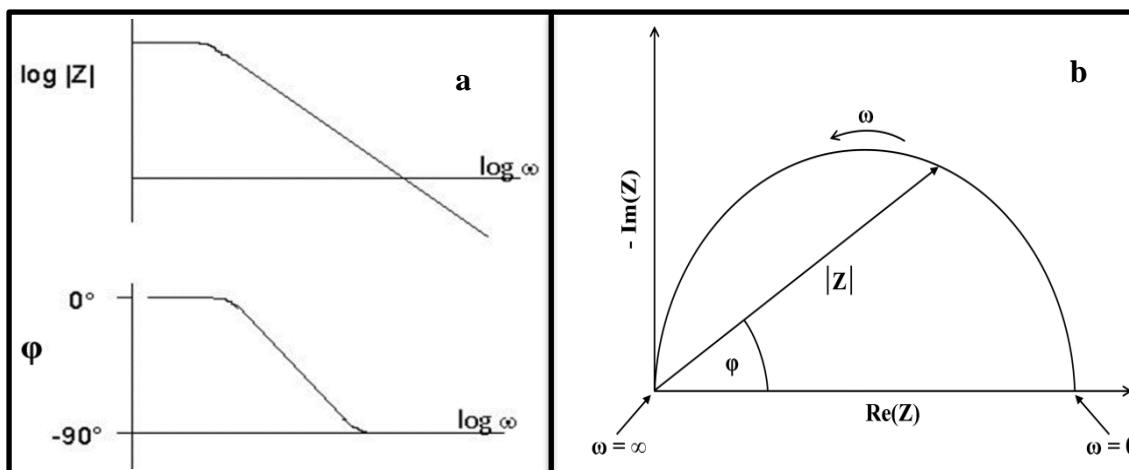


Figure 2. 3: a) Bode Plot, b) Nyquist Plot ⁽³⁵⁾

2.1.3 Data Interpretation: The Electrical Equivalent Circuit Theorem

EIS data are often interpreted in terms of electrical equivalent circuits (EECs). However, EECs are analogs not models, and hence the information that they can deliver on the physio-electrochemical processes involved is very limited. ⁽³⁶⁾

There may be good reasons to carry out measurement modelling (e.g., fitting to an equivalent circuit) and then process modelling (extracting the kinetic parameters), but fitting data to equivalent circuits is the most followed approach since most commercial software packages for fitting impedance data are based on equivalent circuits.

In order to appropriately use the EECs, it is important to know which types of mechanism correspond to a given type of equivalent circuit. This is a difficult problem, since the correspondence between circuit elements and kinetic parameters is complicated and often counterintuitive. ⁽³⁷⁾

Typically, several cell elements and cell characteristics contribute to the system's EIS spectrum. A partial list of possible elements includes:

- Electrode Double Layer Capacitance
- Electrode Kinetics
- Diffusion Layer
- Solution Resistance

Unfortunately, the system's impedance at any given frequency usually depends on more than one cell element. This greatly complicates the analysis of EIS spectra.

Aspects of the underlying mechanism can be deduced from the numbers of capacitances, inductors and resistors, the presence or absence of a DC path, and the presence or absence of inductive behavior.

The three most common electronic circuit elements in electronics and electrochemistry are the resistor, capacitor, and inductor. The resistor, which defines resistance, is often denoted by the letter R, and has the unit of Ohm (Ω). In literature, resistance can often be sub classified as polarization resistance and ohmic resistance.

The capacitor, which is often defined as reactance, is denoted by the letter C, and has the unit of Farad (F). Just as the resistance, the capacitance can refer to both to double layer and coating capacitance.

Lastly, the inductor, which defines inductance, is denoted by the letter L, and carries the unit of Henry (H). They are defined in the frequency domain by their impedances via the following equations where $\omega = 2\pi f$.

From the above equations, it is easily seen that the impedance of a is independent of frequency while the capacitor and inductor show impedances both inversely and directly proportional to the frequency applied (respectively).

In the Nyquist plot, in which the resistor would exist only as a single point on the real impedance plane, the capacitor would begin at origin and extend only in the negative imaginary impedance direction, and finally the inductor would begin at the origin and extend into the positive imaginary impedance direction. ⁽³⁸⁾

Some other elements that are frequently encountered while using the EECs are the Warburg Impedance and the Constant Phase Element (CPE).

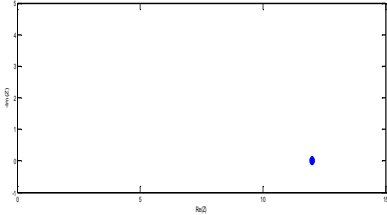
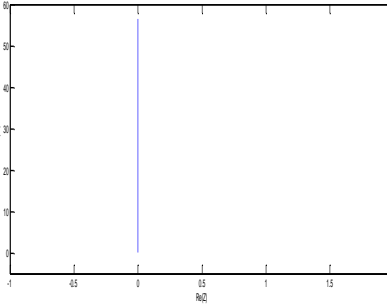
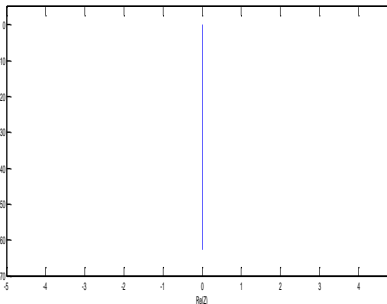
The Warburg Impedance models the diffusion of ionic phases at the interface. Several expressions, based on different assumptions, are used to describe diffusion impedance. The definition stated above is made under the assumption of semi-infinite diffusion layer. The Y_0 term is the diffusion admittance.

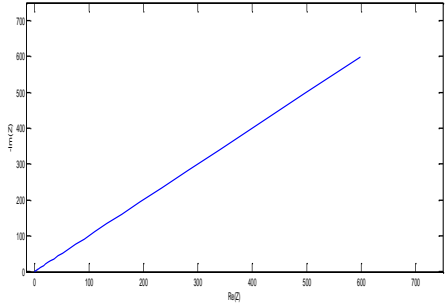
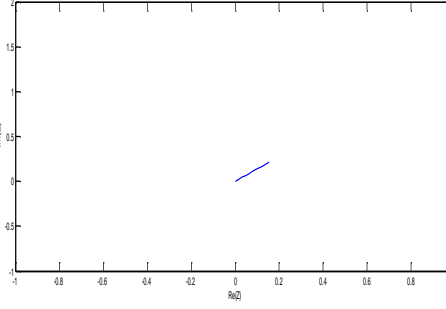
A Warburg impedance is characterized by having identical real and imaginary contributions, resulting in a phase angle of 45° .

The CPE, on the other hand, serves to account for the non-ideality of the capacitor. In this case Y_0 is the admittance of an ideal capacitance and n is an empirical constant, ranging from 0 to 1. It is noteworthy that when $n=1$, the CPE behaves as a pure capacitor, while when $n=0$, the CPE behaves as a pure resistor. Furthermore, when $n=0.5$, the CPE is the equivalent of the so-called Warburg element. ⁽³⁹⁾

Table 2.1 shows the respective equation for each of the elements described in this section.

Table 2.1 Equations for some specific elements

<u>Element</u>	<u>Equation</u>	<u>Nyquist Representation</u>
Resistor	$Z_R(\omega) = R$	 <p>The Nyquist plot for a resistor shows a single point on the real axis. The horizontal axis is labeled 'ReZ' and ranges from 0 to 15. The vertical axis is labeled 'ImZ' and ranges from 0 to 4. A single blue dot is plotted at approximately (12, 0).</p>
Capacitor	$Z_C(\omega) = \frac{1}{j\omega C}$	 <p>The Nyquist plot for a capacitor shows a vertical line on the negative imaginary axis. The horizontal axis is labeled 'ReZ' and ranges from -1 to 2. The vertical axis is labeled 'ImZ' and ranges from 0 to 60. A blue vertical line is plotted at ReZ = 0, extending from ImZ = 0 down to approximately ImZ = -55.</p>
Inductor	$Z_L(\omega) = j\omega L$	 <p>The Nyquist plot for an inductor shows a vertical line on the positive imaginary axis. The horizontal axis is labeled 'ReZ' and ranges from -5 to 5. The vertical axis is labeled 'ImZ' and ranges from 0 to 80. A blue vertical line is plotted at ReZ = 0, extending from ImZ = 0 up to approximately ImZ = 75.</p>

<p style="text-align: center;">Warburg Impedance</p>	$Z_W(\omega) = \frac{1}{Y_o \sqrt{j\omega}}$	
<p style="text-align: center;">CPE</p>	$Z_Q(\omega) = \frac{1}{Y_o(j\omega)^n}$	

2.2 Equipment for EIS Data Acquisition

2.2.1 Traditional Instrumentation

A typical electrochemical impedance experimental setup consists of an electrochemical cell (the system under investigation), a potentiostat/galvanostat, and a frequency response analyzer (FRA). The FRA applies the sine wave and analyses the response of the system to determine the impedance of the system.

The electrochemical cell, the element to be analyzed, can consist of two, three, or four electrodes. The most basic form of the cell has two electrodes. Usually the electrode under investigation is called the working electrode, and the electrode necessary to close the electrical circuit is called the counter electrode. The electrodes are usually immersed in a liquid electrolyte. For solid-state systems, there may a solid electrolyte or no electrolyte.

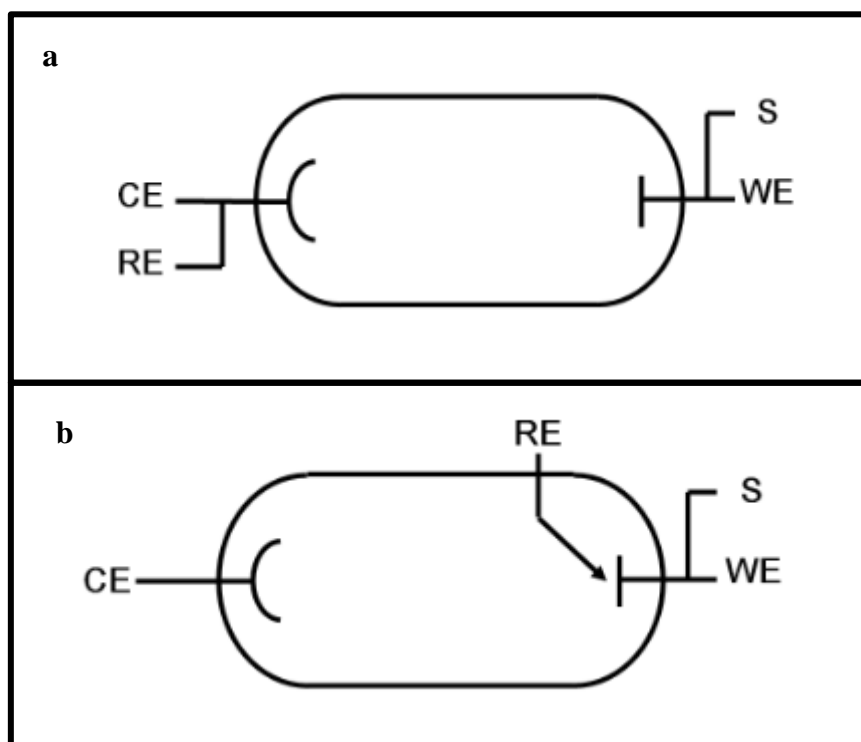
A two-electrode configuration for the cell is used when precise control of the potential across the electrochemical interface is not critical, figure 2.4.a. This arrangement is used to investigate electrolyte properties, such as conductivity, or to characterize solid-state systems. The impedance is measured between the RE and the S.

A three-electrode configuration for an electrochemical cell is most common for typical electrochemical applications. A third electrode (the reference electrode) is used to determine the potential across the electrochemical interface accurately (see Figure 2.4.b).

Since the absolute potential of a single electrode cannot be measured, all potential measurements, in electrochemical systems are performed with respect to a reference electrode. A reference electrode, therefore, should be reversible, and its potential should remain constant during the course of the measurement. The impedance is measured between the RE and the S.

A four-electrode cell is used to analyze processes occurring within the electrolyte, between two measuring electrodes separated by a membrane. In this configuration, the working electrode and the counter enable current flow (see Figure 2.4.c).

EIS measurements can be done in the potentiostatic or galvanostatic mode. In the potentiostatic mode, experiments are done at a fixed DC potential. A sinusoidal potential perturbation is superimposed on the DC potential and applied to the cell. The resulting current is measured to determine the impedance of the system.



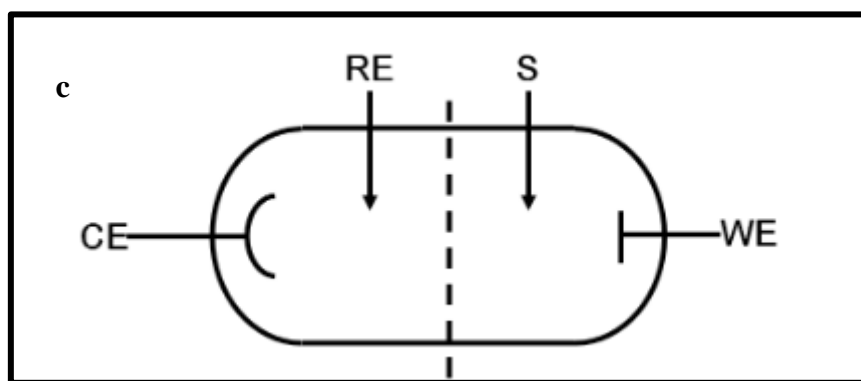


Figure 2. 4: a) Two electrode, b) Three electrode, c) Four electrode configuration

In the galvanostatic mode, experiments are done at a fixed DC current. A sinusoidal current perturbation is superimposed on the DC current and is applied to the cell. The resulting potential is measured to determine the impedance of the system. Typically impedance experiments are done under potentiostatic control. In some cases, i.e. electrodeposition at constant current and battery research, impedance experiments can be performed under galvanostatic control.

Typically, measurements are done in the single sine mode. Multi sine can be used to save time when measuring very low frequencies.

In theory one must choose the widest possible frequency range to capture all the time constants of the system. In practice the frequency range is constrained by the instrument limitations and system considerations.

The highest frequency of an impedance scan is often limited by the high frequency limit of the potentiostat and the slow response of the reference electrode. Typically, potentiostats can go up to 1 MHz.

The measurement time at each frequency is the inverse of the frequency. Hence, a very low frequency limit can result in a very long time for the collection of a complete scan. For example, the measurement of one data point at a frequency of 1 mHz will take 1000 s. For systems that are changing with time (e.g. due to corrosion, growth of a film etc.) this implies that the system has changed during the course of the data collection. Therefore, the low frequency limit should be chosen to ensure minimal change in the system during data collection.

A frequency range of 100 kHz – 0.1 Hz is typically used for most electrochemical systems. The total measurement time for this frequency range is around 10 minutes. ⁽⁴⁰⁾

2.2.2 Electronic Load as a Measurement Alternative

As said before, EIS measurements are normally carried out with the aid of a potentiostat. However, this is not the only possibility when it comes to instruments used for this type of analysis.

A very valid alternative is the use of an electronic load. While a potentiostat is an electronic instrument that controls the voltage difference between a working electrode and a reference electrode ⁽⁴¹⁾, an electronic load usually consists of a bank of power transistors mounted on a suitably sized heat sink, and cooled with fans.

An electronic circuit governs the amount of current that the power devices can draw from the power supply on test. To protect the power devices from damage, electronic loads usually have a pre-settable power limit. This electronic signal can be a voltage change, current change or frequency change depending on the type of load cell and circuitry used.

Depending whether the load is capacitive or resistive it can either change its internal resistance or capacitance. A change in resistance leads to a change in output voltage when an input voltage is applied while a change in capacitance allows the system to hold a certain amount of charge when a voltage is applied to it. ⁽⁴²⁾

For the purposes of this investigation, an Agilent 3302A load model was used. Such a device can operate in 3 different modes.

- Constant current (CC): the module will sink a current in accordance with the programmed value regardless of the input voltage.

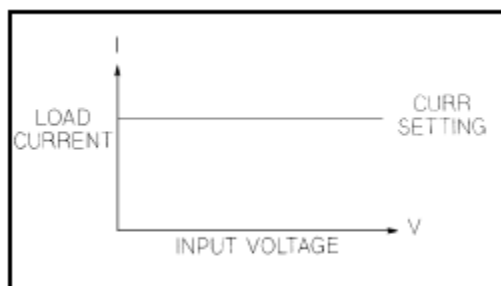


Figure 2.5 CC Mode

- Constant voltage (CV): the module will attempt to sink enough current to control the source voltage to the programmed value.

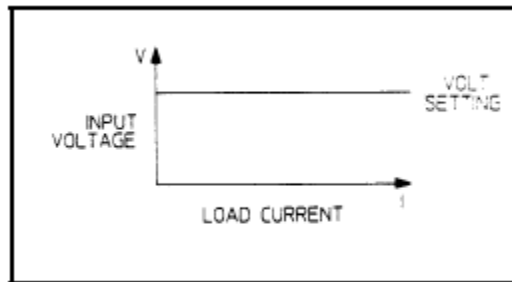


Figure 2.6 CV Mode

- Constant resistance (CR): the module will sink a current linearly proportional to the input voltage in accordance with the programmed resistance.

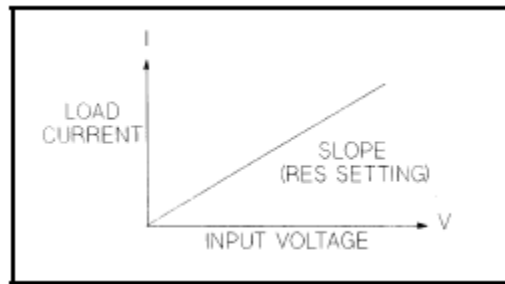


Figure 2.7 CR Mode ⁽⁴³⁾

In order to carry out an electrochemical impedance measurement the load has to be set in the constant current mode. In this way a voltage difference can be established across the capacitor as shown in figure 2.8.

Since the load by itself doesn't produce any current or voltage, a DC adapter has to be connected as the power input supply of the system if the analysis is performed on elements that do not produce energy (such as real circuits).

This, however, leads to the necessity of coupling to a wave function generator in order to obtain the required frequency dependent response. The sinusoidal wave sent into the system perturbs the current and voltage constants values passing through the load, making them thus oscillate around a desired value.

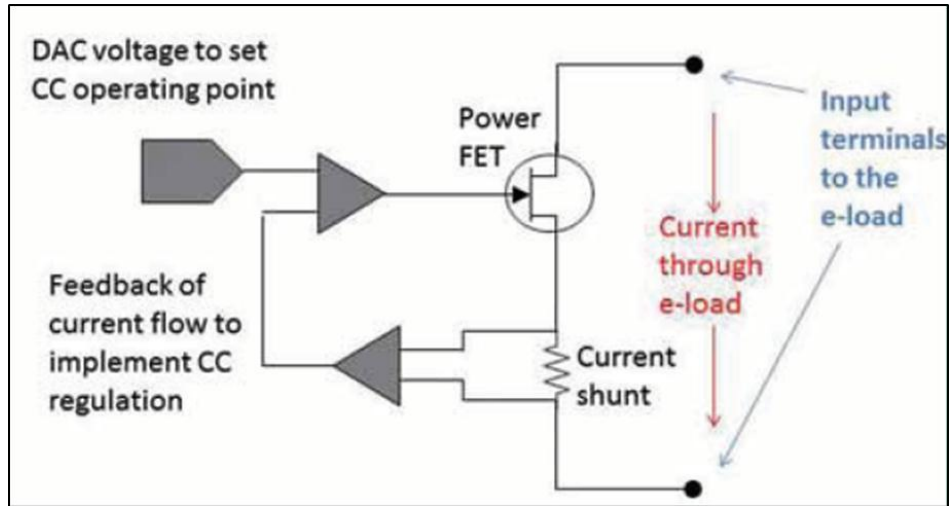


Figure 2.8 Configuration of load ⁽⁴⁴⁾

Figure 2.9.a represents the exact configuration of the system in the case a measurement is carried using a fuel cell while figure 2.9.b is the configuration required in the case the impedance analysis is done to an element not capable of producing power.

Even though it is not explicitly shown in the second images, in both cases the input command is generated remotely through a computer using the computational software Matlab.

All scripts used during experimentation can be found in Appendix A.

The frequency dependence aforementioned sets a limit to the values of the frequency that can be used though because function generator test frequency is affected by some important factors related to FFT data analysis that need to be considered before making this measurement.

In order to avoid inaccuracies during the analysis using the Fourier transforms, the usable frequencies have to be multiple of a binary frequency which can be defined as follows:

$$f_{\text{bin}} = \frac{1}{N_p t_s} \quad (2.5)$$

N_p is the number of samples taken. The FFT requires N to be an integer power of 2. Therefore, the load must be set to capture waveform data with a number of points that is an integer power of 2, with the constraint that the power n must fall within the range $1 \leq n \leq 12$.

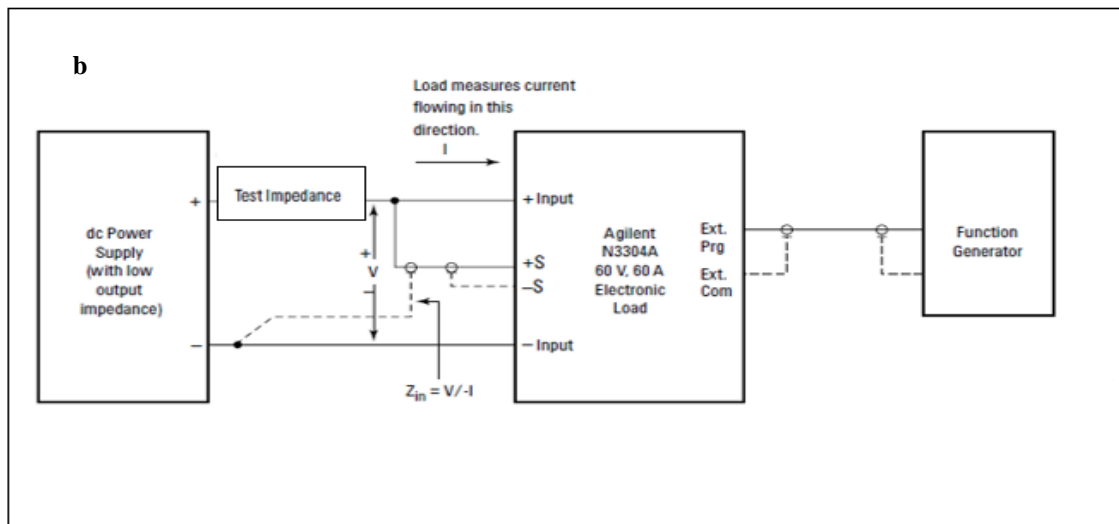
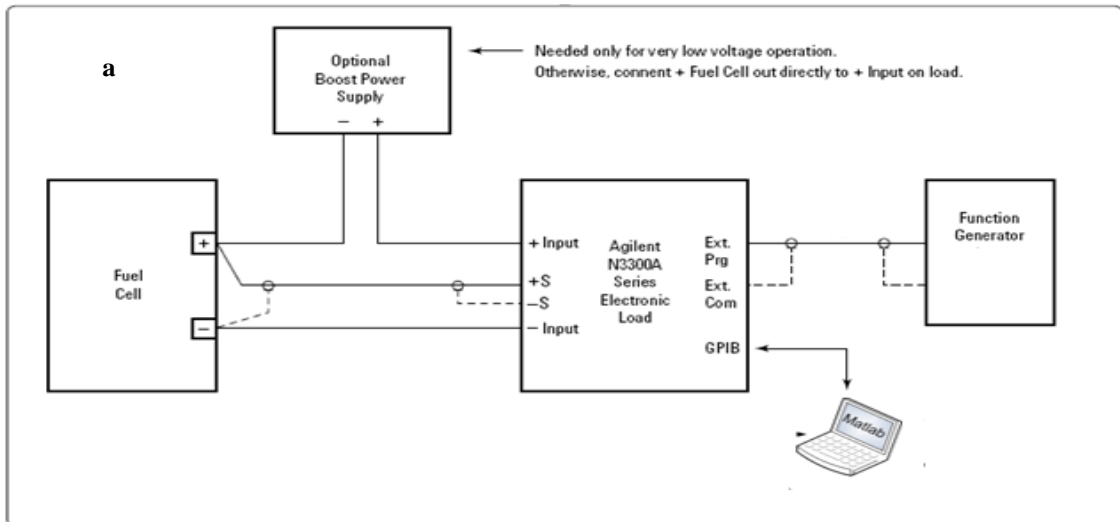


Figura 2.9: a) System Configuration using SOFC, b) System Configuration using a circuit

T_s is the time between samples. Discrete sample times are available from the load resulting in discrete sample frequencies. As mentioned earlier, the load sample rate can be adjusted between $10 \mu s$ and $0.032 s$ in $10 \mu s$ increments.

Once the binary frequency is defined, the testing frequency is implemented as an integer multiple m times f_{bin} .

$$f_{test} = m f_{bin} \quad (2.6)$$

Np=2 ⁿ fbin=1/NP*ts									
dt(us)	32	64	128	256	512	1024	2048	4096	fmax
0,00001	3125,0000	1562,5000	781,2500	390,6250	195,3125	97,6563	48,8281	24,4141	50000
0,00002	1562,5000	781,2500	390,6250	195,3125	97,6563	48,8281	24,4141	12,2070	25000
0,00005	625,0000	312,5000	156,2500	78,1250	39,0625	19,5313	9,7656	4,8828	10000
0,0001	312,5000	156,2500	78,1250	39,0625	19,5313	9,7656	4,8828	2,4414	5000
0,0002	156,2500	78,1250	39,0625	19,5313	9,7656	4,8828	2,4414	1,2207	2500
0,0005	62,5000	31,2500	15,6250	7,8125	3,9063	1,9531	0,9766	0,4883	1000
0,001	31,2500	15,6250	7,8125	3,9063	1,9531	0,9766	0,4883	0,2441	500
0,002	15,6250	7,8125	3,9063	1,9531	0,9766	0,4883	0,2441	0,1221	250
0,005	6,2500	3,1250	1,5625	0,7813	0,3906	0,1953	0,0977	0,0488	100
0,01	3,1250	1,5625	0,7813	0,3906	0,1953	0,0977	0,0488	0,0244	50
0,02	1,5625	0,7813	0,3906	0,1953	0,0977	0,0488	0,0244	0,0122	25
0,032	0,9766	0,4883	0,2441	0,1221	0,0610	0,0305	0,0153	0,0076	15,63

Figure 2.10 Frequency variation accordingly to Np

The value of m has to be less or equal to 2⁽ⁿ⁻¹⁾ in order to have a congruent measurement. Otherwise spectral leakage will occur causing inaccuracies in the results of the FFT calculation.

It is to be remarked that the maximum frequency value that can be tested is independent of the binary frequency:

$$f_{\max} = \frac{1}{2t_s} \quad (2.7)$$

Figure 2.10 shows how frequencies vary depending on N_p and t_s. As it can be observed from the highlighted values, some of them can be repeated through different combinations of these two parameters, confirming in this way that f_{test} is multiple of a given frequency. (45)

2.3 Ionic Conductivity Measurements

2.3.1 Conductivity in MIEC Materials

One way to evaluate a MIEC membrane is to determine the oxygen ionic conductivity, which is an intrinsic material property and can be obtained from the oxygen flux data by using the following equation:

$$\sigma_{\text{ion}}(P''_{\text{O}_2}) = -\frac{4^2 F^2 L}{RT} \left[\frac{dj_{\text{O}_2}}{d \ln P''_{\text{O}_2}} \right]_{P'_{\text{O}_2} = \text{constant}} \quad (2.8)$$

J_{O_2} is the oxygen flux, R the gas constant, T the absolute temperature, F the Faraday constant, L the membrane thickness, σ_{ion} the oxygen ionic conductivity, P'_{O_2} the oxygen partial pressure at the feed side and P''_{O_2} the oxygen partial pressure at the sweep side of the membrane.

For calculating σ_{ion} of a membrane from oxygen flux data, it is in most cases assumed that the oxygen partial pressure at the outlet has the same value as the oxygen partial pressure on the membrane surface. In other words, it is assumed that the oxygen permeation set-up works as a continuous stirred-tank reactor (CSTR), which means a perfect mixing of both nitrogen/oxygen in the feed (air) compartment and sweep gas/oxygen in the permeate compartment. However, the validity of the CSTR assumption depends on the reactor geometry as well as operating parameters. ⁽⁴⁶⁾

The mechanism of oxygen permeation through these membranes is outlined in Fig. 2.11.a. First, gas-phase molecular oxygen on the oxygen-rich side diffuses to the membrane surface where it is adsorbed. The adsorbed oxygen then withdraws two electrons from the membrane and dissociates into oxygen ions.

Driven by the oxygen partial pressure gradient across the membrane, the oxygen ions diffuse across the membrane bulk to the membrane surface on the oxygen-poor side, where they recombine with electron holes to form adsorbed molecular and atomic oxygen.

Finally, the molecular oxygen is desorbed into the gas phase on the oxygen-poor side. High oxygen surface-exchange kinetics and a high rate of oxygen diffusion through the membrane bulk are, therefore, crucial to achieving superior oxygen fluxes through a membrane with a given thickness and a given transmembrane oxygen partial pressure gradient.

During fuel cell operation, the reduction of oxygen is strictly limited to the electrode–electrolyte–gas triple phase boundary, and sharp increases in electrode polarization resistance are typically observed at lower operating temperatures. Applying a mixed ionic and electronic conducting (MIEC) oxide as an electrode should allow for the oxygen reduction sites to penetrate into the electrode bulk to a finite depth.

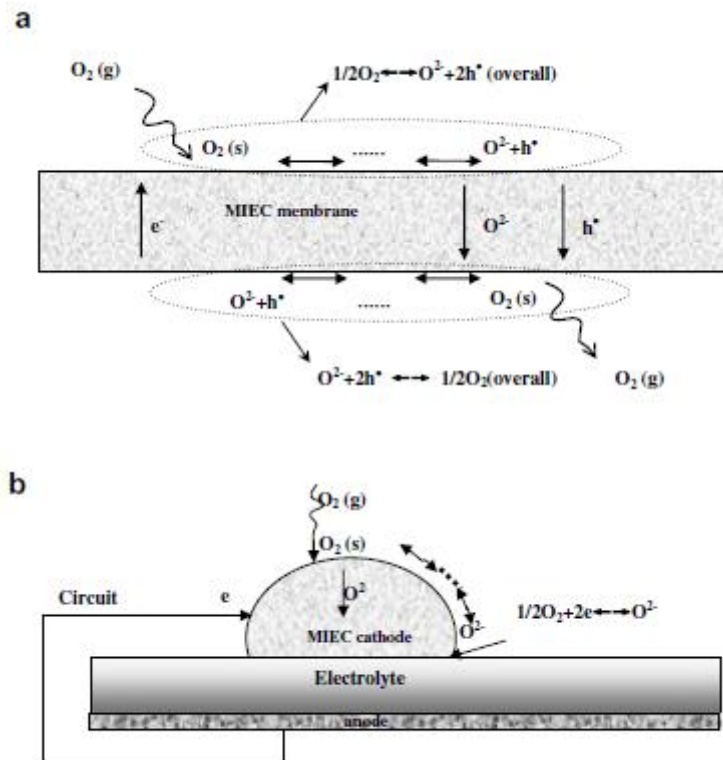


Figure 2.11 a) mechanism of oxygen permeation b) mechanism of activation

The mechanism of oxygen activation at a MIEC cathode is depicted in Fig. 2.11.b. The pertinent reactions involve both oxygen surface exchange and bulk diffusion processes. Oxygen surface sorption and bulk diffusion limit the characteristic depth of oxygen reduction in porous MIEC electrodes.

Membrane permeability was assessed using a high-temperature oxygen permeation apparatus via the gas chromatography (GC) method. ⁽⁴⁷⁾

2.3.2 Permeation Cell Setup

Even though several permeation cell setups can be found in literature, all of them have some common functioning principles. There is always a sweep gas sent to one of the sides of the material, which catches the oxygen that passes ionically from the other side. Figures 2.12.a-c schematize the aforementioned configuration

The sweep gas/oxygen mixture is then usually sent to a gas chromatographer in order to analyze its composition

In the first figure, the sweep gas inlet and outlet can be seen. Helium coming into the system goes up a tube that is positioned one centimeter below the ceramic button through which oxygen is expected to pass.

The holder supporting the sample is placed above the sweep gas inlet and glued with a silicon paste in order to seal the passage of gas from and to the outside. It is of extreme importance that no gas passes through, otherwise composition is no longer countable (oxygen may come in or out altering the results).

Atop the sample holder, a ceramic shell with three holes is placed. These holes are used to connect the air inlet, the air outlet and a thermocouple that will eventually assess the temperature. Sealing for this section is not as important because oxygen migration is not dependent on the quantity sent to the sample.

In order to heat the system (figure 2.12.c), an oven is placed around the previously described gadgets together with some resistances to bring to temperature. The oven is thermally isolated with quartz wool.

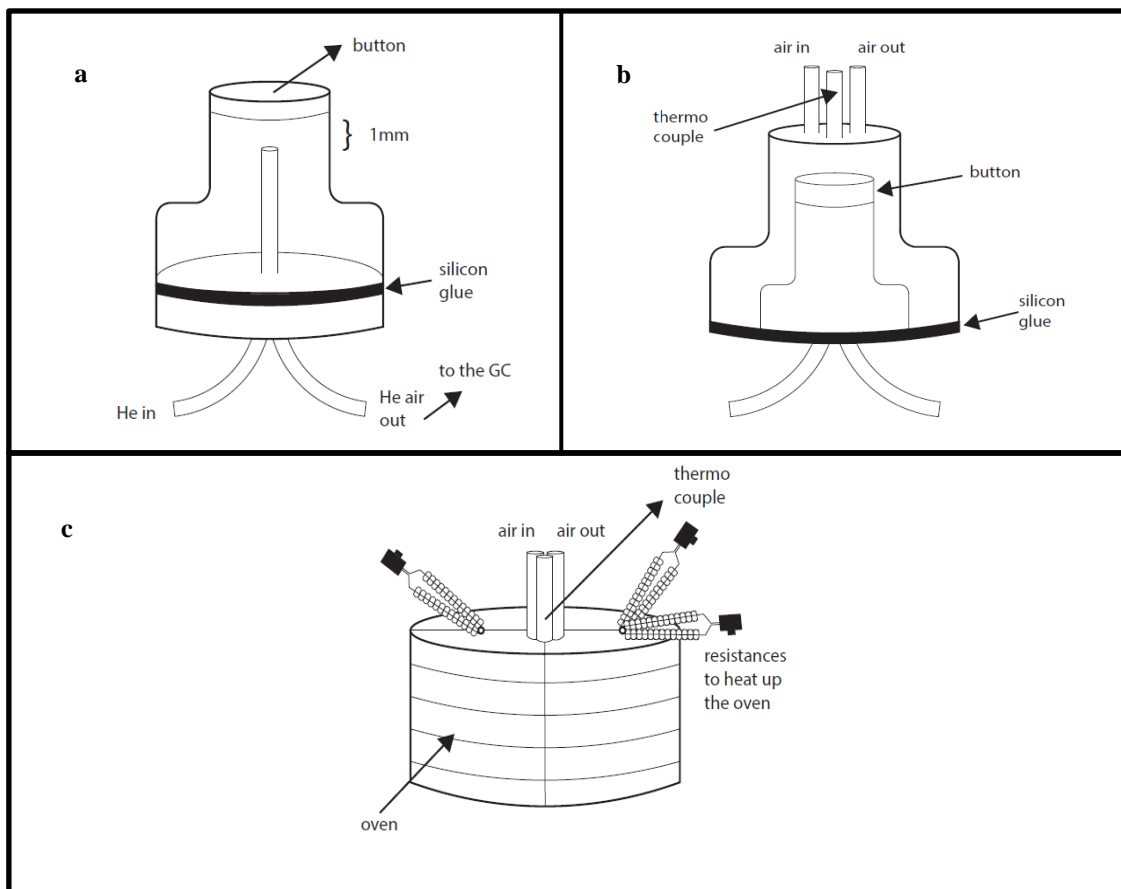


Figure 2.12 Setup of permeation cell

2.3.3 Principles of Gas Chromatography

Chromatography is a commonly used analytic technique that analyzes the volatile substances in a gas phase. It allows the separation of a mixture of compounds (solutes) into separate components. By separating the sample into individual components, it is easier to identify and measure the amount of the various sample components.

In gas chromatography, there is a mobile phase, also known as carrier, which flows through a column containing a stationary phase.

The selection of the carrier depends on different parameters such as chemical-physical characteristics and cost among others. Yet, it is essential for the mobile phase to have a chemical inertia with respect to the stationary phase and the components to be analyzed. For this reason, noble gasses are usually a good choice when it comes to carriers.

The stationary phase, on the other hand, is placed inside a column that can be either a packed or capillary. In both cases, the materials employed are the same and the choice depends on many variables. (48)

Packed columns contain a finely divided, inert, solid support coated with liquid stationary phase. Most packed columns are 1.5 - 10m in length and have an internal diameter of 2 - 4mm.

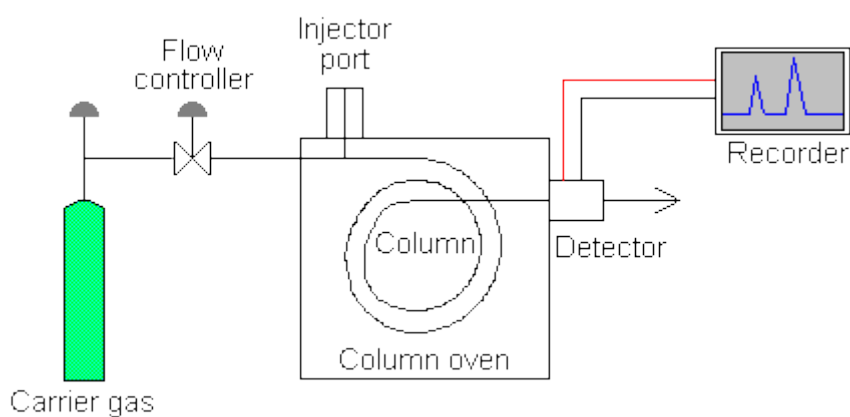


Figure 1.13 Configuration of a GC

Capillary columns have an internal diameter of a few tenths of a millimeter. They can be one of two types; *wall-coated open tubular* (WCOT) or *support-coated open tubular* (SCOT). Wall-coated columns consist of a capillary tube whose walls are coated with liquid stationary phase. In support-coated columns, the inner wall of the capillary is lined with a thin layer of support material such as diatomaceous earth, onto which the stationary

phase has been adsorbed. SCOT columns are generally less efficient than WCOT columns. Both types of capillary column are more efficient than packed columns. (49)

As can be observed from figure 2.13, the carrier gas flows into the injector, through the column and then into the detector. Simultaneously the sample is introduced into the injector with a syringe or an exterior sampling device. The injector is usually heated to 150-250°C, which causes the volatile sample solutes to vaporize. The vaporized solutes are transported into the column by the carrier gas.

The column is maintained in a temperature controlled oven. The solutes travel through the column at a rate primarily determined by their physical properties, and the temperature and composition of the column. The various solutes travel through the column at different rates. The fastest moving solute exits (elutes) the column first then is followed by the remaining solutes in corresponding order. As each solute elutes from the column, it enters the heated detector. An electronic signal is generated upon interaction of the solute with the detector.

The size of the signal is recorded by a data system and is plotted against elapsed time to produce a chromatogram.

The main parts of a basic GC system are shown in figure 2.14.



Figure 2.14 Parts of a GC

The ideal chromatogram has closely spaced peaks with no overlap of the peaks. Any peaks that overlap are called coeluting. The time and size of a peak are important in that

they are used to identify and measure the amount of the compound in the sample. The size of the resulting peak corresponds to the amount of the compound in the sample. A larger peak is obtained as the concentration of the corresponding compound increases.

If the column and all of operating conditions are kept the same, a given compound always travels through the column at the same rate. Thus, a compound can be identified by the time required for it to travel through the column (called the retention time).

The identity of a compound cannot be determined solely by its retention time. A known amount of an authentic, pure sample of the compound has to be analyzed and its retention time and peak size determined. This value can be compared to the results from an unknown sample to determine whether the target compound is present (by comparing retention times) and its amount (by comparing peak sizes).

If any of the peaks overlap, accurate measurement of these peaks is not possible. If two peaks have the same retention time, accurate identification is not possible. Thus, it is desirable to have no peak overlap or co-elution. ⁽⁵⁰⁾

CHAPTER 3

EXPERIMENTAL AND RESULTS

3.1 Implementation of EIS using an E-load

3.1.1 Validation of the Method through Synthetic Waves

Validation of the method is the critical issue when it comes to nontraditional techniques for Electrochemical Impedance Spectroscopy (EIS). Comprehension of Fourier Transforms (FFT) is a key point to construct such a method.

The e-load configuration reported in chapter 2 serves only to represent the assemblage of the instrumentation used for this type of measurements. For it to carry out the spectroscopy, the necessity of a remote program that commands the load is fundamental.

However, before being able to analyze any real-life element, it must be determined whether such a program can return the actual value of the impedance. By using Matlab as interface and the knowledges discussed in precedence, it is possible to verify this.

Models for real element circuits, as well as their respective Nyquist and Bode plots, can be easily found in literature. Such circuits were used during this research as reference for the validation.

Considering that the aim of this first part is only to confirm the script works, all variables that cannot be controlled were eliminated to discern if the method effectively gives the expected results. This was done by creating a series of both voltage and current sinusoidal waves instead of using real waves.

The use of fictitious waves is desirable because it allows to define the amplitude of current and voltage as well as the phase shift between the two waves. These parameters are essential during the FFT because by definition, impedance is the ratio of the transform of the voltage and the transform of the current. Consequently, the returning value of Z will vary accordingly to the values assigned to these parameters.

The main script, which is called *EIS_test*, can be described as follows: it calls within its frame two functions, *freqrespmeasure* and *Impedenza*, that return specific values that the script will then graphically compare.

Impedenza is the first function to be called. Its only purpose is to define models of impedance that are well known in literature without the need of sinusoidal waves but depend only on the values of the circuit elements (such as those present in table 2.1).

The second function is freqrespmeasure and this is the one that carries out all the calculations for the FFT. Even though not complicated by itself, this function is less counterintuitive than the precedent.

Given two variables x and y , which in this case are voltage and current respectively, the function gives back the absolute value of the impedance (Amp), the shift between the two waves (Ph), and finally the real and the imaginary part of the impedance (Z_{Re} and Z_{Im}).

It starts by calculating the FFT which takes a time-based pattern, measures every possible cycle, and returns the amplitude, offset, and rotation speed for every cycle that was found. Subsequently it determines the cycle with the biggest amplitude (for both current and voltage) and calculates the value of Z using the values relative to these cycles.

Once that these two functions have been described, understanding the main script is very simple. Eis_test calls Impedenza to calculate a 'theoretical' value of impedance, then it defines the synthetic waves of current and voltage by assigning an arbitrary value of amplitude. However, the phase shift between these two waves is obtained through the impedance value given by Impedenza.

Once that both synthetic waves have been defined, freqrespmeasure takes and Fourier transform them in order to calculate impedance in a different way that then is returned to the main script. The values of Z are then compared to see if they both yield the same results.

Figure 3.1-8 show that the method established for the calculation of the impedance effectively returns the desired values. Each figure obtained represents first the Nyquist plot and then the Bode plot. Unlike its most common representation where the two plots are one atop of the other, here the variation of the module of the impedance is placed next the variation of the phase shift. Both these parameters are a function of frequency.

The label original in the legend of the figures stands for the values retrieved through the formula (Impedenza), while from I,V are the values obtained through the use of the FFT.

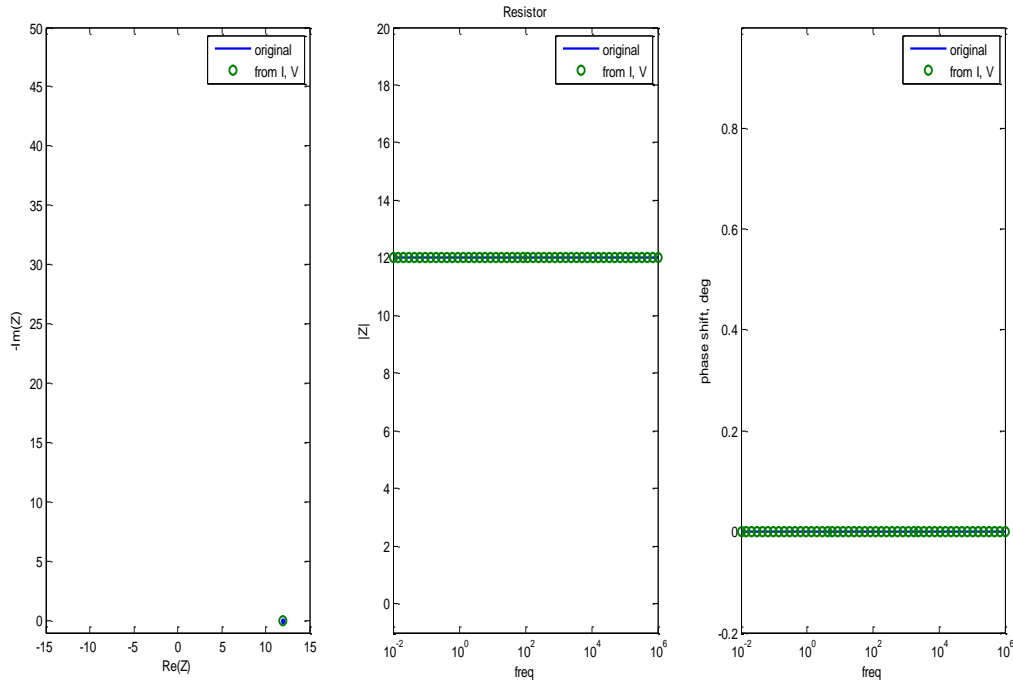


Figure 3.1 Resistor

Figure 3.1 represents the behavior of a resistor with $R= 12 \Omega$. In this case the imaginary part of the impedance is non-existing while the real part has the same value as the resistance. For this reason, impedance (and consequently also the phase shift) is independent of frequency.

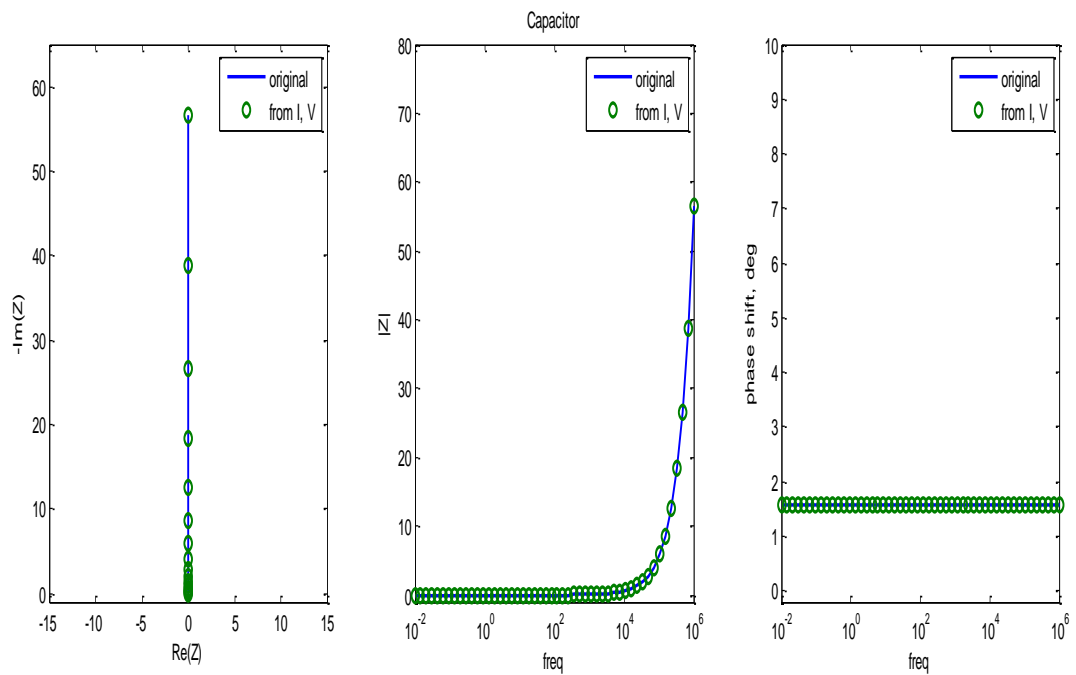


Figure 3.2 Capacitor

Figure 3.2 shows the behavior of a capacitor with $C= 9 \times 10^{-6}$ F. Differently from the previous case, here only an imaginary part of Z is present (Z real=0). This leads to a variation of the module of impedance at very high frequencies and a constant value of phase shift, which now is different from 0.

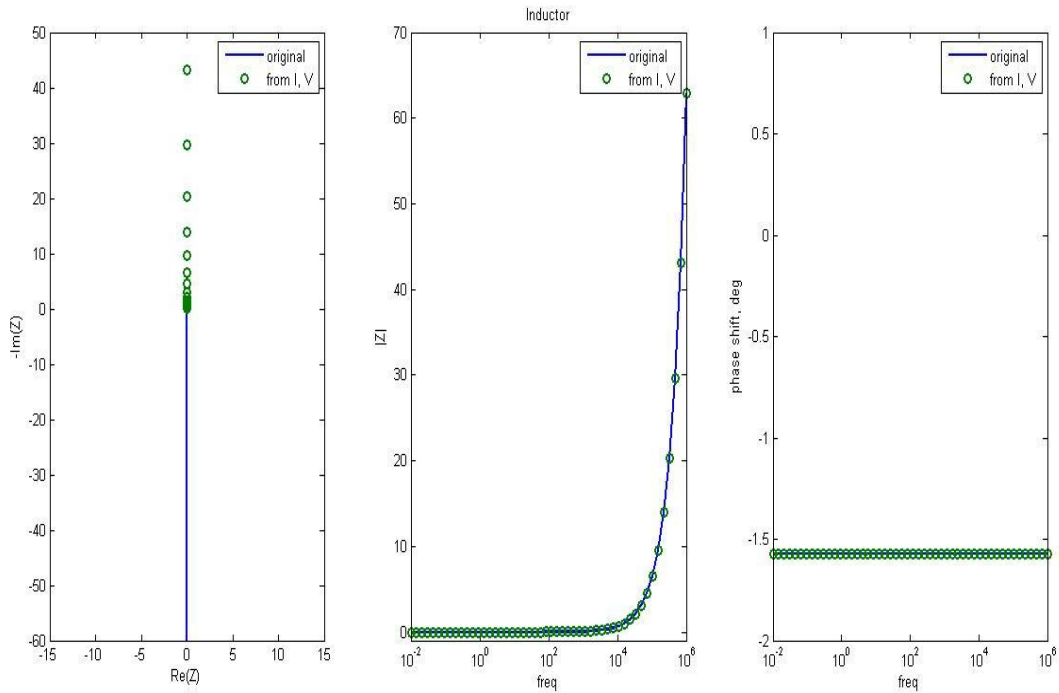


Figure 3.3 Inductor

Figure 3.3 represent the plots of an inductor. This is the only case in which the program was not able to deliver an accurate Nyquist plot. In the case of the inductor we obtain plots very similar to those of the capacitor but with opposite sign for the phase shift and Nyquist plot. However, here it can be seen that the FFT method gives back the correct numerical value of Z imaginary but negative instead of positive. The inductance simulated was $L=10 \times 10^{-6}$ F.

Figure 3.4 is the Randles circuit, a circuit composed by a resistor in series to a resistor and a capacitor in parallel. The R in series is equal to 100Ω while the one in parallel is 12Ω . It must be noticed that the sum of the two resistances gives the maximum value of impedance while the value of the parallel resistance is the minimum value of Z . The capacitance is $C= 9 \times 10^{-6}$ F. In this case it can be seen that both the phase shift and Z imaginary start from 0, then arrive to a maximum point before going back to zero again.

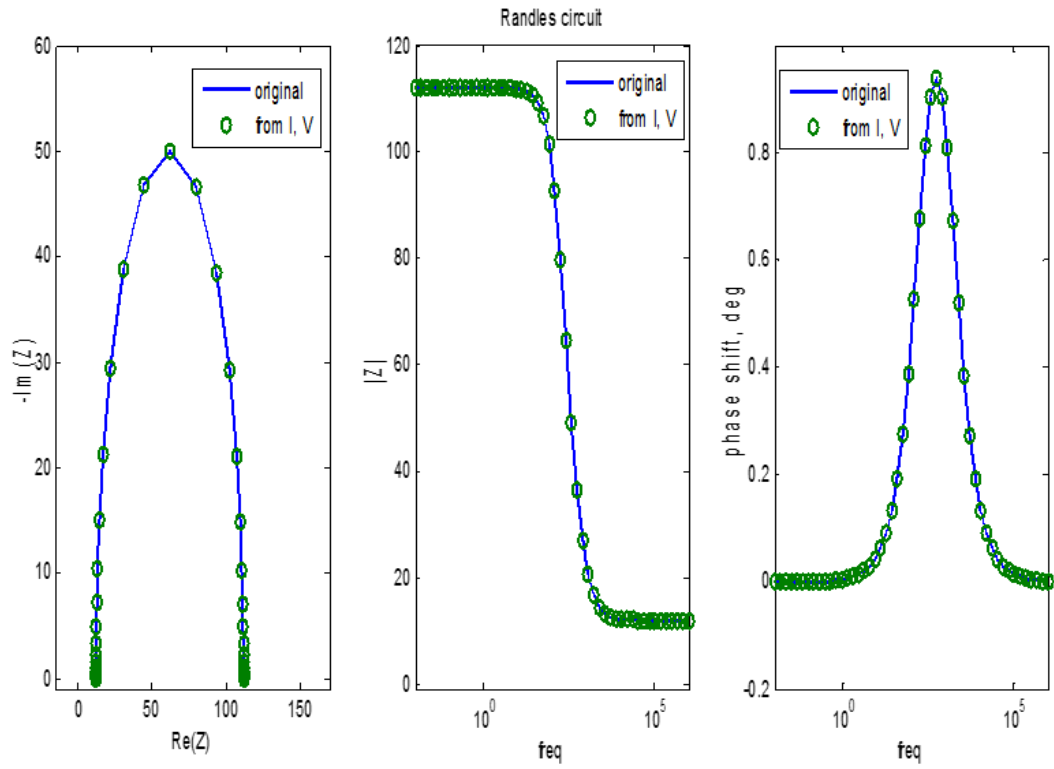


Figure 3.4 Randles Circuit

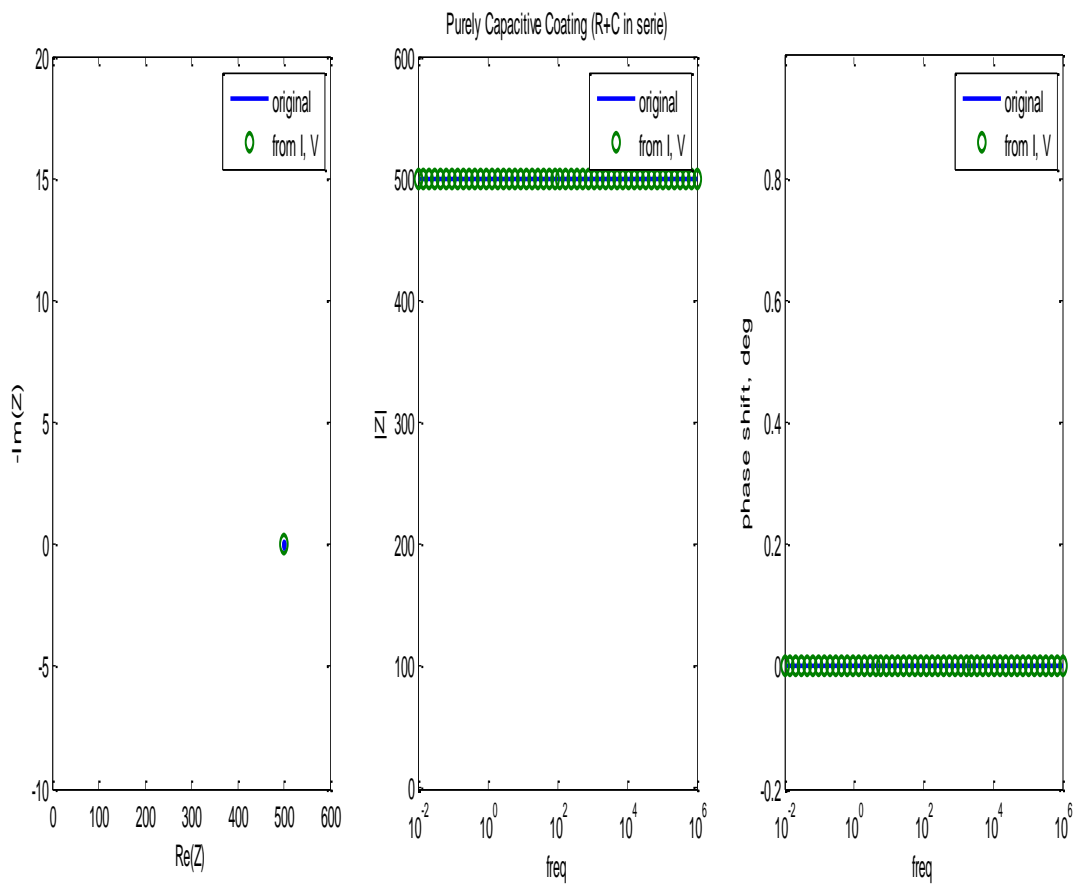


Figure 3.5 RC in series

Figure 3.5 represents a RC series circuit with $R=500 \Omega$ and $C= 2 \times 10^{-10} \text{ F}$. The profiles obtained are an in-between of the single resistance and the single capacitor. The phase shift is still zero and the impedance assumes the value of R, yet in the Nyquist plot an imaginary component, which is typical of capacitors and non-existing in resistances, can be observed.

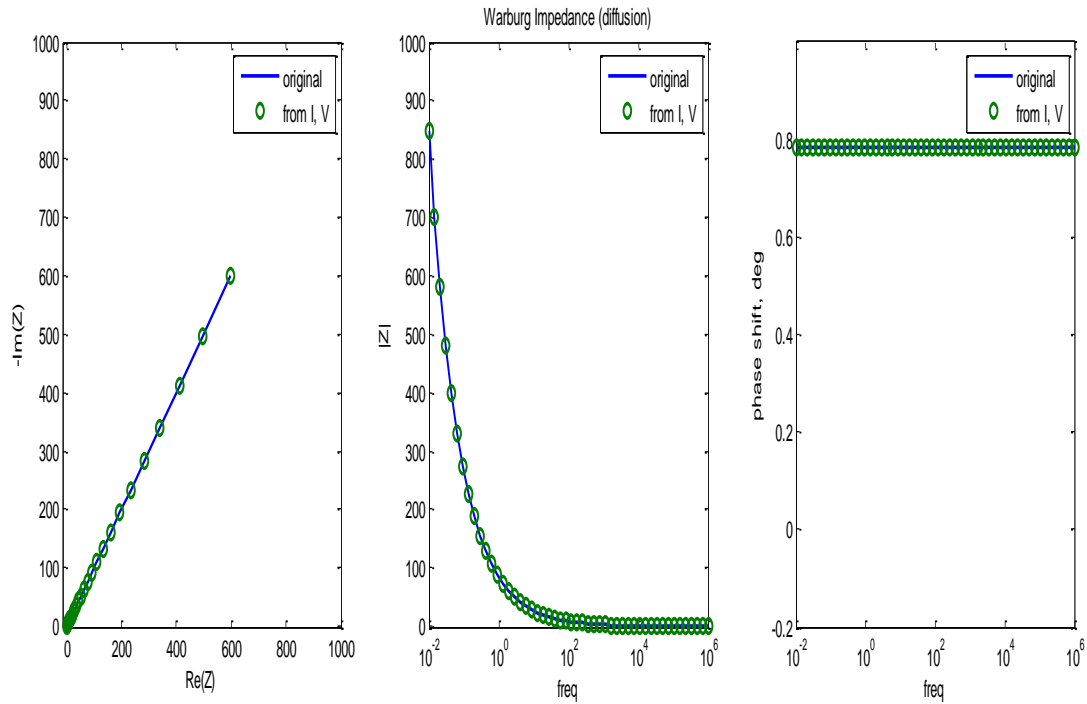


Figure 3.6 Warburg Impedance

Figure 3.6 is the Warburg impedance, that means the presence of diffusive phenomena in the system. The Nyquist plot is characterized by a 45-degree line while the resistance diminishes with the rise in frequency. The phase shift remains invariant.

Figure 3.7 is the representation of the mixed kinetic and diffusive control. Such system can be described through a Randles circuit (as the one explained in figure 3.4) but containing a Warburg impedance in series to the parallel resistance. The plots obtained are, consequently, a combination of the plots obtained for these two cases.

The last system taken into consideration is depicted in figure 3.8 is typical of the failed coatings. From a circuitual point of view it can be thought of as a resistance in series followed by R in series to a RC parallel circuit which is parallel to a capacitor. Here two

arches and two phase shift peaks can be observed, which is a normal characteristic of system possessing two different time constants.

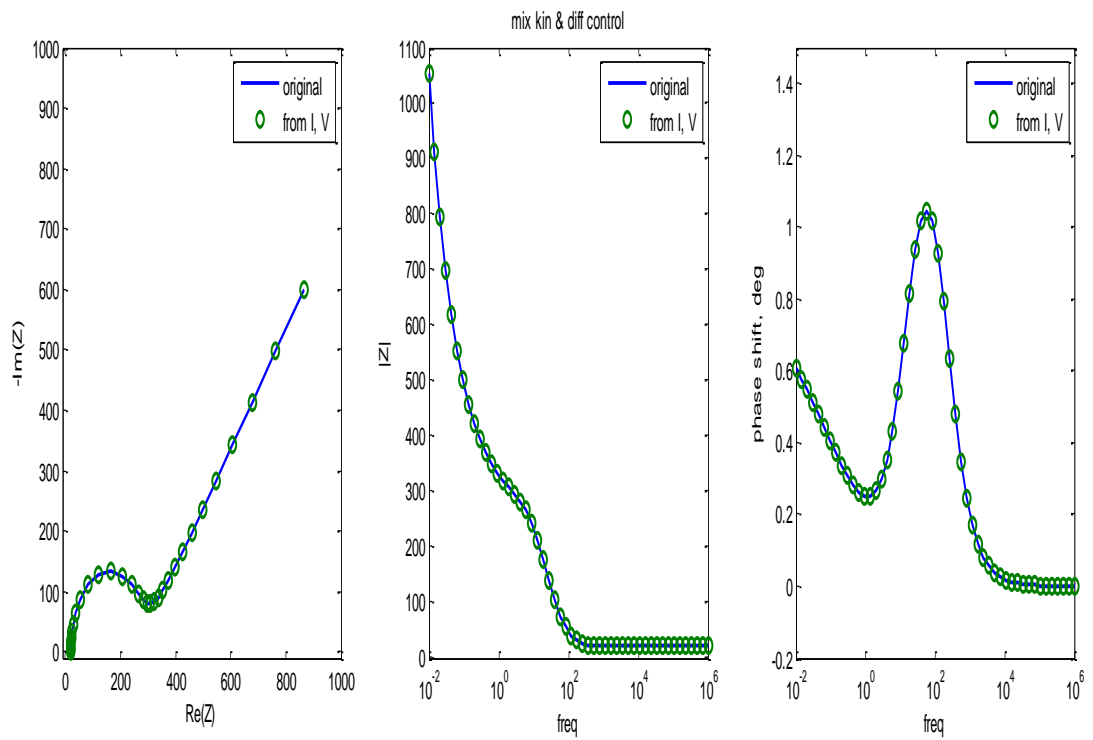


Figure 3.7 Mixed Kinetic and Diffusive control

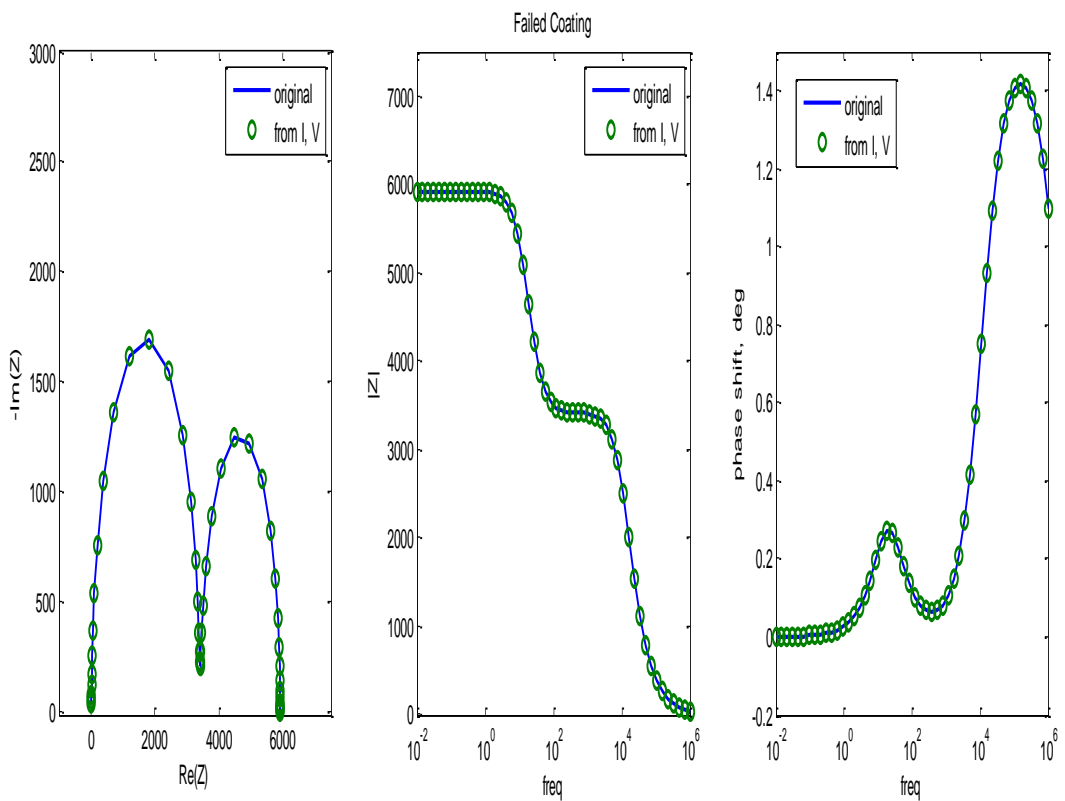


Figure 3.8 Failed Coating

3.2 Real Systems Measurements

3.2.1 Analysis of Real Circuital Elements

Once that the data elaboration program has been redeemed as trustworthy the next logical step is to verify the accuracy of the electronic load. Since this instrument was not designed for this purpose, it must be verified whether the values of impedance obtained correspond to those expected for each specific circuit.

Also in this case Matlab was used, this time as the interface. Some of the programs described in the precedent section were re-used for data elaboration. In specific, `freqrespmeasure` and `Impedenza` are used for the same purposes as before. There are also some other scripts that feature inside the main script that won't be explicitly nominated due to their nature as libraries for the control of the wave generator.

Script **EIS_measurement_1** involves a greater difficulty due to the necessity of creating a communication with the load using SCPI.

SCPI (Standard Commands for Programmable Instruments) is a programming language for controlling instrument functions over the GPIB and RS-232 interface. SCPI is layered on top of the hardware-portion of IEEE 488.2. The same SCPI commands and parameters control the same functions in different classes of instruments.

SCPI has two types of commands, common and subsystem:

- Common commands generally are not related to specific operation but to controlling overall electronic load functions, such as reset, status, and synchronization. All common commands consist of a three-letter mnemonic preceded by an asterisk
- Subsystem commands perform specific electronic load functions. They are organized into an inverted tree structure with the "root" at the top.

The first commands serve to establish a connection with the load, followed by the frequency set to be scanned. The program registers all signals stemming from the load and then calls the function `freqrespmeasure` in order to comply with the FFT calculations.

Of vital importance are the commands relative to the sensibility of the ranges, and how the load reads both current and voltage. In the first case, the delivered results may turn

out as noise if sensibility is not compatible with the values expected (they are either too low or too high).

The reading of current and voltage, on the other hand, is strictly related to commands FETch and MEASure. Coupling of these two instructions in the wrong way generates poor results (if not completely inexact) and their use is not as straightforward as their meaning may suggest.

The most logical combination would be to call for a measurement of current and voltage followed by the fetch of such measurements. Yet proceeding in this way causes an override of the data saved in the buffer resulting in not comparable information being analyzed.

The reliable procedure consists in calling for only one measurement, it does not matter whether of current or voltage because by doing so the load evaluates both variables passing through the system. In a similar way, by fetching only one of them both current and voltage data saved in the buffer can be correctly retrieved. The only constraint is that if current is measured then voltage must be fetched and vice versa.

For this present stage 3 different circuit have been studied for different ranges of frequency:

- Pure resistor with $R=11\Omega$
- RC system in series with $R=11\Omega$ and $C=7\mu F$
- Randles cell with series $R=12\Omega$, parallel $R=100\Omega$ and $C=9\mu F$

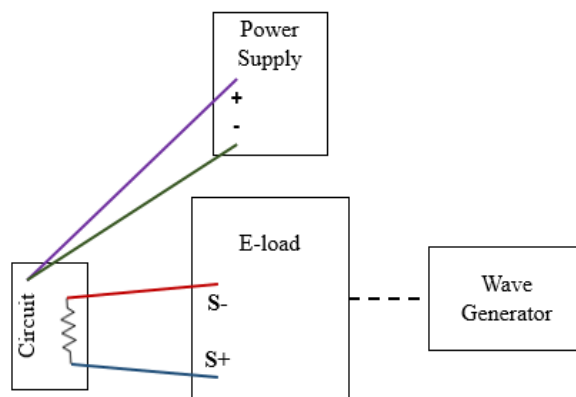


Figure 3.9 Experimental Setup

The setup of the system is represented in figure 3.9. The circuit is welded on a printed circuit board. The extremities of the circuit (in this case depicted as a resistance) are connected to the terminals S+ and S- of the electronic load, while the power supply is achieved through a connection between the board and the DC adapter.

Figures 3.10-12 show how the three aforementioned systems vary with frequency. It can immediately be observed that even if for the most part the results obtained are those expected, some minor deviations from the ideal behavior are present in these real systems.

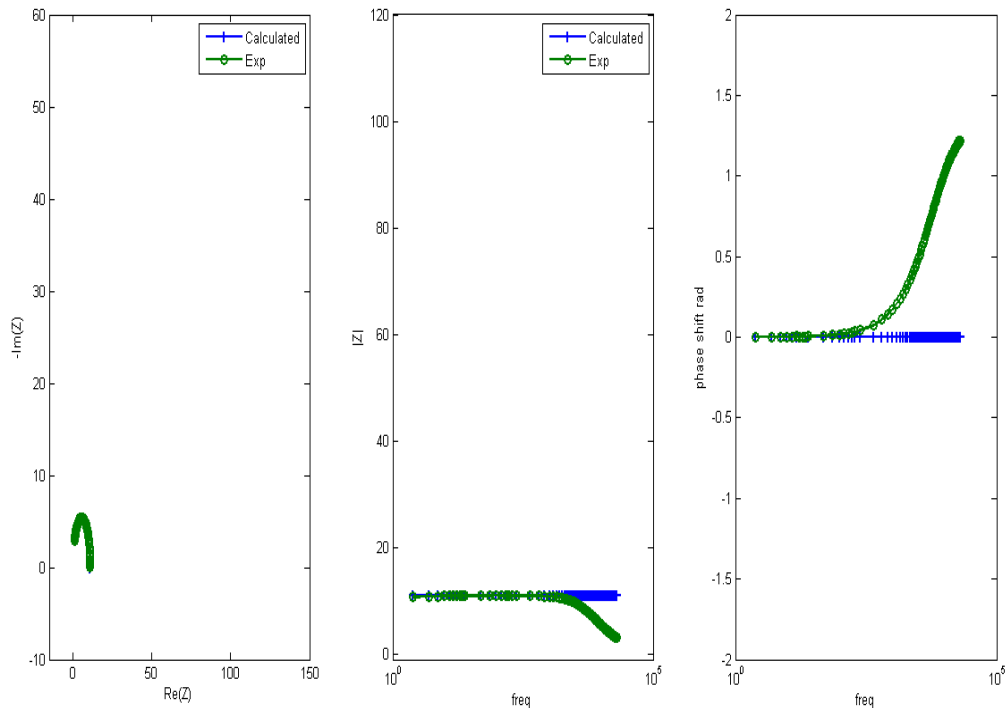


Figure 3.10 Pure resistance up to 20 KHz

The use of real connection elements adds an uncertainty in measurements to the analysis. Now the frequency becomes an important specification while performing EIS, because it cannot exceed a certain value. The majority of EIS manufacturers specify a maximum frequency of 1 MHz.

Some manufacturer's specifications, however, misrepresent true system performance. Many EIS instruments specified to measure impedance at 1 MHz can apply a 1 MHz signal and measure a response, but have huge errors when they do so. Figures 3.13 a and b are example of such behavior. ⁽⁵¹⁾

Besides the deviation from ideality, also some inaccuracies can be observed for some frequencies scanned. These perturbations derive from the way in which frequency has to be implemented.

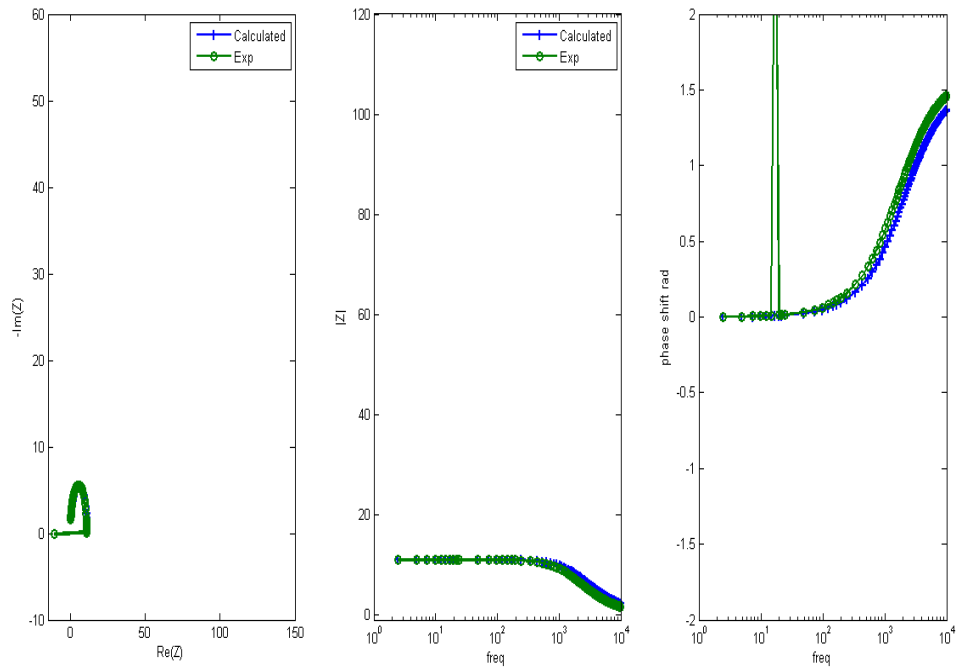


Figure 3.11 RC in series up to 10 KHz

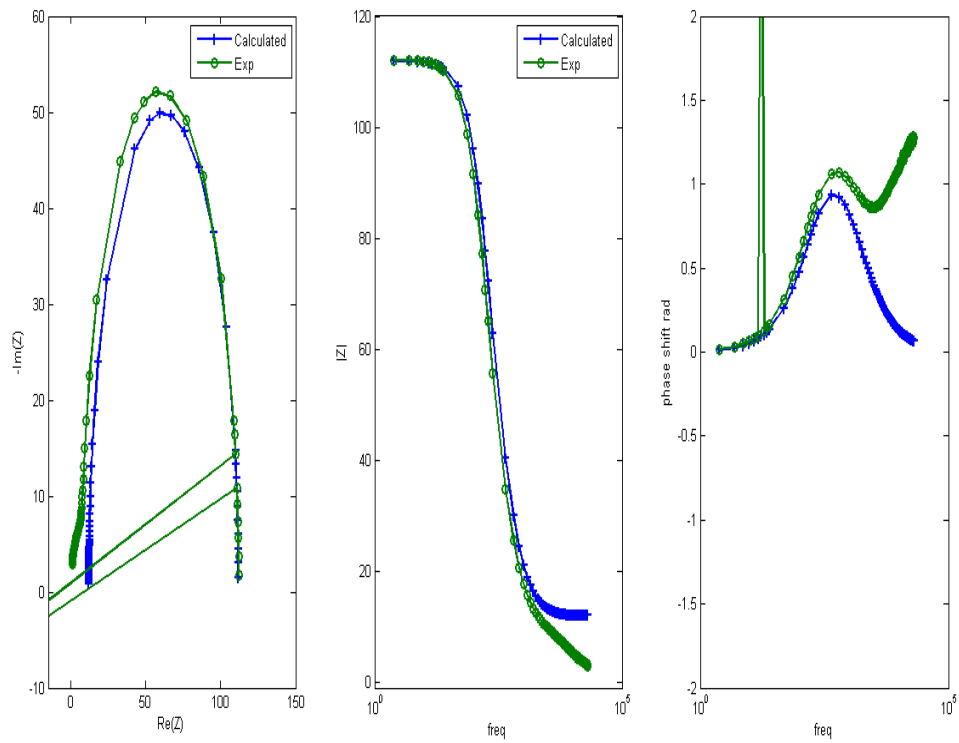


Figure 3.12 Randles circuit up to 20 KHz

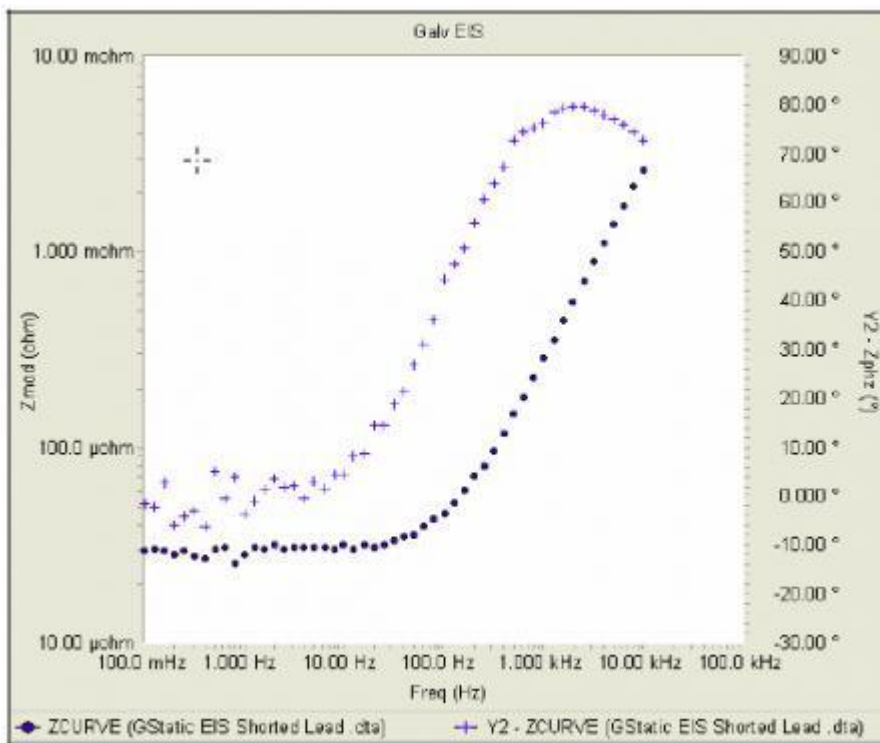
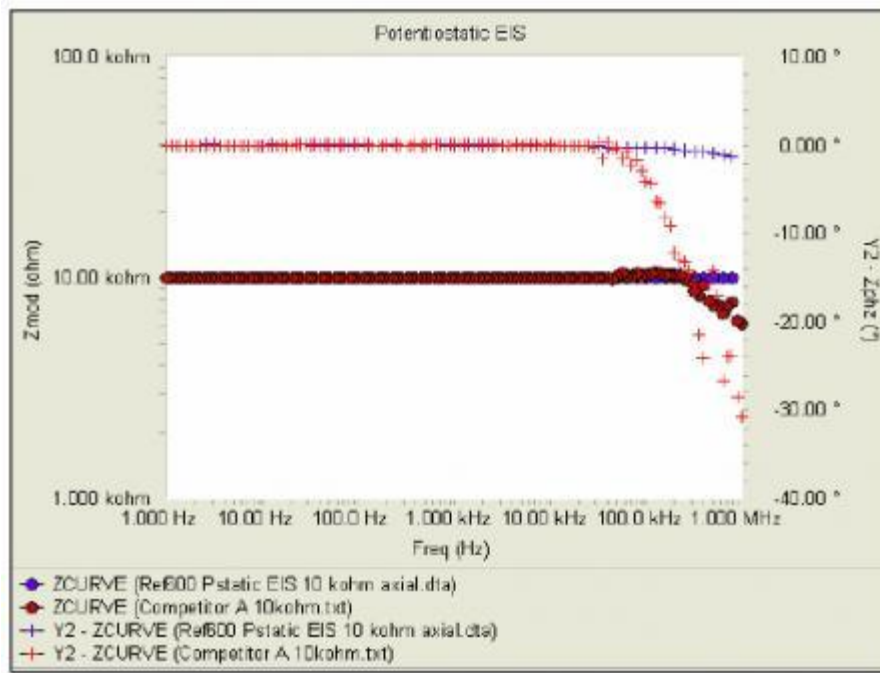


Figure 3.13 Deviation from ideality during measurements

The way in which frequency is defined implies two problems: the first the presence of duplicate frequencies if they are not set in manual mode while the second is independent on how frequencies are defined in the script. As can be seen from figure 2.10 some values are not integer numbers but rather ciphers with several decimals. Even though these

values can be precisely defined in the script, during the scansion the load tends to round to the first decimal, which leads to miscalculations in the FFT. This can be seen in the final result as not coherent points in the plots.

These two inconvenient, however, do not pose as a problem for the EIS analysis since most of the measurements do not exceed 10 kHz, range that this instruments ensures when it comes to accuracy., and the isolated perturbed points can be easily removed without altering the final data distribution.

3.2.2 Analysis on Batteries

The following step included the analysis of elements and the fitting of the results through the EEC theorem. This provided a first opportunity at attempting a study of the results obtained.

Two measurements were carried on alkaline batteries, such as those that are normally used in the bicycles headlights. The characteristic of the battery are the following: Battery Sony, 9V, 6lf22, 6am6. First on a single battery was considered and subsequently two batteries in series.

In this case the setup is similar to that explained in figure 3.9 but without the printed circuit board and the power supply. In this case, there is a direct connection between the battery and the load and the same battery supplies the ΔV required.

With the use of self-supplying elements, the voltage set on the script (which is the same of the previous case) becomes of important because setting a high ΔV might deplete the battery. Since the ΔV given by the battery (or the power supply) corresponds to a certain value of current, it must be ensured that the value of current taken though the load is less than the one available.

Figure 3.14 shows the data obtained for the single battery. It can be observed that the resulting spectroscopy is similar to that of a RC series circuit, where the value of the electrical resistance is 4.7Ω , $C=5.4 \times 10^{-5}$ F. The calculated points (blue line) are obtained through the assignment of an equivalent circuit while the experimental points are those retrieved through the actual EIS measurement.

It must be mentioned that the phase shift plot presents only one set of data, the one relative to the acquired (experimental points). This is due to the fact that the fitting was covered

by the experimental points and consequently it was removed. Nevertheless, if compared to the previously described RC circuit, the plot obtained is coherent to the fitting selected. Unfortunately, it was not possible to determine whether the lack of experimental points corresponding to the uncovered blue line were caused by a non-efficient fitting or to the connection between load and battery.

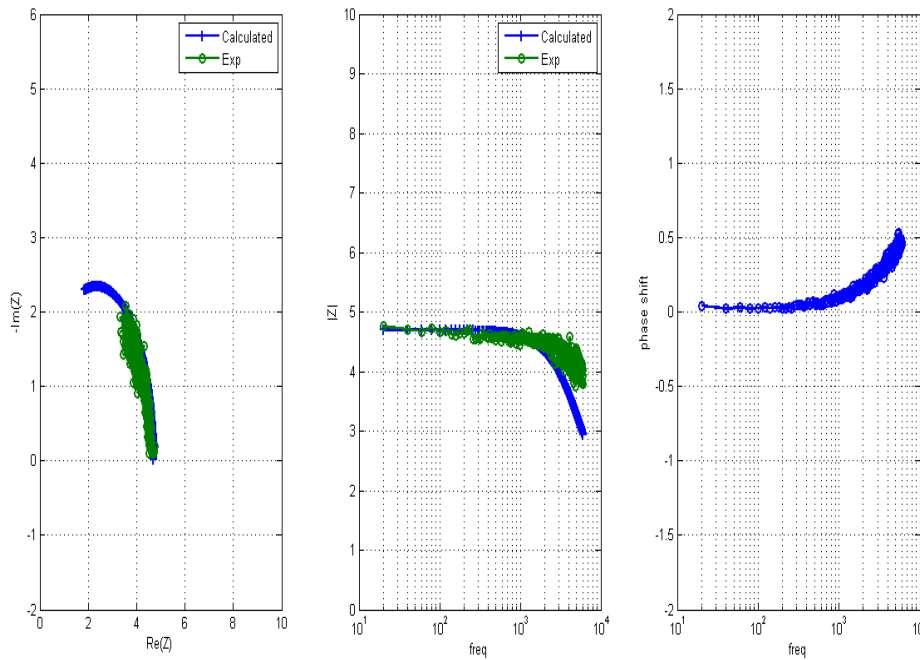


Figure 3.14 Single Alkaline Battery

Subsequently two batteries in series (with the same characteristics as before) were analyzed giving the following data.

The results obtained are of difficult interpretation since Bode and Nyquist plot do not seem to correspond. Even though that in this case we continue to obtain something similar to a RC series circuit, a proper fitting for the Bode plot gives inaccurate results for the Nyquist plot- something similar to what happens to the inductor plots generated through a synthetic wave (figure 3.3).

However, it is possible that a more complicated equivalent circuit can provide a better fitting since the choice of the EEC is not univocal.

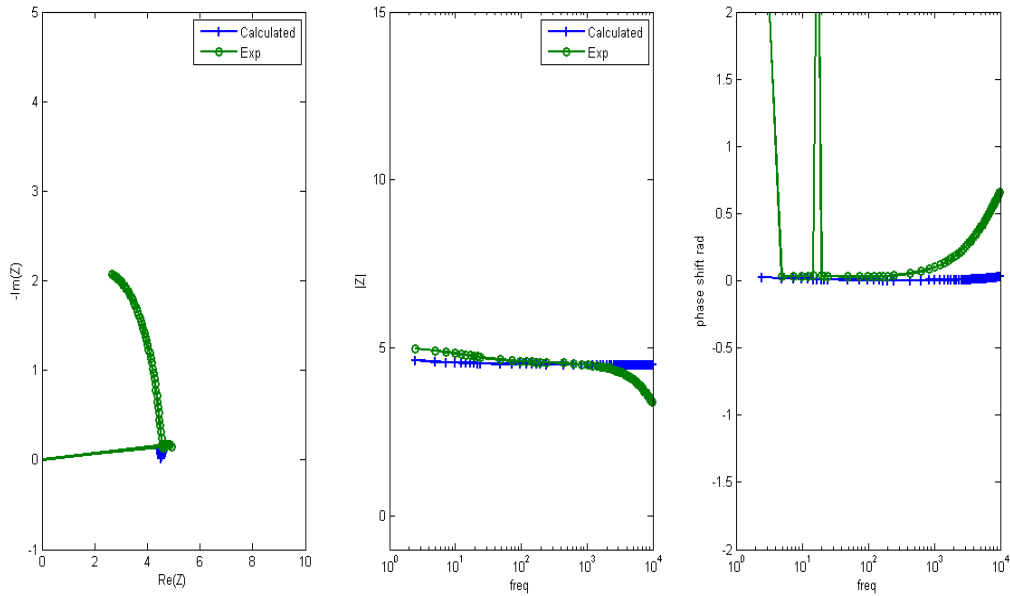


Figure 3.15 Alkaline Batteries in series

3.2.3 EIS analysis of SOFC with novel materials

3.2.3.1 Analysis Method: Selection of the EEC

As discussed in chapter 2, interpretation of impedance measurements is often done by using the electrical equivalent circuit theorem. It must be noticed, however, that electrical equivalent circuits are not univocal and that more than one configuration can produce fittings of similar quality and accuracy. Thus, the choice of the EEC depends heavily on who is carrying out the measurements instead of the nature of the material by itself, even though it is common to rely on systems used for tests done on the same materials.

For this particular case, it was chosen to use a version of the Randles circuit which includes a Warburg element, such as the one shown below in figure 3.16.

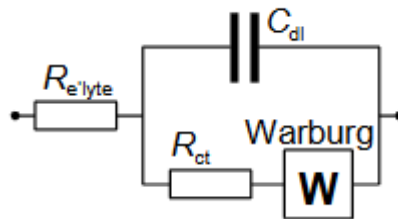


Figure 3.16 Randles circuit

The selection of this disposition was based on the vast knowledge of the meaning of each single element composing the system. Where R_i is the ionic resistance of the electrolyte, C_{dl} is the double layer capacitance and R_{ct} is the charge transfer resistance. The semi-infinite diffusion is represented by the Warburg (W) element.

More often than not the capacitance element is substituted by a constant phase element (CPE). It is encountered frequently in solid state electrochemistry; however, no general physical interpretation has been given yet. The CPE behavior of interfaces has been ascribed to a fractal nature (special geometry of the roughness) of the interface. As for bulk effects no direct derivation has been given. ⁽⁵³⁾

The advantage of using a CPE instead of a capacitance derives from the fact that it adds an extra parameter that accounts for the non-ideal behavior of the circuit elements. By assigning some specific values to this parameter it is still possible to describe ideal situations.

The sense behind these components has roots in electrochemical and quantum considerations.

The presence of a capacitance is owed to the spilling and smoothing effect that takes place in the crystallographic structure (the first one inside the structure while the second one occurs on the surface). Quantum mechanics demonstrate that even if electrons should remain within the potential zone allowed to them, they can momentarily escape this zone and move towards a prohibited potential zone. By doing this the form instantaneous dipoles that imbalance the charge neutrality of the system.

Consequently, electrons have a variable disposition in space that changes continuously. For long periods of time it has been proven that the mean of this distribution is different from zero. The set of instantaneous dipoles present on the surface can thus be seen as a layer of dipoles that have a fixed charge in time.

Because of these phenomena, between an internal point of an ionic conductor and an internal point of an electronic conductor a differential of potential is established (also known as Galvani's potential). This situation is the one encountered while analyzing MIEC materials, such as the ones that will be shortly introduced.

To accurately describe what happens at the interface between both conductors, some models have been developed using the equilibrium condition as the foundation

The simplest of these models is the Helmholtz model. It says that the charge on the surface of the electronic conductor is equal but with different sign to that of the ionic conductor. The interface becomes in practice a parallel plate capacitor. Since a double electronic layer is formed between the two interface the capacitance is aptly named double layer.

Nevertheless, the Helmholtz model is not capable of accounting for some other occurrences that also take place. In order to explain them, the Gouy-Chapman model is used because it considers the effect of the contribution of the thermic agitation.

Thus a diffusive double layer (that can be explained using Poisson's equation and Boltzmann distribution) is introduced into the model. A diffusive effect is hence introduced to the circuital system under the name of Warburg.

The presence of the resistances within the Randles circuit are of different origin. Efficiency of a FC depends essentially on three parameters:

1. Reactants efficiency: not all the fuel sent into the cell is consumed.
2. Gibbs efficiency: not all of the chemical energy (ΔH) can be converted into electrical energy, only ΔG can. Temperature becomes an important parameter since it is directly correlated to the Gibbs efficiency. ΔG becomes less negative with the increase of temperature.
3. Potential efficiency: It is the ratio between the potential supplied by the FC while it is working and the maximum potential it could theoretically dispense (ΔE_{rev}).

This difference between ΔE_{rev} and ΔE_{real} is consequence of what is commonly known as the cell internal resistances. The total resistance can be defines as $R_{tot}=R_0+R(j)$.

The loss of efficiency depends only on the current density with which the cell must work. Therefore, there is a need to render this current density as low as possible.

R_0 is nothing but the sum of all ohmic resistances present in the system and which in this case are given to some degree by the materials and the electrodes while the major part is due to the ionic conductor. In order to reduce the ionic conductor resistance its thickness must be reduced accordingly to Ohm's second law. However, there are also all

the resistances that depend on current density which are namely the overvoltage which are varied in nature.

If ohmic resistances, especially that of the ionic conductor, are prevalent over those deriving from current density, the contribution deriving from overvoltage can be neglected. Such is the case of batteries.

Yet, for FC the resistance cause by the overvoltage of electron transfer becomes comparable to that of the ohmic resistances. In order to quantify this overvoltage Tafel equation ($\eta = a + b \ln |j|$) is commonly used since the situation encountered is one sufficiently distant from the equilibrium.

The most important parameters within Tafel equations are parameter B that depends on a parameter α and the current density (which also depends on α , if defined according to the Butler-Vollmer- see chapter 1). So, it can be observed that overvoltage grows if the current density exchanged is diminished.

Electron transfer can be seen as a reaction kinetic and therefore it has an Arrhenius dependence on temperature. This means that the higher the temperature the lower the resistances.⁽¹⁾

Since the Randles cell contains all the elements mentioned above, it can be seen why it usually proves to be a good fitting model for EIS spectra.

Once understood the physical meaning of each circuit component, it is appropriate to closely inspect the elements that compose the Nyquist plot and how the values of the parameters included in the Randles circuit affect the curve.

Figure 3.17 a-d shows a generic Nyquist plot. Each image contains the same plot but it highlights one section of the plot with a different color.

In the first figure a green circle can be seen at the most left side point of the curve as well as a green line whose extremities were named a and b. The value of that coincided with the green circle is not other than the value of the electrolyte resistance while the distance between points a and b is the value assigned to the charge transfer resistance. A decrease in R_{ct} not only narrows the base of the bell but all diminishes the height of it.

In the second picture the highlighted red zone corresponds to the right slope of the Nyquist plot. This side corresponds is tightly linked to the value assigned to the capacitance in parallel. In absence of diffusion the value of the capacitance is not entirely important since it slightly changes the slope of this curve. This, however, is not the most common situation encountered in practice. In the presence of diffusive processes an increase in capacitance stands for a shortening in the red line while decreasing its values does exactly the opposite- it lengthens it.

Figure 3.17.c represents the effect of the Warburg element. The yellow line is representative of the diffusive processes inside the system and the longer it is, the more important diffusion becomes. In the case $W=0$ the plot does not show this line but simply continues toward the abscissa.

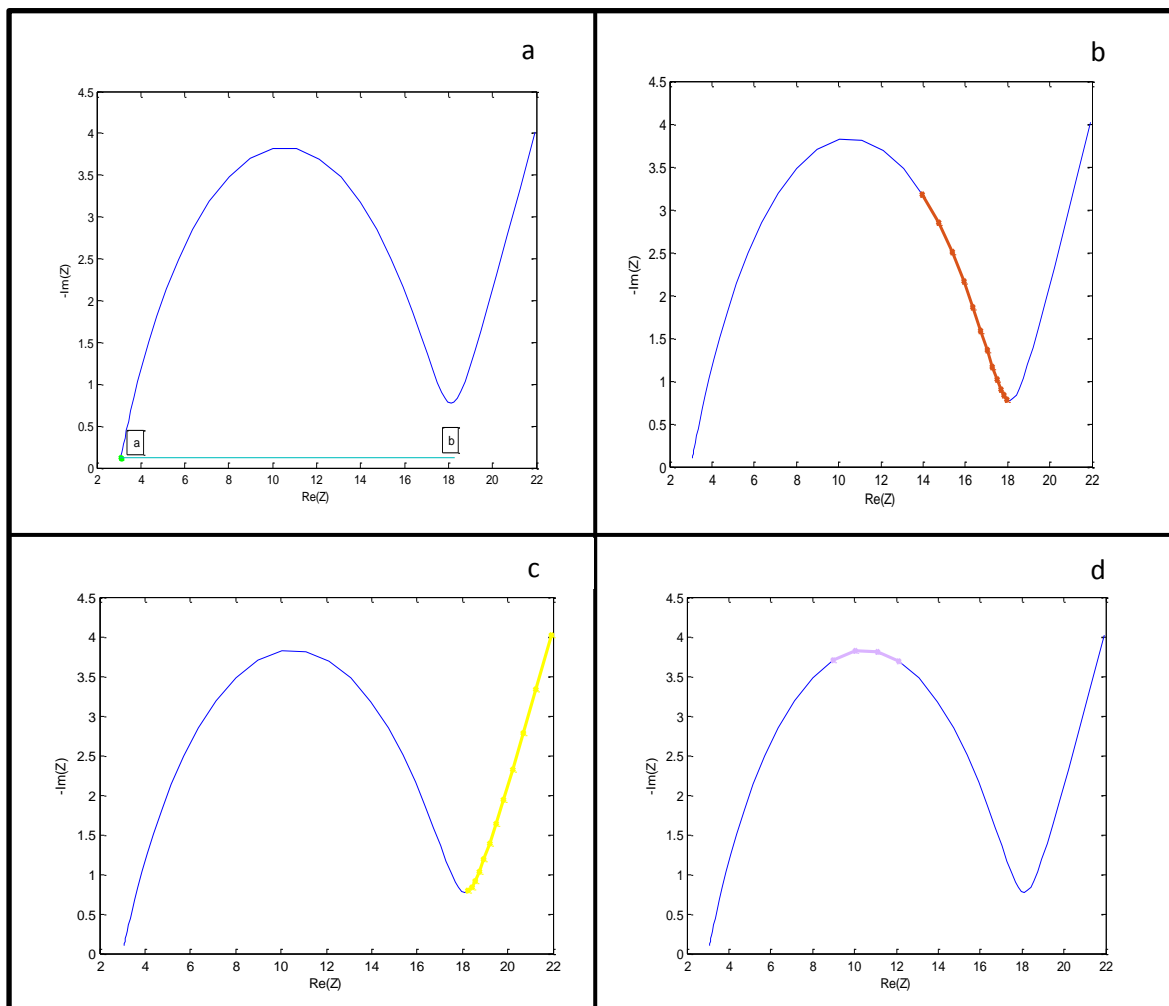


Figure 2.17 Sections of a Nyquist plot

Lastly, figure 3.17.d stand for the variations of the a parameter found in the CPE. Usually values smaller than 0.5 are not used because they represent a non-ideality in the resistive behavior which is not physically possible. On the other hand, values $1 < a < 0.5$ account for the non-idealities in the capacitive behavior which is something that can occur in real systems. Even though this parameter has no physical meaning it was observed that by adjusting it the height and the narrowness of the top of the bell (lavender line) can be modified.

Independently of the circuital meaning that can be given to the curves, which as stated before can be ambiguous due to the different EECs that can fit one spectroscopy, it is undoubtable that low frequency behaviors are related to mass transport phenomena while high frequency is related to electrochemical reactions.

This leads to an alternative approach to EIS (not considered in this study work) which tries to decouple the different phenomena taking place inside the ceramic. By using physical equations (i.e. Navier-Stokes) and inserting as many known parameters as possible it is possible to retrieve the values of all missing parameters. This approach foresees simulation and not only can it characterize the material in the way proposed here but can also give information concerning the limitations that need to be overcome.

Now that the fitted elements have been explained it is possible to compare the characteristics between samples in order to determine whether improvements have been made by altering the synthesis process.

While analyzing Nyquist plot, different types of arches can be found depending on the different phenomena that can be had in the system. The arch encountered in this system has been associated to electrochemical reactions

3.2.3.2 Materials and Data Acquisition

Due to different factors it was not possible to carry out measurements on fuel cell ceramic materials described above. However, fitting of impedance spectra was feasible by using data rendered available by the Faculty of Chemical Sciences of the University of Padua.

(52)

Evaluation if this data is useful since the same materials will be eventually tested under the same conditions while using the e-load. By comparing existing data to that which is expected from these measurements, a second verification of the system is obtainable.

Five different samples were assessed, all of them symmetric cells on GCO electrolyte but synthesized at different temperature or having different composition. For simplification, all samples have been renamed in the way explained in table 3.1.

Table 3.1 Composition of the single samples

Name	Composition	Synthetization Temperature
A	$\text{La}_{0.6}\text{Sr}_{0.4}\text{Ga}_{0.3}\text{Fe}_{0.7}\text{O}_3$	1000°C
B	$\text{La}_{0.6}\text{Sr}_{0.4}\text{Ga}_{0.3}\text{Fe}_{0.7}\text{O}_3$	1100°C
C	$\text{La}_{0.6}\text{Sr}_{0.4}\text{Ga}_{0.3}\text{Fe}_{0.7}\text{O}_3+\text{MnOx}$	1000°C
D	$\text{La}_{0.6}\text{Sr}_{0.4}\text{Ga}_{0.3}\text{Fe}_{0.7}\text{O}_3+\text{MnOx}$	1100°C
E	$\text{La}_{0.6}\text{Sr}_{0.4}\text{Ga}_{0.3}\text{Fe}_{0.7}\text{O}_3+\text{FeOx}$	1000°C

(La, Sr)(Fe, Ga)O₃ perovskite, also known as LSGF, is a MIEC perovskite with great chemical and thermal stability. Even though it shows slightly lower performances with respect to the most common materials - manganese and cobalt based perovskites- the chemical stability improves with respect to these materials while still allowing a good oxygen semi-permeation.

The composition exhibiting the best compromise between activity and stability, has been identified in $\text{La}_{0.6}\text{Sr}_{0.4}\text{Ga}_{0.3}\text{Fe}_{0.7}\text{O}_3$, hence this is the only composition considered.⁽⁵²⁾

Figure 3.18 shows how the Nyquist plot for sample A varies for different temperatures. One of the first things that can be observed is that for low temperatures (<545°C) a 45° angle line appears at the end of the arches. This line is typical of diffusive processes and it's not surprising to see it since at these temperatures diffusion is still a limiting step with respect to the reactions taking place inside the FC.

As it can be expected, temperature improves kinetics. For this reason, a shrinkage of the arches can be seen as temperatures go up.

Figure 3.19 shows the same plot but for a material that was synthesized at 1100°C instead of 1000°C.

The first difference that can be seen between the two figures is that synthesis at higher temperatures allows for a diminution of diffusive processes inside the material.

Still, sample B shows a small loop at high frequencies which is a behavior not yet explained (and not expected) for this type of plots. This is nothing but an inductive behavior which appears in the high frequency range and that is easily explained by instrumental artifacts, inductance of the electrode, or the inductance of the connecting wires. For this reason, it is usually not considered in the fitting of the data.

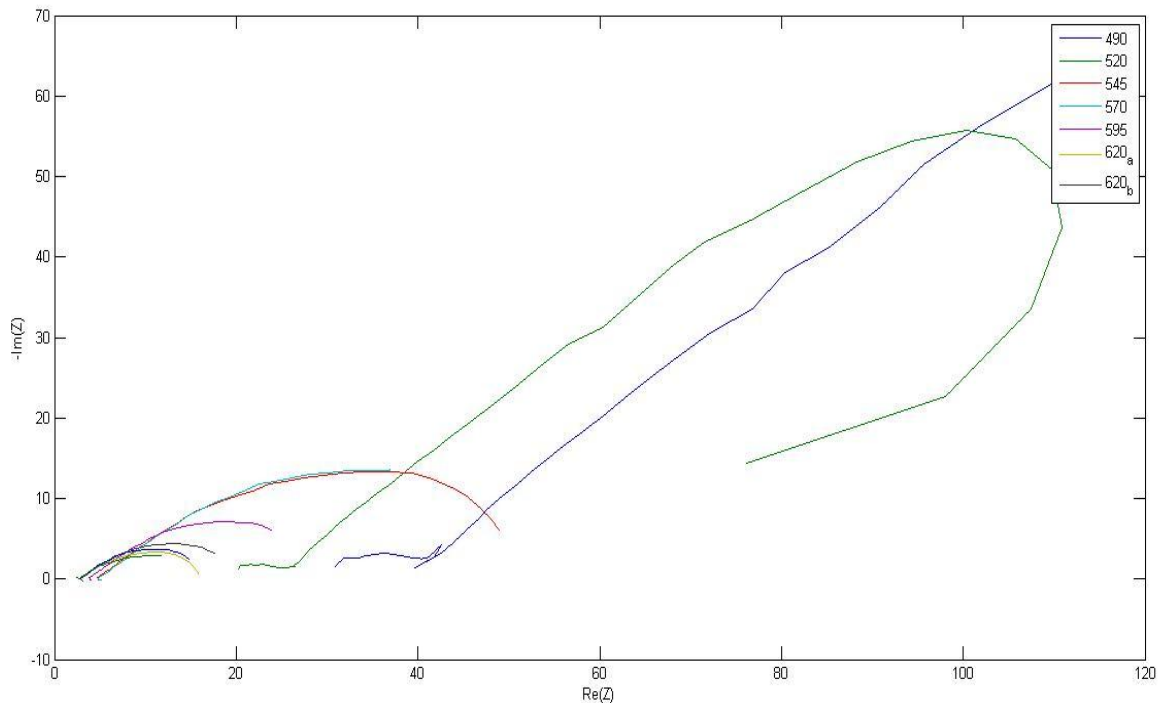


Figure 3.18 Nyquist plot – parametric in T- for sample A

Figure 3.20 represents a different material with respect to the previous cases since manganese oxide is now coating the surface of the ceramic material. The presence of MnOx increases the dimension of the arches, which already suggests a worsening in the overall behavior. The same compound synthesized at higher temperature- figure 3.21- does not show improvements with respect to the non-coated material but only with respect to its lower T synthesized version

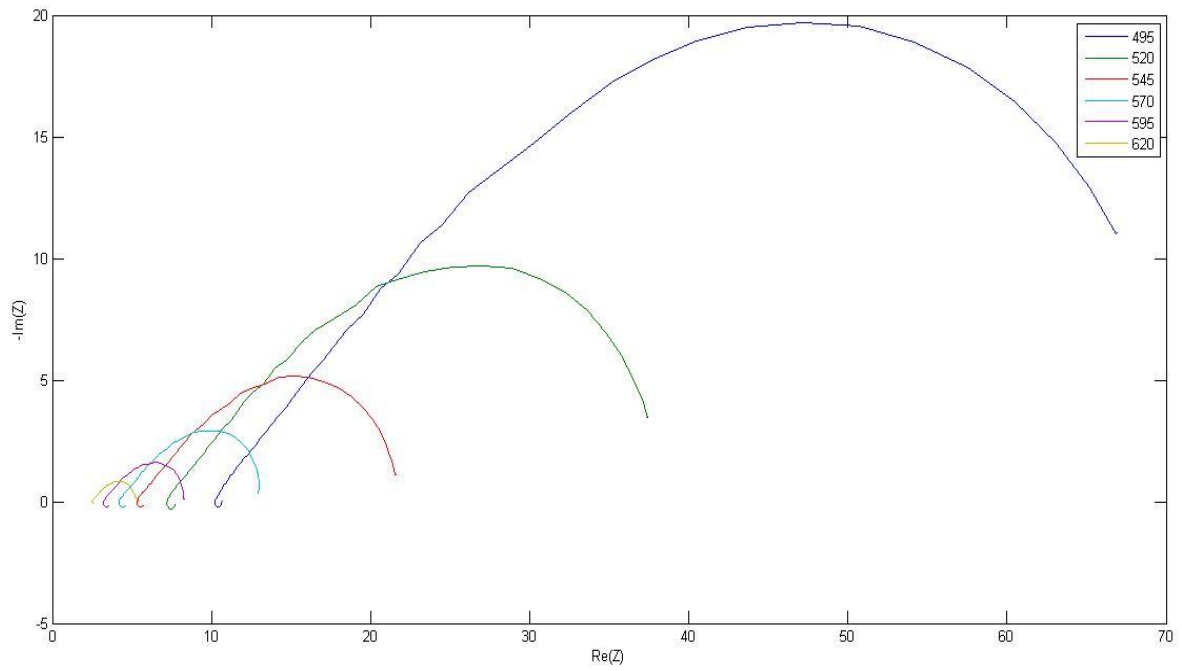


Figure 3.19 Nyquist plot – parametric in T- for sample B

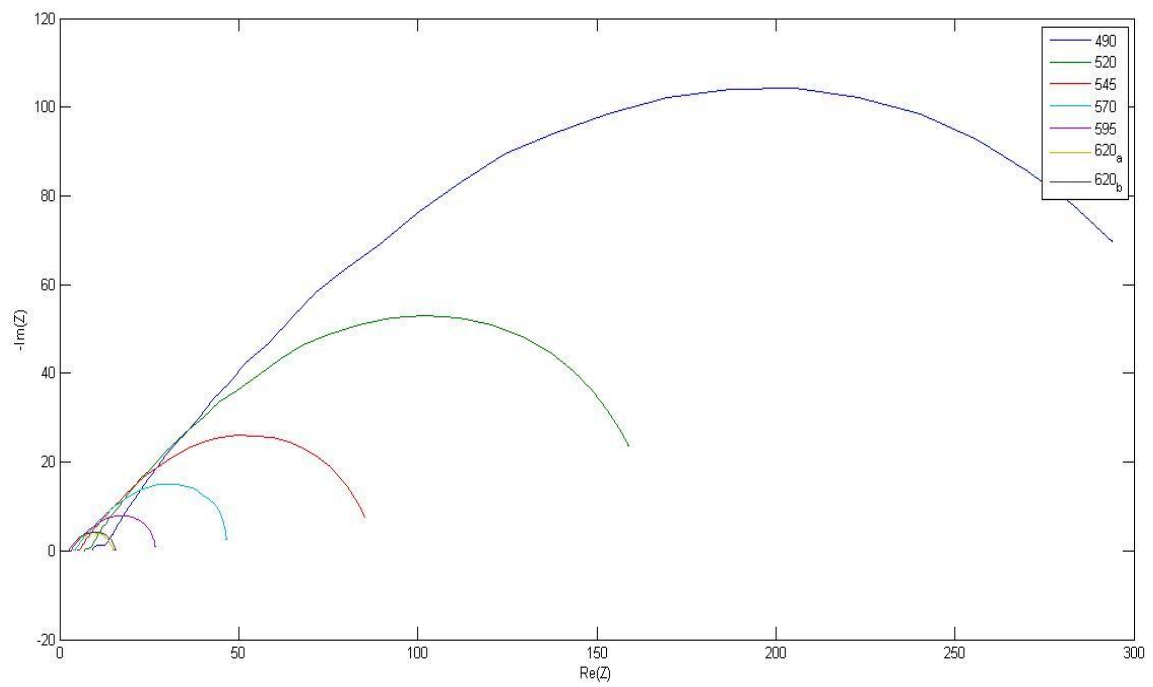


Figure 3.20 Nyquist plot – parametric in T- for sample C

Sample E consist of the same material synthetized at 1000°C but coated with ferrous oxide instead of manganese. While in the precedent case the coating implied a worse performance, now it means an overall improvement. Consequently, this set-up allows for a better performance with respect to all former samples.

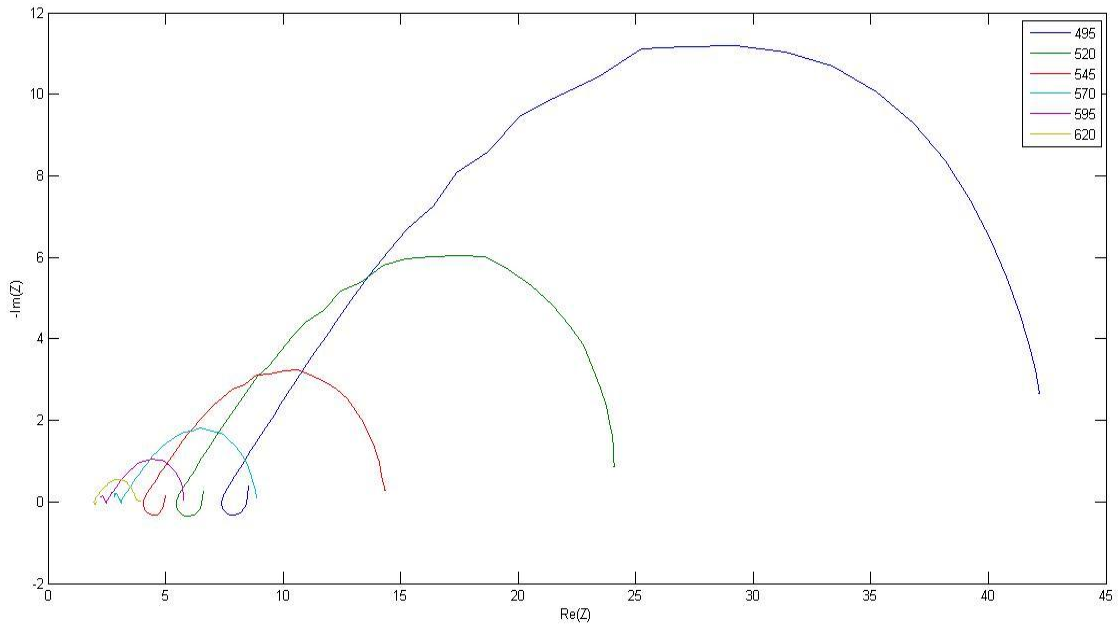


Figure 3.21 Nyquist plot – parametric in T- for sample D

The FeOx coated material shows two features, one of them already seen in sample B while the second is something not seen before, that are worth mentioning. For the lower temperatures, an inductive behavior can be perceived in the form of a closing loop at the left extremity of the curve.

Yet, as temperatures increase this inductive behavior seems to become the beginning of a second arch, which suggests that now not only one phenomenon is taking place inside the material. Usually these two arches can either be explained through a failed coating model or when systems have two time constants. Given the nature of the material being analyzed, the first option seems a the more sensible option.

One common characteristic that is not to be underestimated is the presence of the Warburg element in all fitting. Even though only sample A at low temperatures shows a distinct

diffusion component, all other samples contain a small diffusion contribute that cannot graphically be seen.

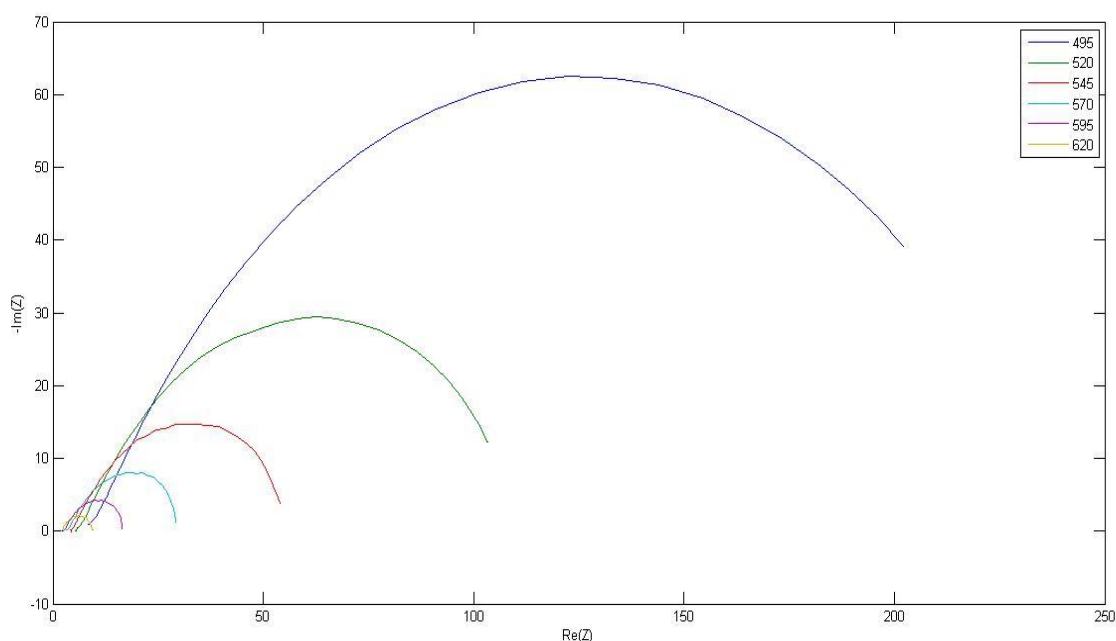


Figure 3.22 Nyquist plot – parametric in T- for sample E

Real processes are not exempt from this type of transport. It may be less relevant when compared to convection or irradiation but it is still always present. Without the Warburg element diffusion is not accounted for and hence the arch closes itself by reaching the x-axis instead of allowing the right-sided line to stop midway.

3.2.3.3 Data Interpretation

The figures considered so far represent only experimental data but without taking into account the values of the fitted parameters and how accurate they are when compared to the original curves. Also, they were commented without going into detail about the phenomena taking place inside the material and how this improves/worsens the characteristics that are searched for.

However, even without a fitting, it is possible to already form an idea on the performance of the samples previously discussed by comparing the EIS curves at similar temperatures. Even though the minimum analysis temperature does not yield the best result due to higher charge transfer resistance and a more noticeable limitation of the double layer capacitance (also related to mass transport), a trend on the behavior of all five samples can be already determined.

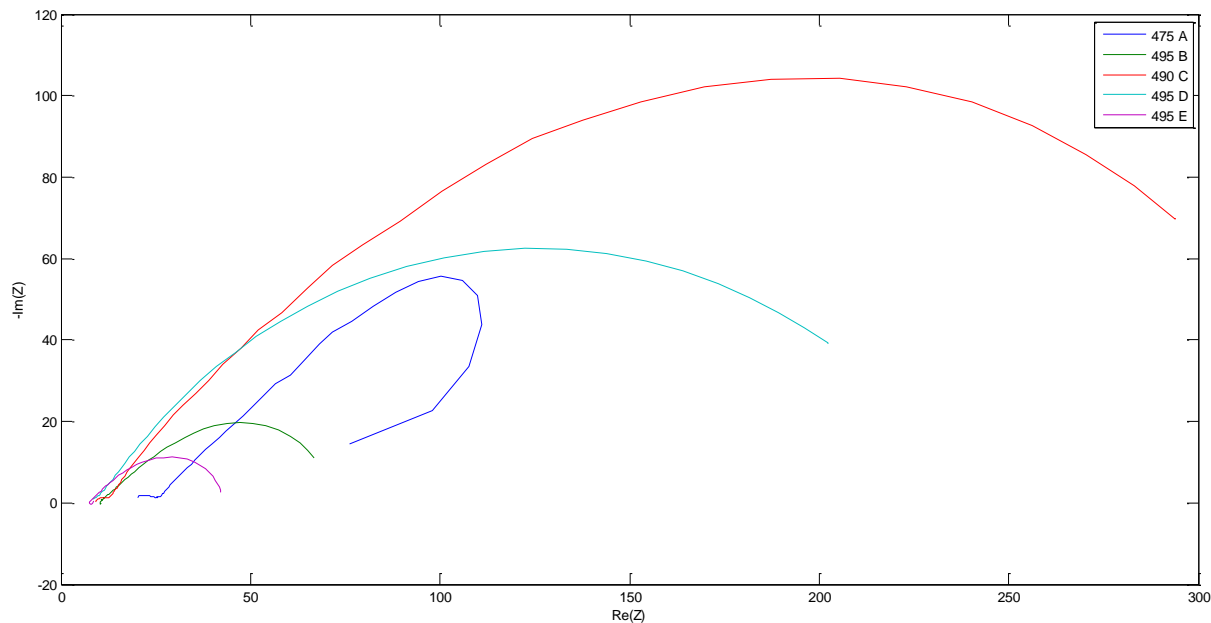


Figure 3.23 Nyquist plot for samples at low temperature

From figure 3.23 some considerations can be made that are of general validity. First, analyses made at temperatures well below the 500°C, such as sample A, demonstrate a penalization in diffusive transport that is not desired at all. Consequently, temperature becomes a limit of great importance and this is why new materials need to overcome it in order to be rendered more desirable.

Second, the synthetization temperature plays a fundamental role in behavior improvement for a given material. As can be seen from samples A and B or C and D, a raise of only 100°C in synthetization can diminishes by circa one third the resistances connected to passage of current through the system.

This is desirable since it is easier to improve this type of resistance instead than to lower the intrinsic resistance of the material, which is a property that cannot be changed without changing material.

A third general consideration regards the effect of the double layer capacitance. While looking at Nyquist plots, the left side data can be associated to high frequencies, this means the reactions taking place. Likewise, right sided data is linked to low frequencies and mass transport phenomena which can be divided into two main groups the matter in consideration: convection and diffusion.

From a circuitual point of view, it has already been said that diffusion can be expressed through the Warburg element. Yet convection, which has a greater importance when it comes to mass transfer since it can hinder in a more perceptible way the reactions taking place, has not been commented explicitly.

In fact, the effect of the capacitance within the circuit is exactly this one. Systems with higher capacitance show a greater distance between the real axis and the more right-sided point, which means that also mass transfer needs to be improved in order to also diminish the resistances within the system. This is exactly the case of sample C and D.

It must be said, however, that both diffusion and convection are highly dependent on temperature. For this reason, it is expected to obtain a better behavior while raising the temperature.

The presence of a coating in the material can either improve or worsen the behavior depending on what is used. Samples C and D use a manganese oxide coating and they show worse characteristics with respect to their non-coated counterpart. Yet, the use of ferrous oxide cause the opposite to take place: an improvement is achieved. For this reason, no general considerations can be made in this respect.

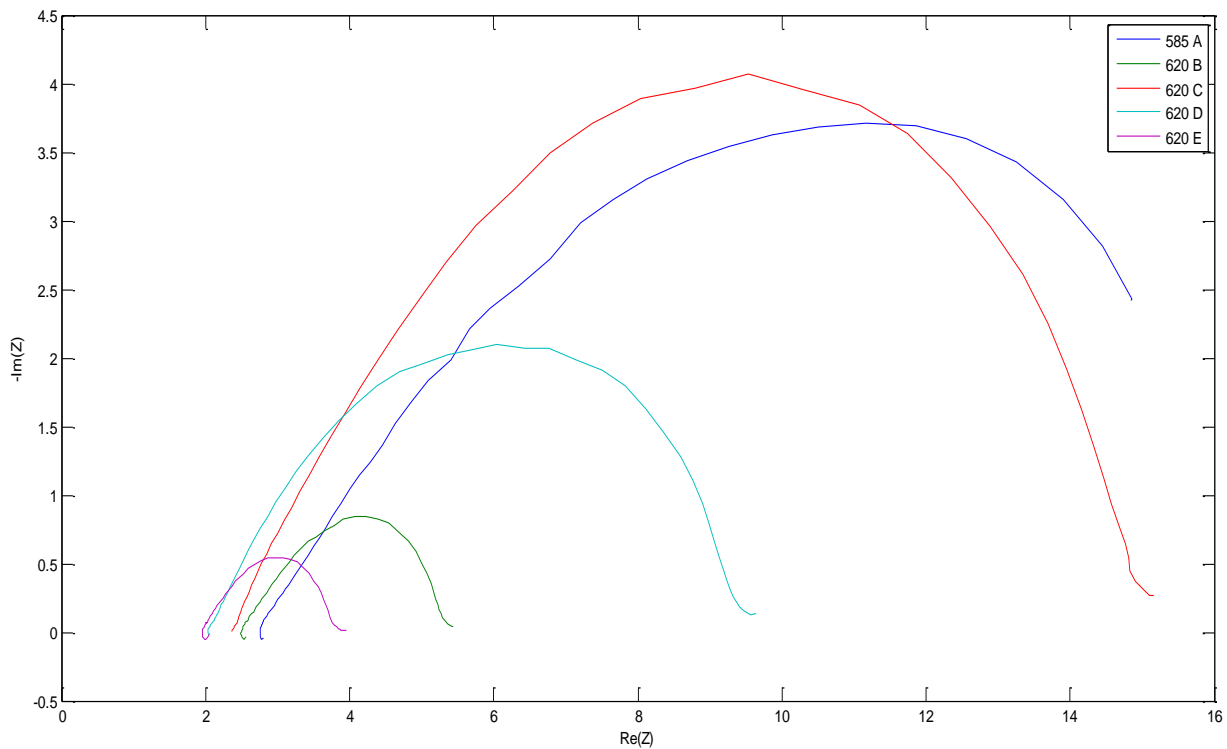


Figure 3.24 Nyquist plot for samples at high temperature

Figure 3.24 shows the same five samples, this time all at the highest analysis measurement available. It can be observed that all considerations made so far still apply, which confirms the trend proposed before. Consequently, even without fitting, sample E can be foreseen as the best one among the ones studied.

In order to confirm this hypothesis, as well as the one regarding the choice of the EEC, a fitting has been carried out using the program Impedenza (explained in a previous section) coupled to the program Model. Both script can be found in Appendix A.

Due to the quantity of curves to be fitted, fitting will be presented in groups, each one relative to one sample. At the end a table containing all parameters for a given sample will be presented along some comments relative to the fitting. The first group of fitting, presented through images 3.25 a-i, is sample A.

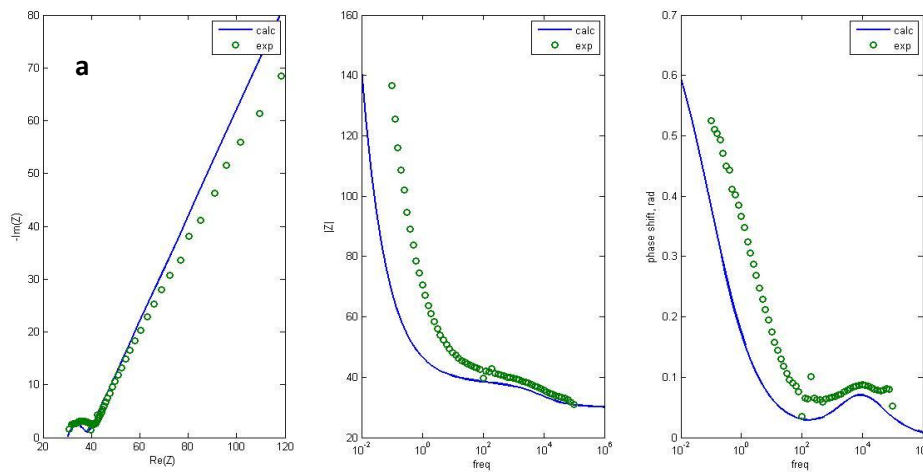


Figure 3.25.a $La_{0.6}Sr_{0.4}Ga_{0.3}Fe_{0.7}O_3$ - synthesized @1000°C- 430°C

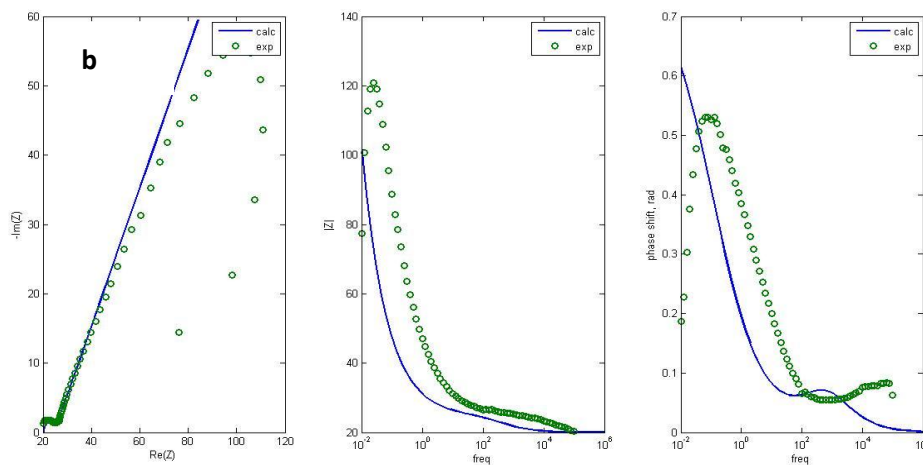


Figure 3.25.b $La_{0.6}Sr_{0.4}Ga_{0.3}Fe_{0.7}O_3$ - synthesized @1000°C- 475°C

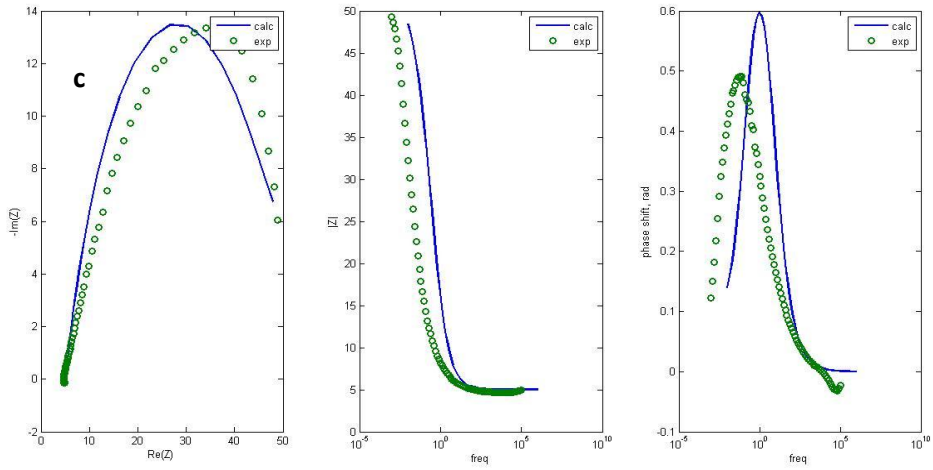


Figure 3.25.c La_{0.6}Sr_{0.4}Ga_{0.3}Fe_{0.7}O₃ - synthesized @1000°C- 535°C (1)

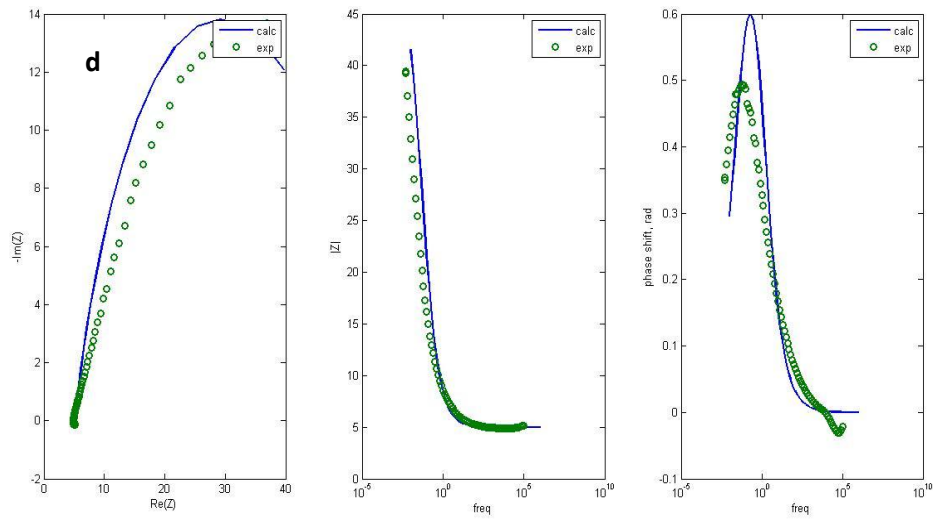


Figure 3.25.d La_{0.6}Sr_{0.4}Ga_{0.3}Fe_{0.7}O₃ - synthesized @1000°C- 535°C (2)

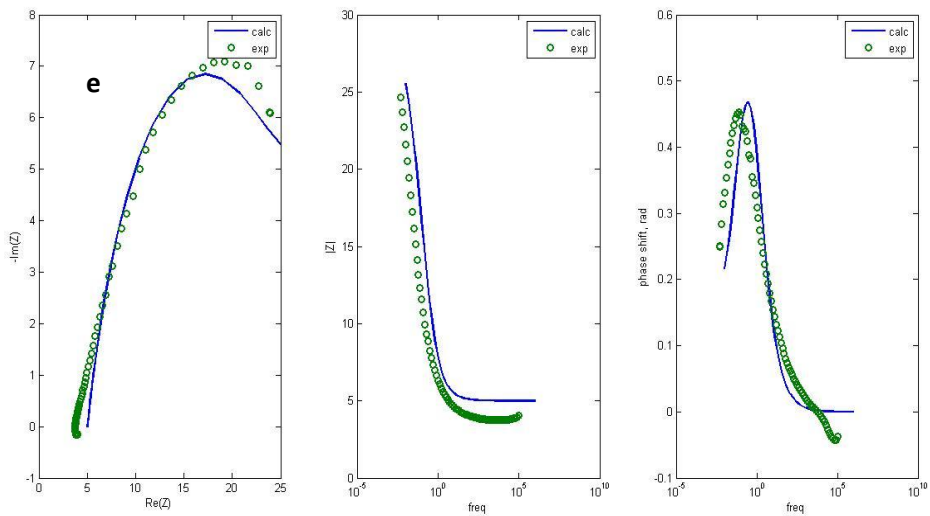


Figure 3.25.e La_{0.6}Sr_{0.4}Ga_{0.3}Fe_{0.7}O₃ - synthesized @1000°C- 560°C

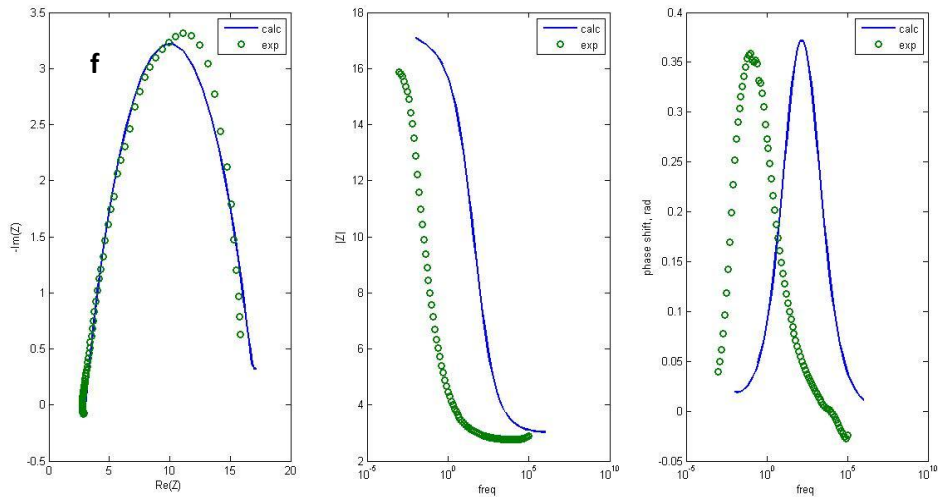


Figure 3.25.f La_{0.6}Sr_{0.4}Ga_{0.3}Fe_{0.7}O₃ - synthesized @ 1000°C- 585°C (1)

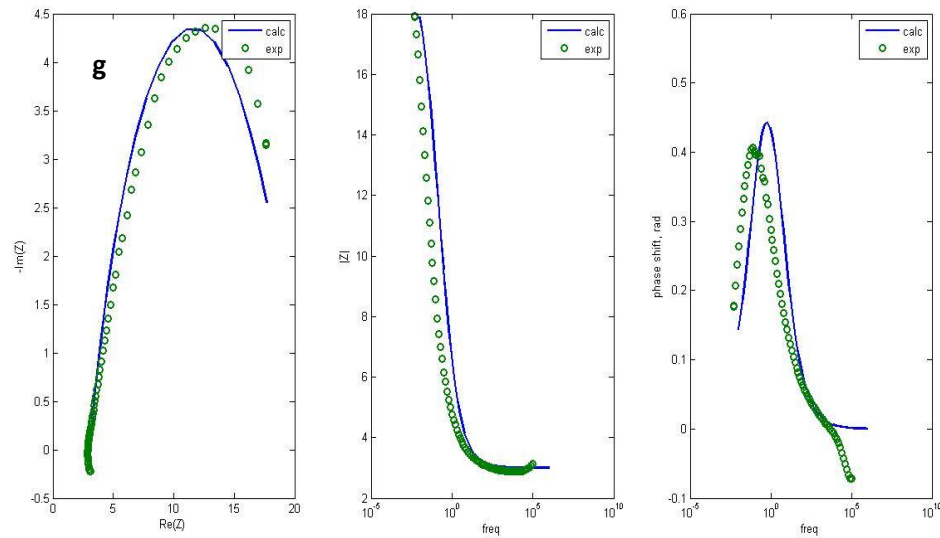


Figure 3.25.g La_{0.6}Sr_{0.4}Ga_{0.3}Fe_{0.7}O₃ - synthesized @ 1000°C- 585°C (2)

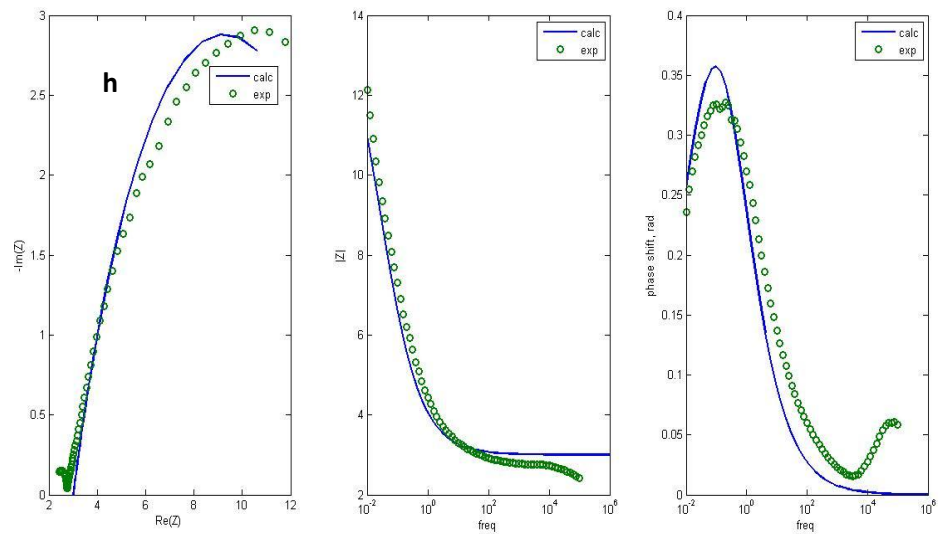


Figure 3.25.h La_{0.6}Sr_{0.4}Ga_{0.3}Fe_{0.7}O₃ - synthesized @ 1000°C- 585°C (3)

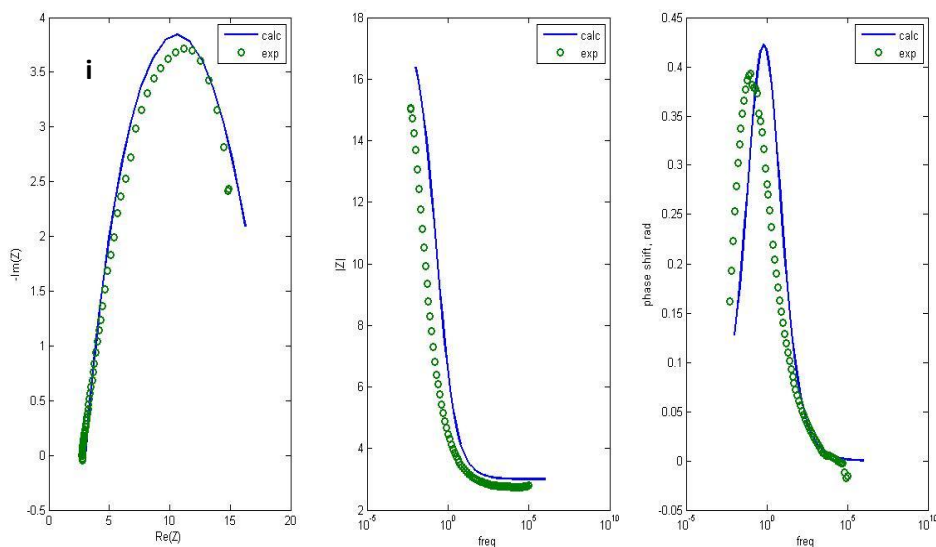


Figure 3.25.i La_{0.6}Sr_{0.4}Ga_{0.3}Fe_{0.7}O₃ - synthesized @1000°C- 585°C (4)

Table 3.2 Parameters for sample A

La _{0.6} Sr _{0.4} Ga _{0.3} Fe _{0.7} O ₃ – synthesized @ 1000°C					
T(°C)	R1(Ω)	R2(Ω)	C(F)	a	W(Ωs ^{-1/2})
430	30	8	8,00E-05	0,68	20
475	20	5	8,00E-04	0,68	15
535_1	5	45	2,00E-02	0,68	0,5
535_2	5	45	6,00E-02	0,68	0,5
560	5	22	7,00E-02	0,68	0,5
585_1	3	14	4,00E-03	0,55	0,05
585_2	3	20	7,00E-02	0,6	0,05
585_3	3	12	2,50E-01	0,56	0,05
585_4	3	15	7,00E-02	0,6	0,05

Since the same EEC was used for all samples studied, it is not surprising that it may adapt better to some cases with respect to others. In figure 3.25.f it can be seen that even if the impedance Bode plot seems accurate enough, the calculated phase shift Bode plot and the calculated Nyquist plot (obtained through fitting) diverge slightly from the experimental points.

Figure 3.25.e shows on the other hand that in some cases the fitting is basically perfect while figures such as 3.25.a demonstrate a slight less ideal fitting, yet good enough

considering the circuit chosen. Similar behavior will be encountered in the following figures.

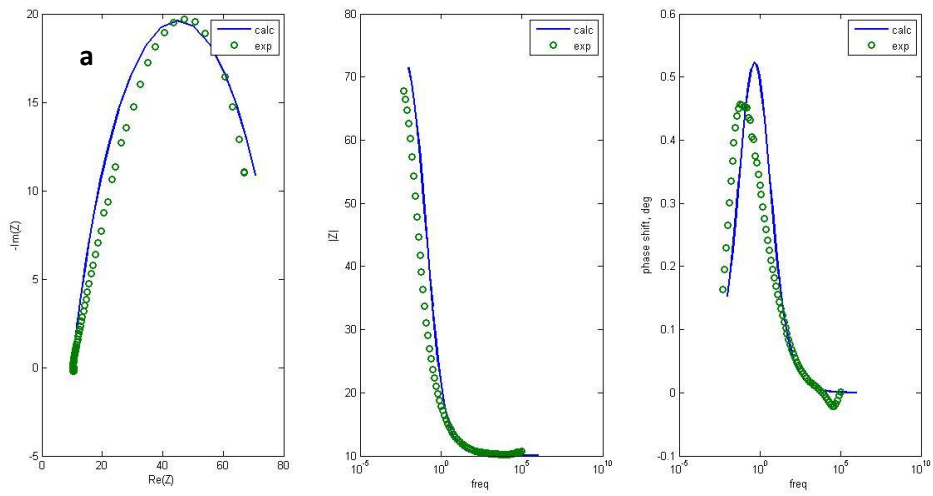


Figure 3.26.a $\text{La}_{0.6}\text{Sr}_{0.4}\text{Ga}_{0.3}\text{Fe}_{0.7}\text{O}_3$ - synthesized @ $1100^\circ\text{C}-495^\circ\text{C}$

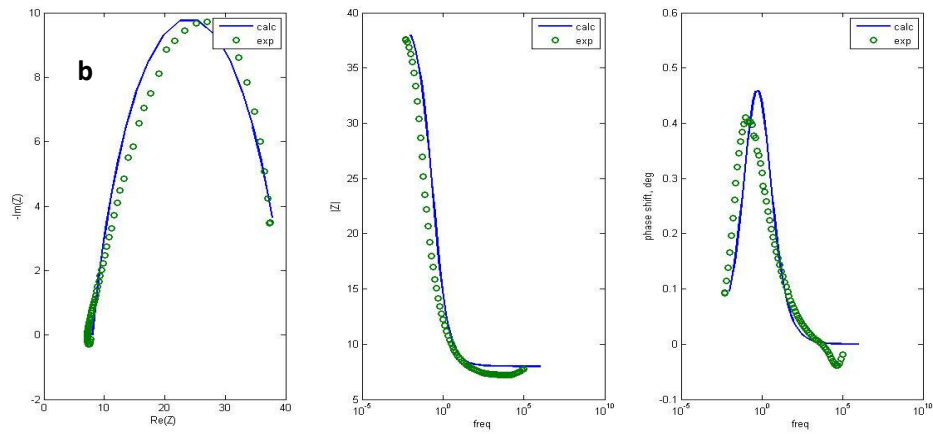


Figure 3.26.b $\text{La}_{0.6}\text{Sr}_{0.4}\text{Ga}_{0.3}\text{Fe}_{0.7}\text{O}_3$ - synthesized @ $1100^\circ\text{C}-520^\circ\text{C}$

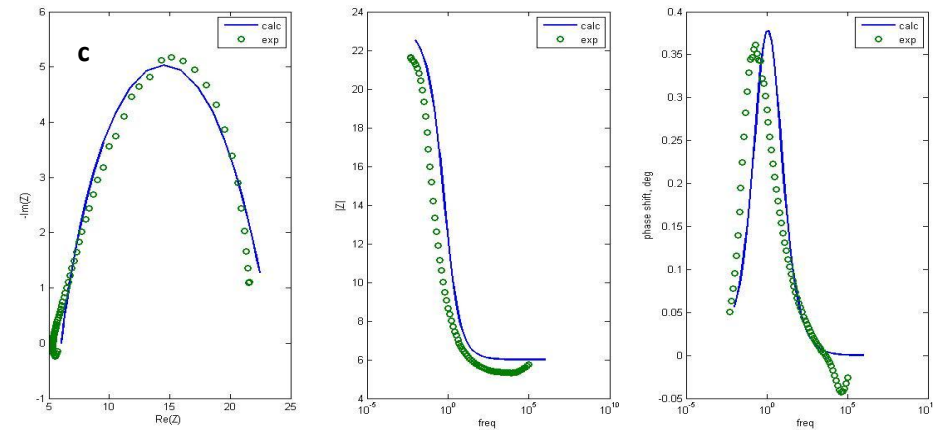


Figure 3.26.c $\text{La}_{0.6}\text{Sr}_{0.4}\text{Ga}_{0.3}\text{Fe}_{0.7}\text{O}_3$ - synthesized @ $1100^\circ\text{C}-545^\circ\text{C}$

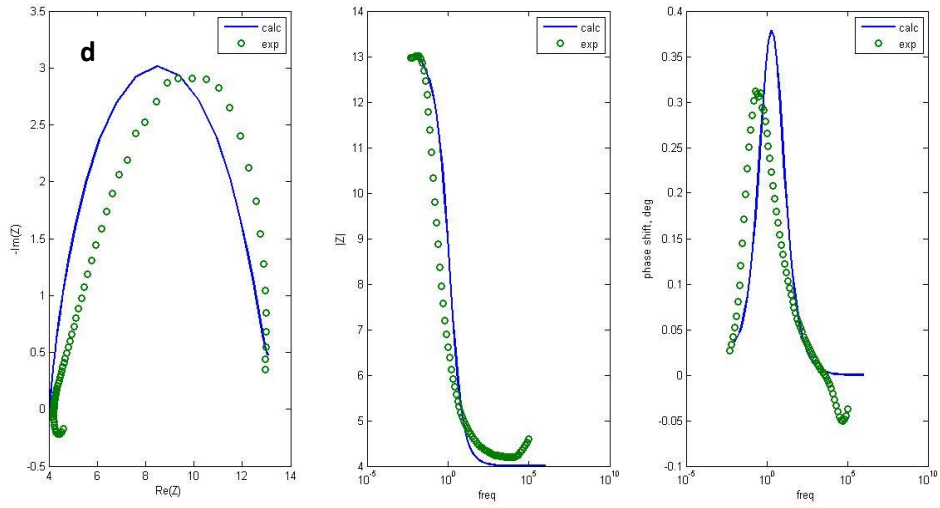


Figure 3.26.d La_{0.6}Sr_{0.4}Ga_{0.3}Fe_{0.7}O₃ - synthesized @ 1100°C-570°C

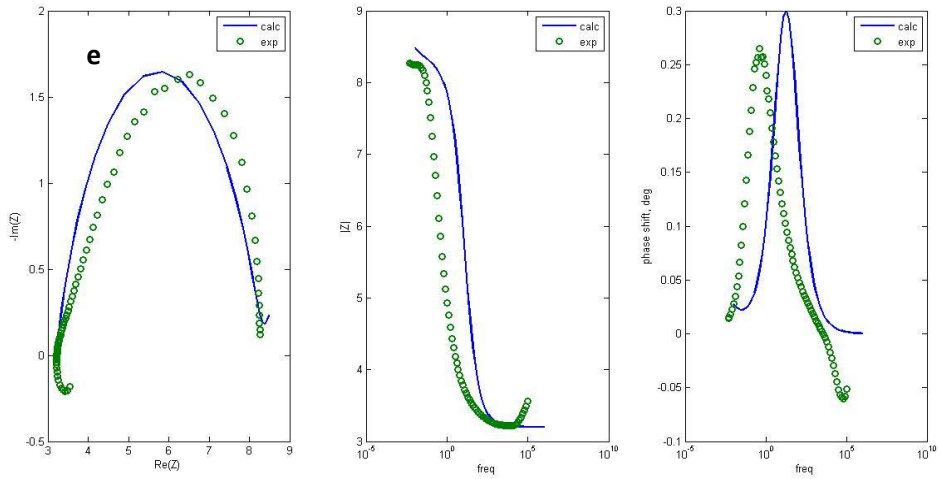


Figure 3.26.e La_{0.6}Sr_{0.4}Ga_{0.3}Fe_{0.7}O₃ - synthesized @ 1100°C-595°C

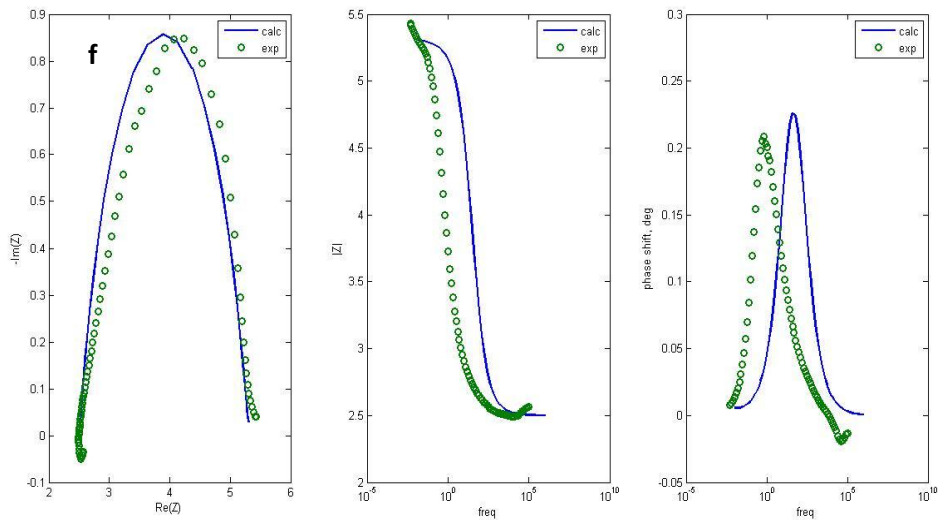


Figure 3.26.f La_{0.6}Sr_{0.4}Ga_{0.3}Fe_{0.7}O₃ - synthesized @ 1100°C-620°C

Table 3.3 Parameters for sample B

La _{0.6} Sr _{0.4} Ga _{0.3} Fe _{0.7} O ₃ – synthesized @ 1100°C					
T(°C)	R1(Ω)	R2(Ω)	C(F)	a	W(Ωs ^{-1/2})
495	10	70	2,00E-02	0,65	0,05
520	8	32	3,00E-02	0,7	0,05
545	6	17	3,00E-02	0,68	0,05
570	4	9	3,00E-02	0,75	0,05
595	3,2	5,1	1,00E-02	0,73	0,05
620	2,5	2,8	1,00E-02	0,7	0,005

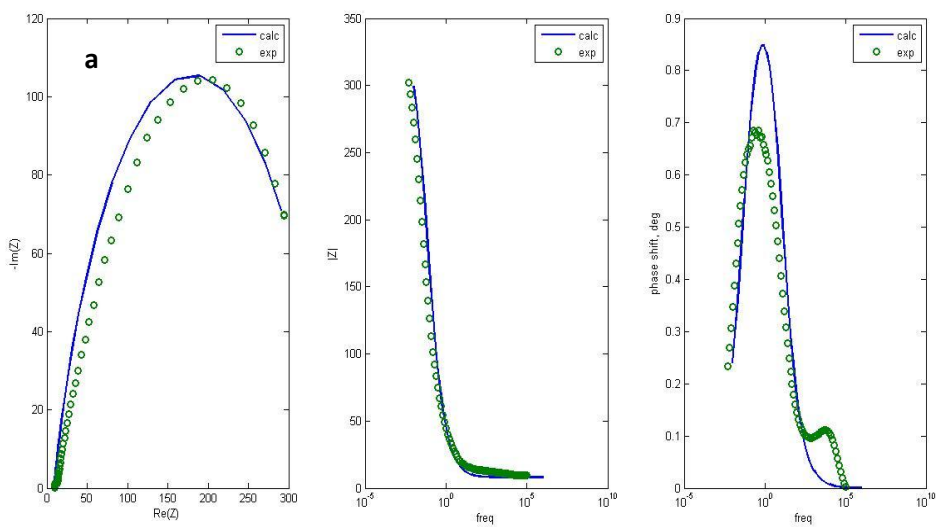


Figure 3.27.a La_{0.6}Sr_{0.4}Ga_{0.3}Fe_{0.7}O₃ +MnOx - synthesized @1000°C-490°C

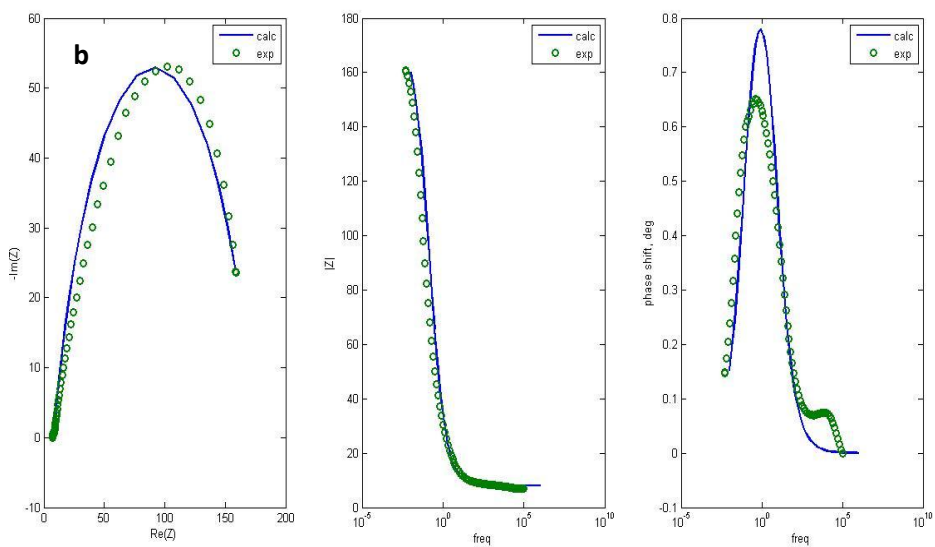


Figure 3.27.b La_{0.6}Sr_{0.4}Ga_{0.3}Fe_{0.7}O₃ +MnOx - synthesized @1000°C-520°C

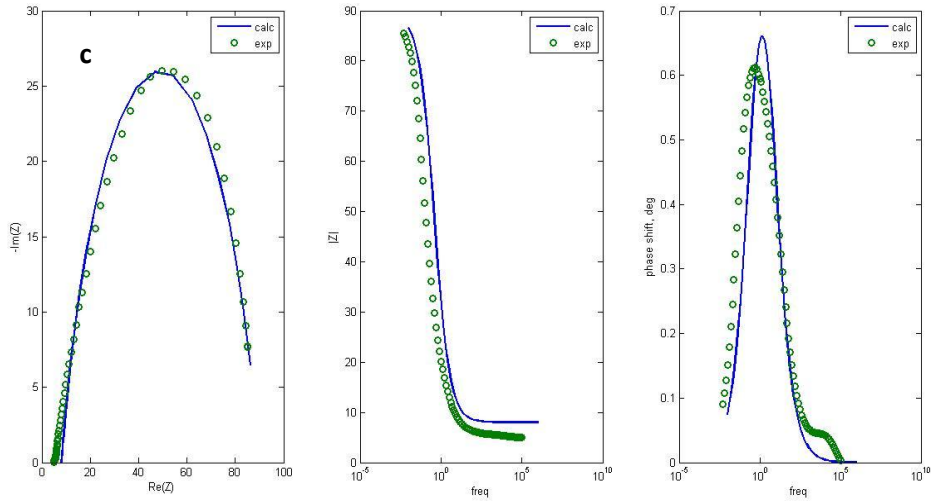


Figure 3.27.c La_{0.6}Sr_{0.4}Ga_{0.3}Fe_{0.7}O₃ + MnO_x - synthesized @ 1000°C-545°C

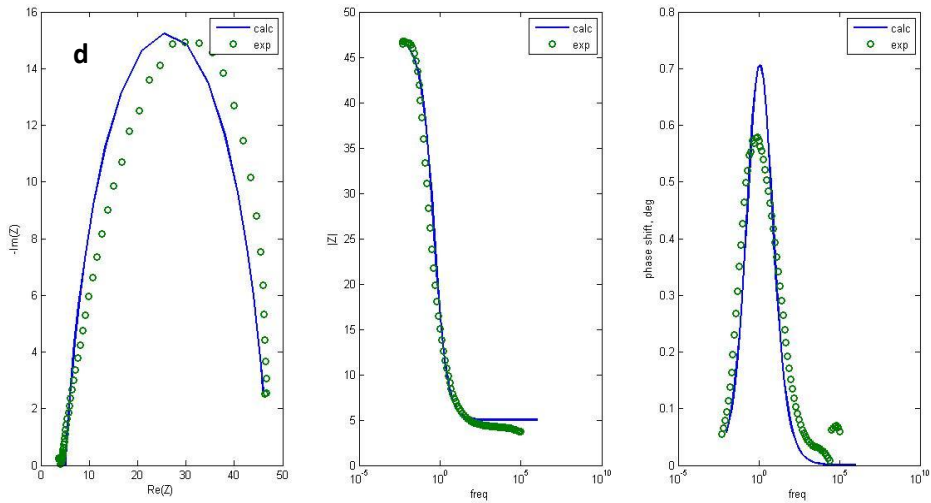


Figure 3.27.d La_{0.6}Sr_{0.4}Ga_{0.3}Fe_{0.7}O₃ + MnO_x - synthesized @ 1000°C-570°C

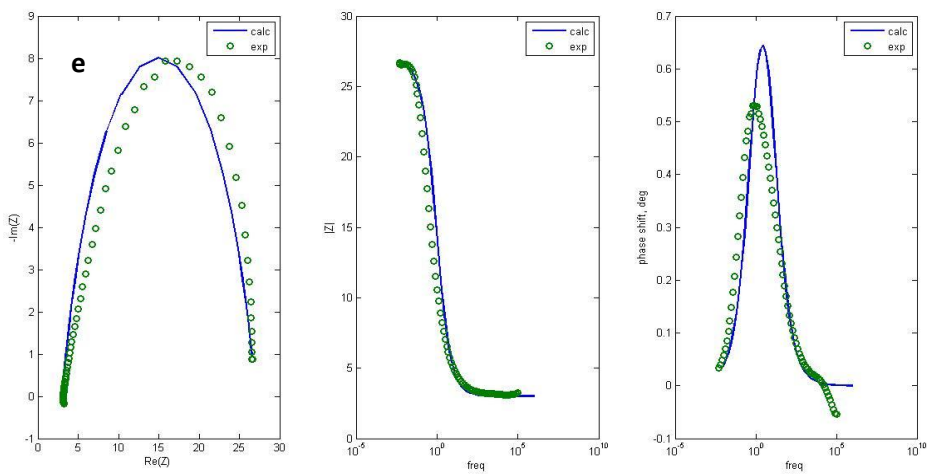


Figure 3.27.e La_{0.6}Sr_{0.4}Ga_{0.3}Fe_{0.7}O₃ + MnO_x - synthesized @ 1000°C-595°C

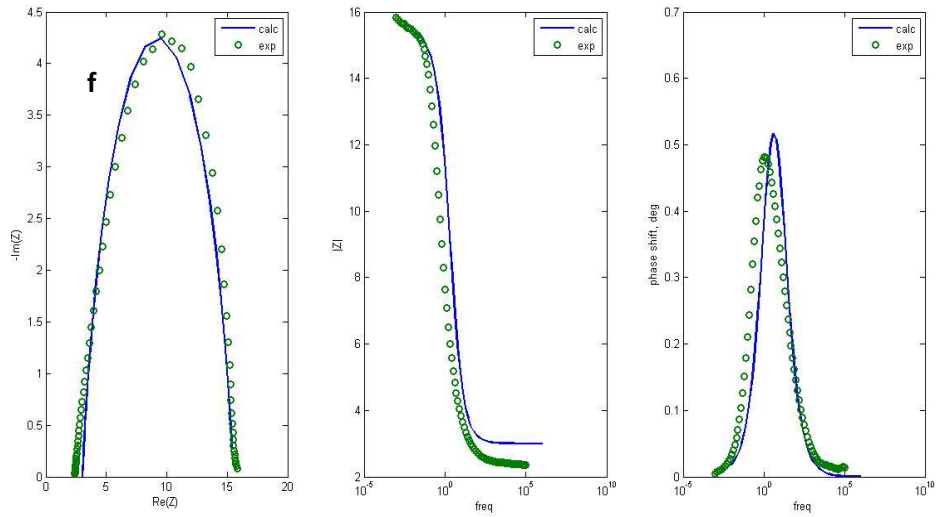


Figure 3.27.f La_{0.6}Sr_{0.4}Ga_{0.3}Fe_{0.7}O₃ + MnOx - synthesized @1000°C-620°C (1)

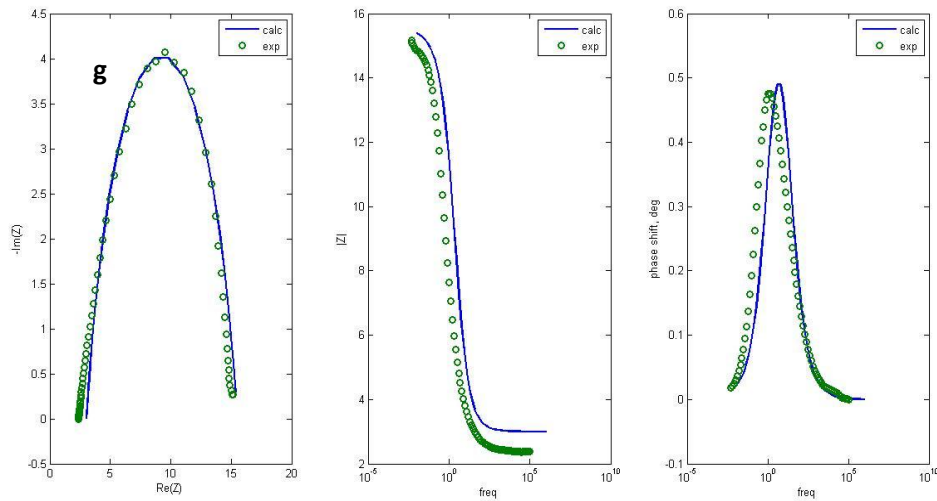


Figure 3.27.g La_{0.6}Sr_{0.4}Ga_{0.3}Fe_{0.7}O₃ + MnOx - synthesized @1000°C-620°C (2)

Table 3.4 Parameters for sample C

La _{0.6} Sr _{0.4} Ga _{0.3} Fe _{0.7} O ₃ + MnOx – synthesized @ 1000°C					
T(°C)	R1(Ω)	R2(Ω)	C(F)	a	W(Ωs ^{-1/2})
490	8	345	6,50E-03	7,00E-01	0,005
520	8	167	8,50E-03	0,72	0,005
545	8	82	8,50E-03	0,72	0,005
570	5	42	1,50E-02	0,8	0,005
595	3	24	1,50E-02	0,75	0,005
620_1	3	12,5	1,50E-02	0,73	0,005
620_2	3	12,5	1,50E-02	0,76	0,005

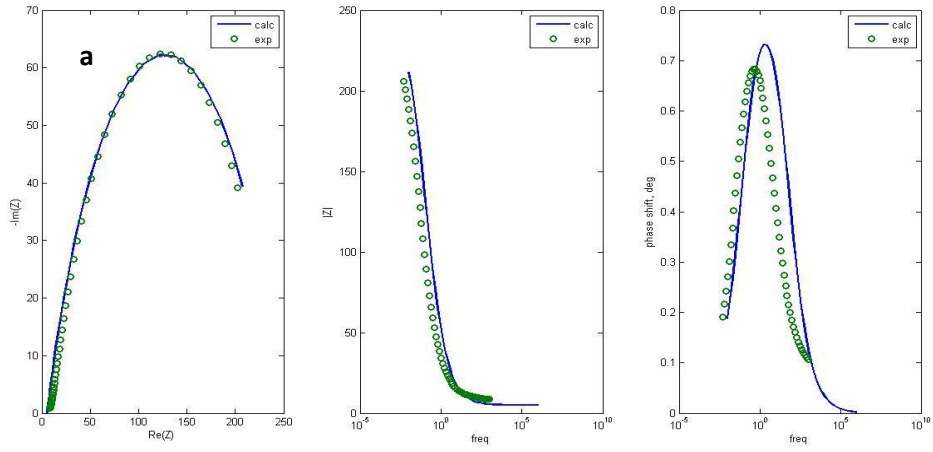


Figure 3.28.a $\text{La}_{0.6}\text{Sr}_{0.4}\text{Ga}_{0.3}\text{Fe}_{0.7}\text{O}_3 + \text{MnOx}$ - synthesized @ 1100°C - 495°C

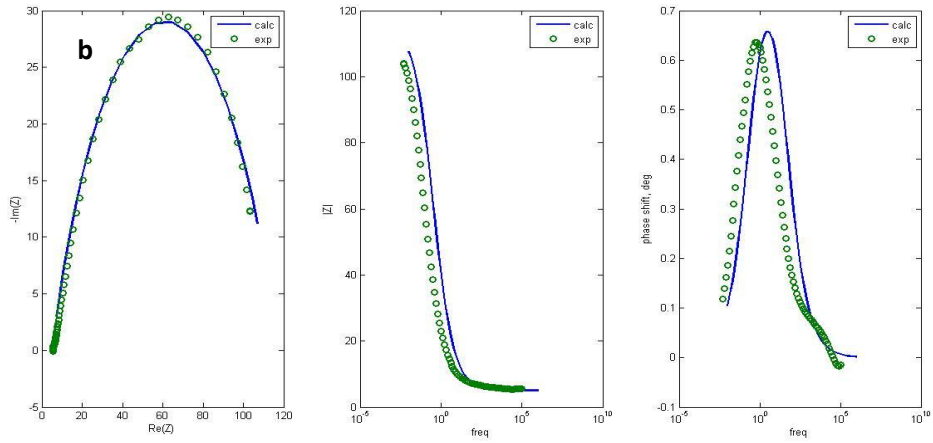


Figure 3.28.b $\text{La}_{0.6}\text{Sr}_{0.4}\text{Ga}_{0.3}\text{Fe}_{0.7}\text{O}_3 + \text{MnOx}$ - synthesized @ 1100°C - 520°C

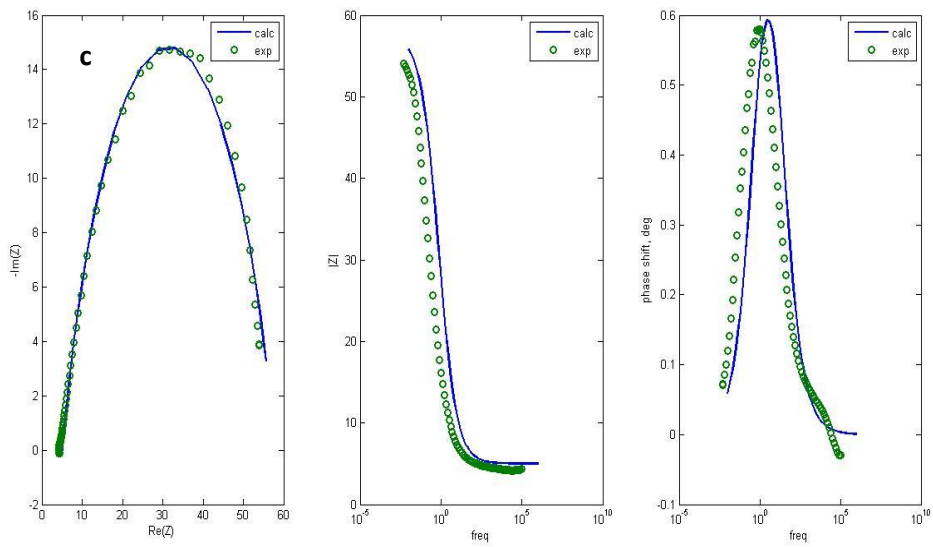


Figure 3.28.c $\text{La}_{0.6}\text{Sr}_{0.4}\text{Ga}_{0.3}\text{Fe}_{0.7}\text{O}_3 + \text{MnOx}$ - synthesized @ 1100°C - 545°C

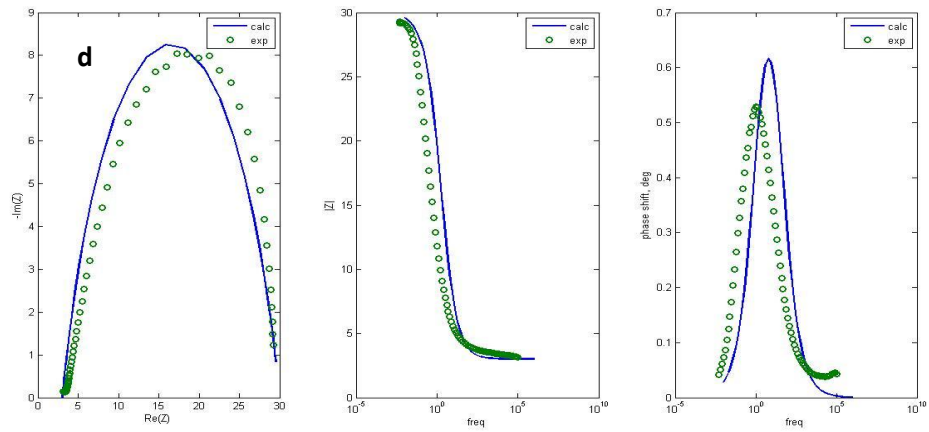


Figure 3.28.d $\text{La}_{0.6}\text{Sr}_{0.4}\text{Ga}_{0.3}\text{Fe}_{0.7}\text{O}_3 + \text{MnO}_x$ - synthesized @ 1100°C - 570°C

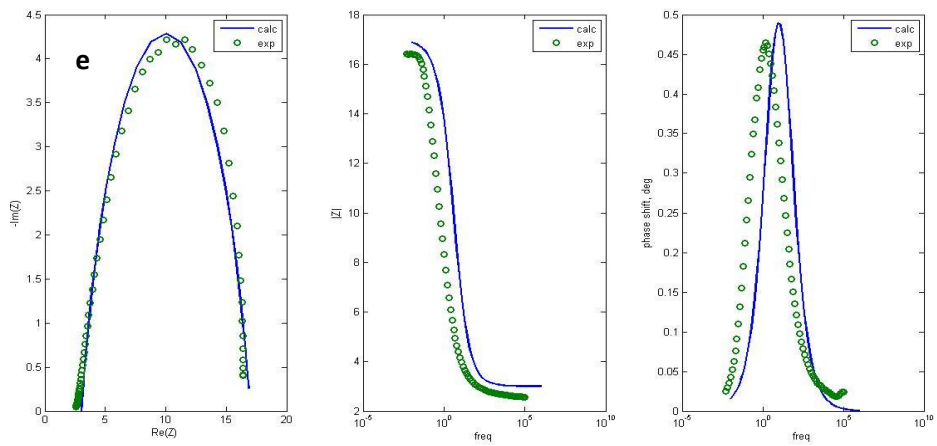


Figure 3.28.e $\text{La}_{0.6}\text{Sr}_{0.4}\text{Ga}_{0.3}\text{Fe}_{0.7}\text{O}_3 + \text{MnO}_x$ - synthesized @ 1100°C - 590°C

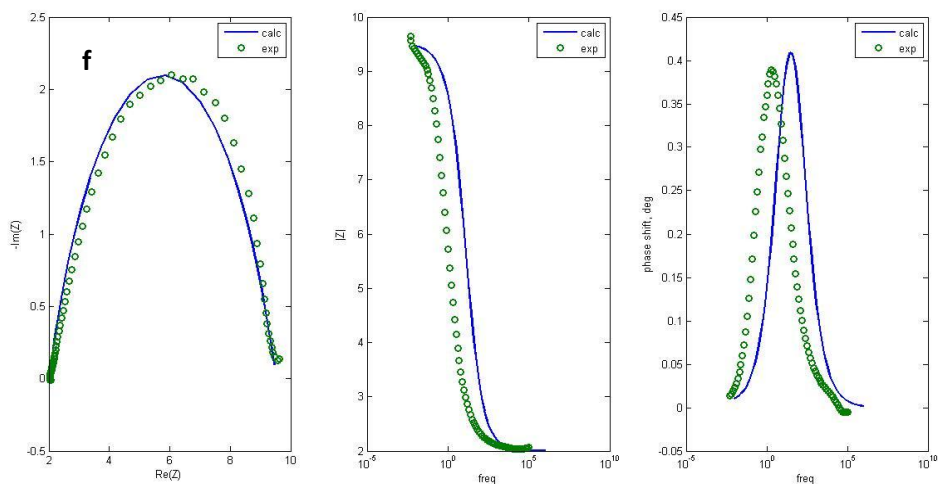


Figure 3.28.f $\text{La}_{0.6}\text{Sr}_{0.4}\text{Ga}_{0.3}\text{Fe}_{0.7}\text{O}_3 + \text{MnO}_x$ - synthesized @ 1100°C - 620°C

Table 3.5 Parameters for sample D

La _{0.6} Sr _{0.4} Ga _{0.3} Fe _{0.7} O ₃ + MnOx – synthesized @ 1100°C					
T(°C)	R1(Ω)	R2(Ω)	C(F)	a	W(Ωs ^{-1/2})
495	5	245	6,00E-03	6,00E-01	0,005
520	5	113	7,00E-03	0,61	0,005
545	5	53	9,00E-03	0,65	0,005
570	3	27	9,00E-03	0,7	0,005
595	3	14	9,50E-03	0,7	0,005
620	2	7,5	9,50E-03	0,65	0,005

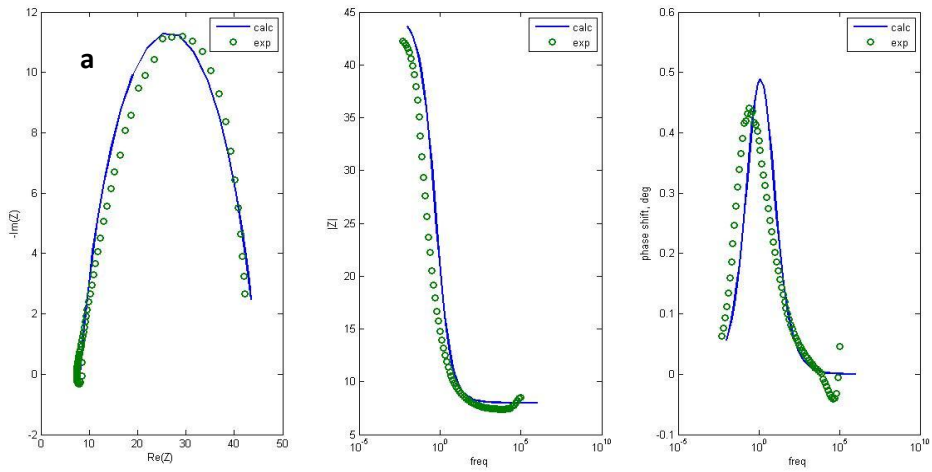


Figure 3.29.a La_{0.6}Sr_{0.4}Ga_{0.3}Fe_{0.7}O₃ + FeOx - synthesized @ 1000°C-495°C

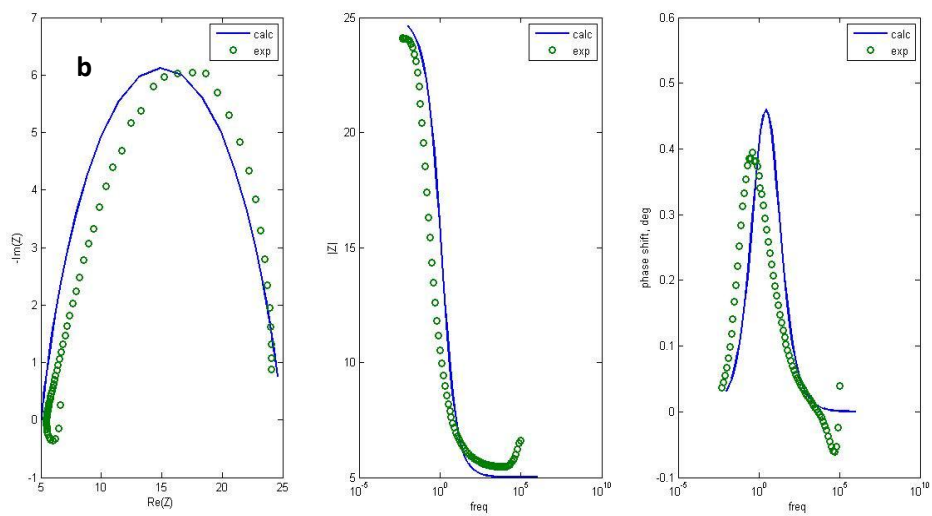


Figure 3.29.b La_{0.6}Sr_{0.4}Ga_{0.3}Fe_{0.7}O₃ + FeOx - synthesized @ 1000°C-520°C

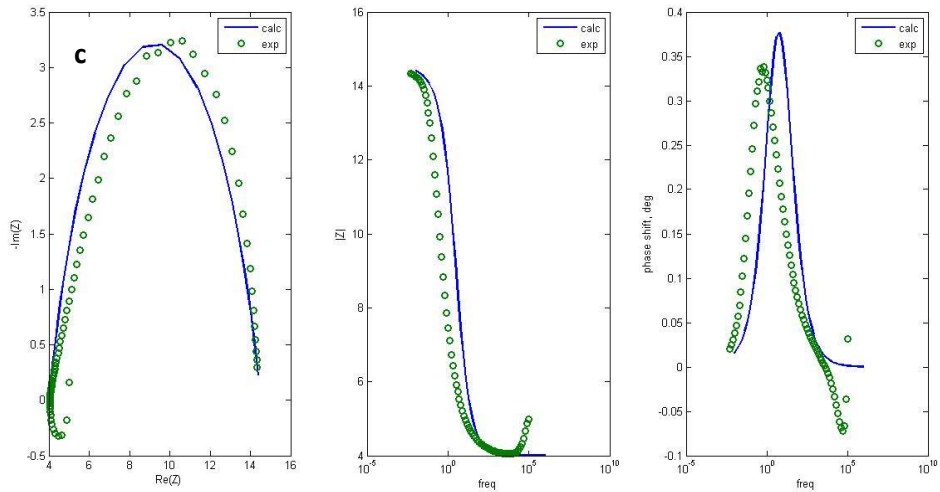


Figure 3.29.c La_{0.6}Sr_{0.4}Ga_{0.3}Fe_{0.7}O₃ + FeO_x - synthesized @1000°C-545°C

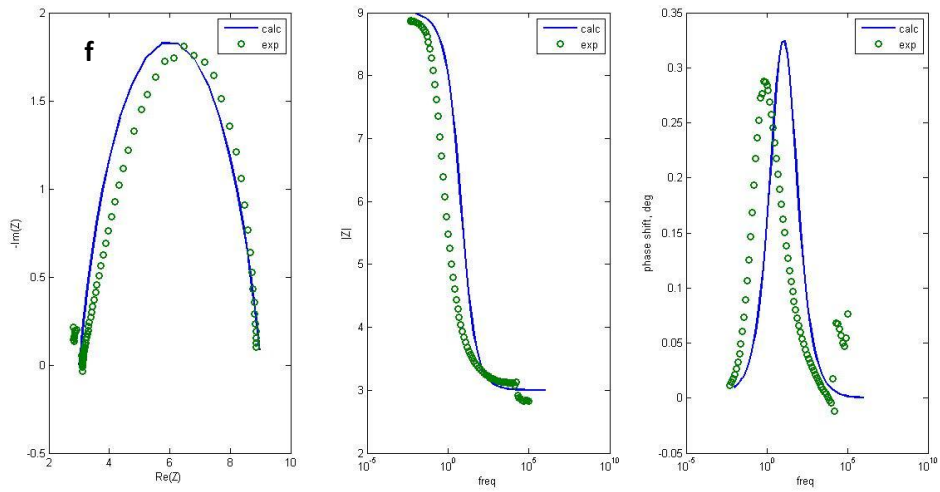


Figure 3.29.d La_{0.6}Sr_{0.4}Ga_{0.3}Fe_{0.7}O₃ + FeO_x - synthesized @1000°C-570°C

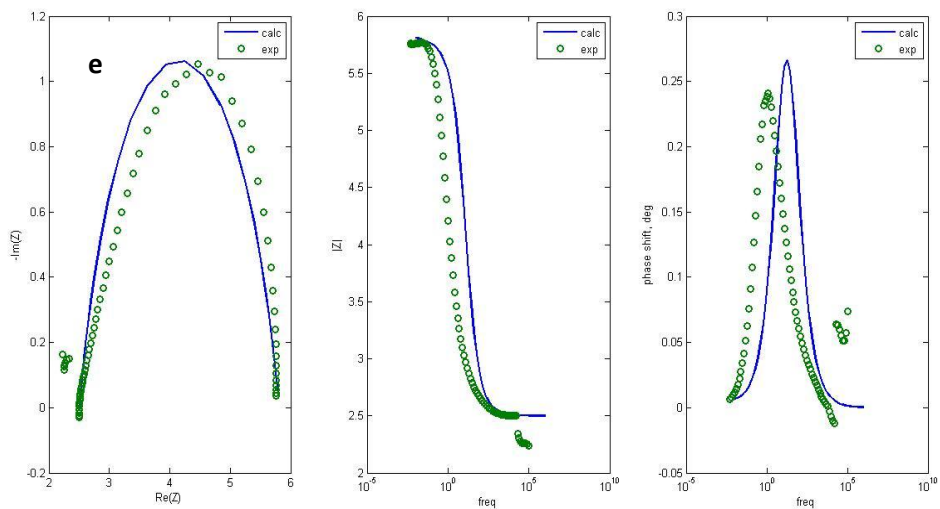


Figure 3.29.e La_{0.6}Sr_{0.4}Ga_{0.3}Fe_{0.7}O₃ + FeO_x - synthesized @1000°C-595°C

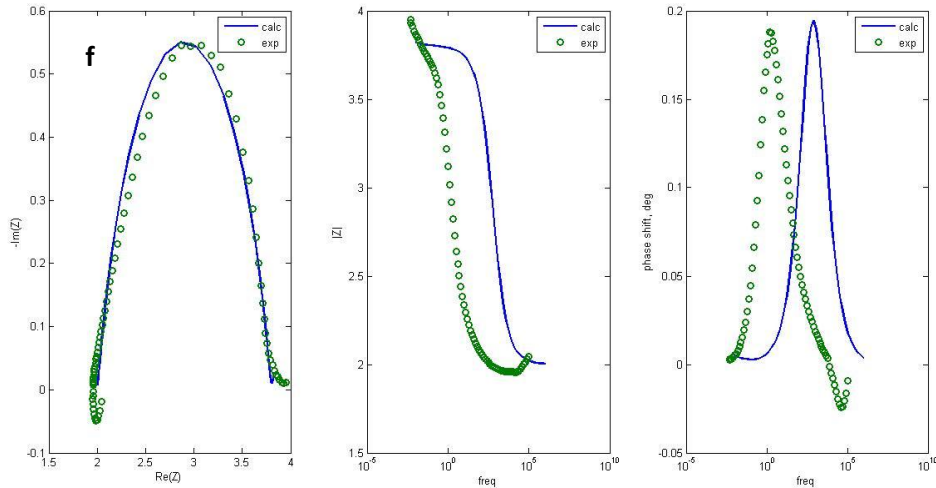


Figure 3.29.f La_{0.6}Sr_{0.4}Ga_{0.3}Fe_{0.7}O₃ +FeOx - synthesized @1000°C-620°C

Table 3.6 Parameters for sample E

La _{0.6} Sr _{0.4} Ga _{0.3} Fe _{0.7} O ₃ + FeOx – synthesized @ 1000°C					
T(°C)	R1(Ω)	R2(Ω)	C(F)	a	W(Ωs ^(-1/2))
495	8	37	1,50E-02	7,00E-01	0,005
520	5	20	1,50E-04	0,7	0,005
545	4	10,5	1,50E-02	0,7	0,005
545	4	10,5	1,50E-02	0,7	0,005
570	3	6	1,50E-02	0,7	0,005
620	2	1,8	2,00E-03	0,7	0,005

Interpretation of the single E parameters can be achieved through the explanations in the precedent paragraphs. As stated before, it can be observed that an increase in temperature leads to a reduction in parameters, reaffirming that high temperatures are essential when it comes to these materials and the reactions that take place within them.

Also, it can be declared that the EEC used for the fitting can in fact represent the phenomena occurring in the system. The fact that some fittings do not prove themselves as accurate does not mean an erroneous fitting but the need to consider an additional parameter to explain in a more accurate way what is going on.

Table 3.7 lists the parameters for all samples at the highest possible temperature, allowing for a better comparison between them. As predicted before, sample E provides the better performance among all the samples considered.

Furthermore, considering the trend suggested earlier, it can be assumed that the same material synthesized at higher temperatures could provide an even better performance by minimizing both the capacitive and resistive behavior.

Table 3.7 Comparison of parameters for $\text{La}_{0.6}\text{Sr}_{0.4}\text{Ga}_{0.3}\text{Fe}_{0.7}\text{O}_3$

Coating	Temperature °C	Rct Ω	Rel Ω	Cdl F	a	W $\Omega\text{s}^{0.5}$
No @ 1000°C	585	3	15	7×10^{-2}	0.6	0.05
No @ 1100°C	620	2.5	2.8	1×10^{-2}	0.7	0.005
MnOx @ 1000°C	620	3	12.5	1.5×10^{-2}	0.76	0.005
MnOx @ 1100°C	620	2	7.5	9.5×10^{-3}	0.65	0.005
FeOx @ 1000°C	620	2	1.8	2×10^{-3}	0.7	0.005

3.2 Conductivity Measurements

3.2.1 Gas Chromatography Setup

A key parameter while carrying conductivity measurements is the selection of the sweep gas and the reference gas of the GC (the method chosen for quantification of O_2). The sensibility of the instrument depends strongly on this coupling and it must be ensured that the gas chromatographer can detect the expected quantity of oxygen (ca. one hundred O_2 molecules in a couple hundred molecules).

Even though Ar is the sweep gas used in literature it was found that The GC cannot perceive less than a concentration of 0.5% of air in Ar, which is well above the values expected. This can be seen in figure 3.24, which shows a noisy base line of the chromatogram that could lead to integration inaccuracies.

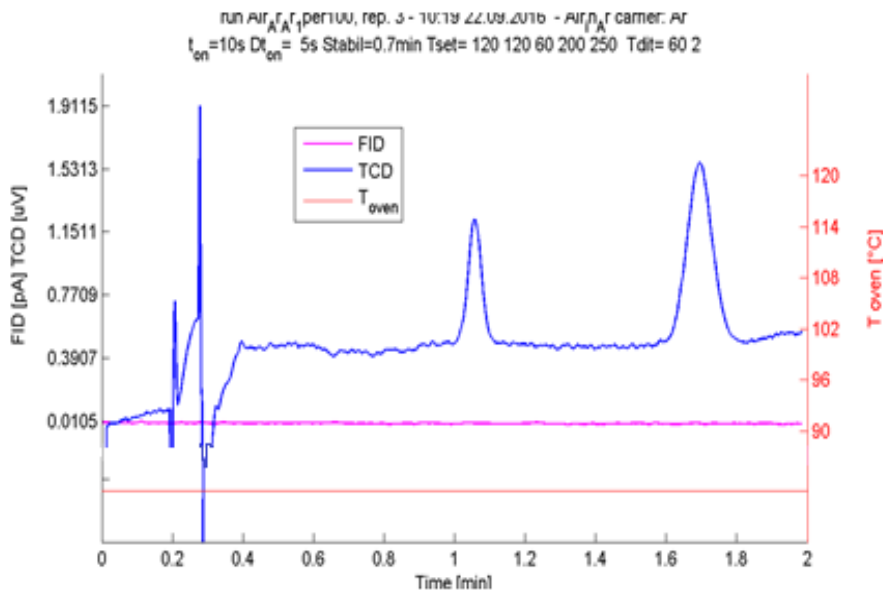


Figure 3.24 Chromatogram of 0.5% air in Ar

It was then attempted to still use Ar as sweep gas while changing the reference gas to He, a non-so desirable coupling due to the appearance of a third peak. However, this choice proved to be worse than expected because of the superposition of the He and O₂ peaks.

Figure 3.25 shows the chromatogram of a mix made by 0.5% air, 0.5% Ar in He. Since the component analysis is done through a thermal conductivity difference, now the presence of a third peak can be observed because the sweep gas and the carrier gas are no longer the same one.

Even at small compositions and at the lowest temperature the GC available can work, it is impossible under these conditions to separate both elements. It has been proven that such small quantities can be separated either with the use of long (20/30 mt.) capillary columns or by reaching cryogenic temperatures. However, no successful separation of a small quantities of oxygen in great quantities of Ar has been found in literature, which leads to think such feat as impossible.

Finally, it was established that using helium both as sweep and reference gas was the only available option to achieve the required sensibility. In fact, as can be seen from figure

3.26, in this way it is possible to quantify concentrations of 0.05% air in He, one order of magnitude less with respect to case where Ar is used both as carrier and sweep gas.

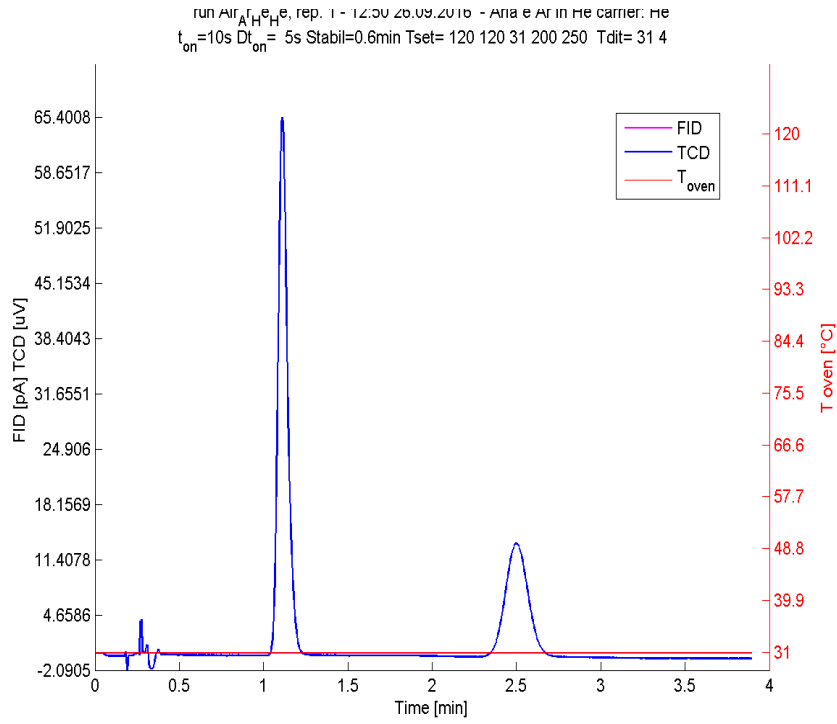


Figure 3.25 Chromatogram of 0.5% air, 0.5% Ar in He

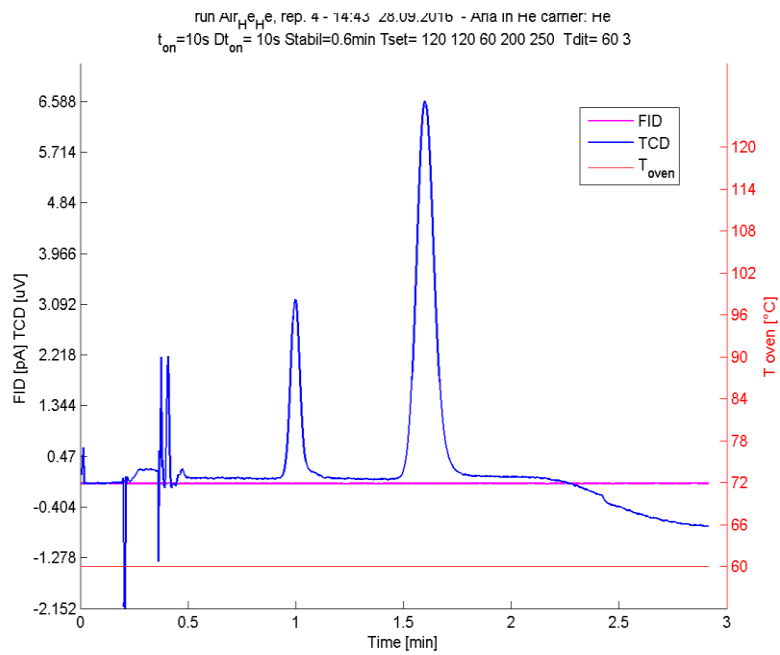


Figure 3.26 Chromatogram of 0.05% air in He

3.2.2 Experimental Measurements and its Problematics

Attempts of conductivity measurements on the ceramic materials studied in the first part of the chapter were carried but without achieving great success. Diverse problematics have arisen, all of them of diverse nature, which will subsequently be explained.

The first problem to be overcome is the dilatation of the silicic paste used to hold the pieces together. At elevated temperatures, the cement tends to dilate thus allowing oxygen to pass through due to the dimension of the cavities.

This imposes a need to send pure air ($O_2=21\%$, $N_2=79\%$) to one of the faces of the sample. The use of pure air instead of 100% oxygen derives from a malfunction of the cement holding the sample in place. By knowing the exact O_2/N_2 ratio, it is possible to quantify how much oxygen has passed through ionic migration and dilatation of the cement.

Since, as explained in the previous section, helium was chosen as sweep gas, the dilatation of the cement may lead to another issue: leakage of He through the ceramic paste due to its dimension. It is sensible to assume that if air can pass through, also helium can go pass in the opposite direction since it is smaller.

To verify a possible leakage of He the same configuration reported before was used, this time substituting the ceramic button with an impermeable material. Both the composition of the air and the total flux of the sweep gas and the air were to be measured. By doing so two new difficulties were found, one for each type of measurement carried.

While determining the conservation of flux passing through the lower side of the cell, it was observed that in fact there was a leakage of mix. Nonetheless, this leak proved to be different from the one expected since it was caused by a non-perfect isolation between the different sections of the permeation cell.

This loss in sweep gas became even bigger the moment the ceramic material was used because of its intrinsic fragility. Assemblage of the system produced enough stresses as to crack the ceramic, allowing a contact between the lower and the upper side and consequently a loss of He from the upper side.

Independently of this issue, another complication related to chromatographic analysis arose. As can be observed in figure 3.27, an unexpected element came into view while analyzing the mix coming out of the cell.

Due to the form in which it appears, not as a well-defined peak but as a curvy enlarged one, the presence of water inside the permeation cell was hypothesized. This assumption was furtherly validated through a Hiden analysis (mass spectroscopy), which showed the appearance of water (figure 3.28-green line) the moment the flux was changed from a direct connection to the GC to a connection that passed first through the cell. Through the whole experiment helium seemed to be constant enough as can be seen from the red line.

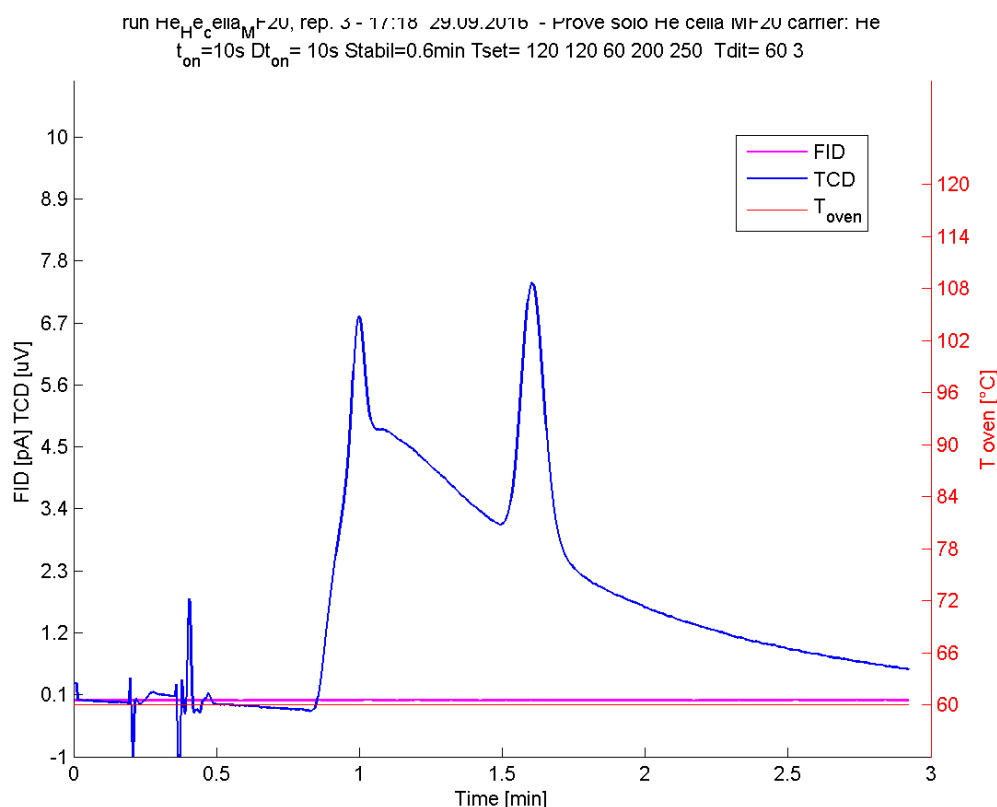


Figura 3.27 Chromatogram containing wáter

The presence of water inside the cell was associated to the water released by the silionic paste, which unfortunately was not possible to remove because of continuous breakage of the ceramic button, especially at high temperatures.

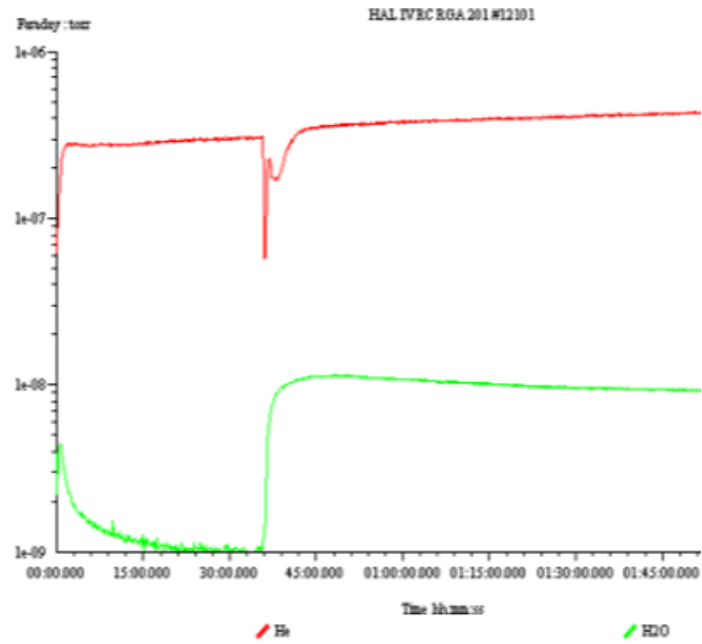


Figura 3.28 Mass spectroscopy analysis of elements present in the cell

The fact that these types of analysis must be carried in a wide range of temperature also made it clear that while this is in fact possible, heating and cooling ramps have to be slow enough as not to create internal stresses within the material that could lead to mechanical damages

Because of all these hindrances, ionic measurements could not be carried to completion yet it allowed for identification of problems that need to be corrected in future permeation setups.

CONCLUSIONS

Among the many alternatives available now a day as a renewable substitution to fossil fuels, fuel cells are among the researched ones. The various configurations available in the market allow for adaptation to different environments and needs.

The purpose of the study was to understand and implement two of the most common techniques that serve to characterize solid oxide fuel cells: Electrochemical Impedance Spectroscopy and Ionic Conductivity measurements.

The ultimate goal when one speaks of fuel cells is to make way to new materials that work at lower temperatures (500/600°C) with respect to the commercial, available ones. Such materials, however, need to demonstrate that their performance does not worsen while working at such temperatures. This is the reason why the two techniques aforementioned are of great relevance within the electrochemical field.

The present thesis proposed an alternative implementation to the conventional analysis of EIS through the use of an e-load instead of a potentiostat. Analysis on diverse circuitual elements proved in fact that such a configuration is possible under the constraint of testing only at low frequencies (less than 10 kHz).

Furthermore, a venture at EIS data interpretation was carried through the the use of electrical equivalent circuits theorem. By comparing different samples made up by the same base material but differing in coating and synthetization temperatures, it was determined that $\text{La}_{0.6}\text{Sr}_{0.4}\text{Ga}_{0.3}\text{Fe}_{0.7}\text{O}_3$ coated with ferrous oxide synthetized at 1100°C provided the best performance. Through this analysis it was observed that characteristics of the material improve with synthetization temperature and that a coating may or may not improve the overall behavior of the material.

Also, an attempt at ionic conductivity was made. Yet the approach used proved to be ineffective due to succession of problematics that could not be overcome and that lead to the conclusion that the setup chosen was not appropriate at all.

CONCLUSIONI

Tra le diverse alternative di energia rinnovabile con cui a giorno di oggi si possono sostituire i combustibili fossili, le celle combustibile si trovano tra le più ricercate. Le diverse configurazioni disponibili in mercato permettono una buona adattamento per diversi ambienti e bisogni.

L'obiettivo di questo studio è stato capire ed implementare due delle più comuni tecniche che servono a caratterizzare le celle combustibili ceramiche: la Spettroscopia d'Impedenza Elettrochimica e le misure di Conduttività Ionica.

Lo scopo finale, quando uno parla di SOFC, è di aprire campo a nuovi materiali che lavorano a temperature più basse (500/600°C) rispetto a quelli che attualmente si trovano in commercio. Tuttavia questi materiali devono dimostrare di non peggiorare le loro prestazioni con l'abbassarsi della temperatura. Questo è il motivo per cui le due tecniche appena citate sono di grande importanza nell'ambito elettrochimico.

Questa tesi ha proposto una implementazione alternativa alle convenzionali misure di EIS attraverso l'uso di un carico elettrico invece di un potenziostato. Analisi su diversi elementi circuitali hanno dimostrato che effettivamente questa configurazione è possibile di usare ma è vincolata dalle basse frequenze che riesce a leggere (meno di 10 kHz).

Oltretutto, c'è stato un tentativo di interpretazione di data EIS tramite il teorema dei circuiti equivalenti. Comparando diversi campioni fatti tutti dello stesso materiale ma differendo in temperatura di sintetizzazione e ricoperture, si è determinato che il $\text{La}_{0.6}\text{Sr}_{0.4}\text{Ga}_{0.3}\text{Fe}_{0.7}\text{O}_3$ ricoperto di ossido di ferro sintetizzato a 1100°C procurava le migliori prestazioni. Attraverso questo analisi si ha anche visto che le proprietà dei materiali migliorano se questo viene sintetizzato a temperature maggiore e che eventuali ricoperture possono sia peggiorare che migliorare il comportamento complessivo del materiale.

Inoltre si ha provato a fare delle misure di conducibilità ionica. Tuttavia, l'approccio utilizzato si è verificato inefficace a causa di una serie di problematiche che non potevano essere risolte per cui si è arrivato alla conclusione che la configurazione scelta non era adatta alla situazione.

NOMENCLATURE AND ABBREVIATIONS

α	Electron Transfer Coefficient
AC	Alternate Current
AFC	Alkaline Fuel Cell
C	Capacitance
CC	Constant Current
CPE	Constant Phase Element
CR	Constant Resistance
CSTR	Continuously Stirred Tank Reactor
CV	Constant Voltage
DC	Direct Current
E	Electrode Potential
E°	Standard Electrode Potential
EEC	Electrical Equivalent Circuits
EIS	Electrochemical Impedance Spectroscopy
F	Faraday Constant
f	Frequency
f_{bin}	Binary Frequency
G	Gibbs Free Energy
G°	Standard Gibbs Free Energy
GC	Gas Chromatographer

GCO	Gadolinium Doped Ceria
FC	Fuel Cell
FCC	Face Centered Cubic
FFT	Fourier Transform
J	Flux
j	Current Density
j_0	Exchange Current Density
L	Membrane Thickness
L	Inductance
LSGM	Lanthanum Gallate doped with Strontium Oxide and Magnesium
MIEC	Mixed Ionic and Electronic Conductivity
n	Number of Electrons transferred
N_p	Number of Points
[Ox]	Concentration of the Oxidized Species
P'	Partial Pressure
R	Gas Constant
R	Resistance
[Red]	Concentration of Reduced Species
σ	Conductivity
SCOT	Support-Coated Open Tubular
SCPI	Standard Command for Programmable Instruments
SOFC	Solid Oxide Fuel Cell
T	Temperature

TPB	Three Phase Boundary
t_s	Time of Test Sample
ω	Angular Frequency
W	Warburg
WCOT	Wall-Coated Open Tubular
Y_0	Diffusion Admittance
YSZ	Yttria Stabilized Zirconia
Z	Impedance

BIBLIOGRAPHY

1. Gennaro, A. *Lecture Notes*
2. *FuelCellToday*, Johnson Matthey Plc 2016 (www.fuelcelltoday.com)
3. DoE U.S, *Fuel Cell Facts Sheet*, 2015
(www.energy.gov/sites/prod/11/f27/fcto_fuel_cells_fact_sheet.pdf)
4. Woodrow, W.C; Grant, C. *Global Energy Innovation: Why America Must Lead* 2011 Prager, Santa Barbara (CA)
5. <http://www.climatetechwiki.org/technology/stationary-fuel-cells>
6. Stimming, U.; Carrette, L.; Friedrich, A.K; *ChemPhysChem* 2000, 1, 162-193
7. Minh N.Q.; *J. Am. Ceram. Soc.* 1993, 76, 563-588.
8. Singhal S.C.; *Electrochem Soc Interface* 2007, 41-44
9. Stambouli, A. B.; Traversa, E.; *Renew. Sustainable Energy Rev.* Vol. 6, 2002, 5,433–455
10. Mangifesta, P.; *Semicelle SOFC: Studio e produzione di elettroliti con processi a basso impatto ambientale*, 2009, Tesi Magistrale
11. Fergus, J.W.; *J. Power Sources* Vol. 162, 2006, 1, 30–40
12. Chen, X. J.; Khor, K.A.; Chan, S.H; Yu, L.G.; *Mater. Sci. Eng., A* Vol. 335, 2002, 1-2, 246–252
13. Jetske, K.; *Ionic Conductivity in Ytria-Stabilized Zirconia Thin Films grown by Pulsed Laser Deposition*, 2005, M. Sc. Thesis
14. Kim, N.; Kim, B.H.; Lee, D.; *J. Power Sources* Vol. 90, 2000, 2, 139-143
15. Viswanathan, R. et al.; *Processing and Application of Ceramics*, 2009, 3, 137-143
16. Tas, A. C.; Majewski, P. J.; Aldinge, F.; *J. Am. Ceram. Soc.*, 2000, 83 2954 – 60
17. Lia, B.; Liua, S.; Liub, X.; Haob, G.; Wangb, H.; Sub, W.; *Int. J. Hydrogen Energy*, Vol. 38, 2013, 26, 11392–11397
18. Richter, J.; Holtappels, P.; Graule, T.; Nakamura, T.; Gauckler, L.J.; *Monatsh. Chem.*, 2009, 140, 985–999
19. Skinner, S.J.; *Fuel Cells Bull.*, Vol. 4, 2001, 33, 6-12
20. Giesbers, A.; *Development of cathodes for low temperature solid oxide fuel cells Oxygen reduction mechanism*, 2004, M. Sc. Thesis
21. Ribeiroa, N.F.P.; Souza, M.M.V.M.; Netoa O.R.M.; Vasconcelosa, S.M.R.; Schmala, M.; *Appl. Catal., A*, Vol. 353, 2009, 2, 305–309

22. Gorte, R.J.; Kim, H.; Vohs, J.M.; *J. Power Sources* Vol. 106, **2002**, 1–2, 1, 10–15
23. Gorte, R.J.; Vohs, J.M.; *J. Colloid Interface Sci.* Vol. 14, **2009**, 4, 236–244
24. Hjelm, J.; Nielsen, J.; *Electrochim. Acta* , Vol. 115, **2014**, 31–45
25. Riess, I.; *Solid State Ionics*, **2003**, 157, 1 – 17
26. Sunarsoa, J.; Baumann, S.; Serrca, J.M.; Meulenberg, W.A.; Liua, S.; Lind, Y.S.; Diniz da Costa, J.C.; *J. Membr. Sci.*, **2008**, 320, 13–41
27. Lindegaard, T.; Mogensen, M.; Hansen, U. R.; *J. Electrochem. Soc.*, Vol 141, **1994** , 8, 2122-2128
28. Geffroy, P.M.; Reichmann, M.; Fouletier, J.; Richet, N.; Chartie, T.; *Chem. Eng. Sci.*, **2013**, 104, 817–828
29. Chen, W.; Nauels, N.; Bouwmeester, H.J.M.; Nijmeijer, A.; Winnubst, L.; *J. Eur. Ceram. Soc.*, **2015**, 35, 3075–3083
30. Autolab Application Note EIS06, *Electrochemical Impedance Spectroscopy (EIS)*, **2011**
31. Breitkopf, C.; *Lecture Series at Fritz-Haber-Institute Berlin*, **2012**
32. Gamry Application Note, *Basics of Electrochemical Impedance Spectroscopy*, **2010**
33. Flemming, J.; Hornes, A.; *Rev. Bras. Ensino Fís.*, Vol. 35, **2013**, 35, 3, 3702: 1-4
34. Ribeiro, D.V.; Souza, C.A.C.; Abrantes, J.C.C.; *Rev. IBRACON Estrut. Mater.*, Vol. 8, **2015**, 4, 529-546
35. Vermeeren, V.; Michiels, L.; *Evolution towards the implementation of point-of-care biosensors*, **2011**, ISBN: 978-953-307-443-6
36. D. D. Macdonald; *Electrochimica Acta*, **2006**, 51, 1376–1388
37. Harrington, D.A.; Van den Driessche, P.; *J. Electroanal. Chem.*, **2004**, 567, 153–166
38. Greenleaf, M.C.; *Phenomenological Equivalent Circuit Modeling of Various Energy Storage Devices*, **2014**, Master Thesis
39. Autolab Application Note EIS03, *Electrochemical Impedance Spectroscopy (EIS)*, **2011**
40. Autolab Application Note EIS02, *Electrochemical Impedance Spectroscopy (EIS)*, **2011**
41. Gamry Application Note, *Potentiostat Fundamentals*, **2015**

42. *Loadstar Sensors*, **2016**
43. Keysight DC Electronic Loads, *User Guide*, **2014**
44. Glisenti, A.; *Lecture Notes*
45. Keysight Technologies Application Note, *Making Fuel Cell AC Impedance*, **2014**
46. Chena, W.; Nauels, N.; Bouwmeester, H. J. M.; Nijmeijer, A.; Winnubst, L.; *J. Eur. Ceram. Soc.*, **2015**, *35*, 3075–3083
47. Zhang, K.; Ge, L.; Ran, R.; Shao, Z.; Liu, S.; *Acta Mater.*, **2008**, *56*, 4876–4889
48. Cozzi, R.; Protti, P.; Ruaro, T. *Elementi di Analisi Chimica Strumentale*, **1998**, Zanichelli, Bologna
49. Sheffield Hallam University; *Gas Chromatography*
(<http://teaching.shu.ac.uk/hwb/chemistry/tutorials/chrom/gaschr.htm>)
50. Agilent Technologies; *What is GC*
(<http://teaching.shu.ac.uk/hwb/chemistry/tutorials/chrom/gaschr.htm>)
51. <https://www.gamry.com/application-notes/EIS/quick-check-of-eis-system-performance/>
52. Bedon, A.; Glisenti, A.; Natile, M. M.; *J. Eur. Ceram. Soc.*, **2016**,
<http://dx.doi.org/10.1016/j.jeurceramsoc.2016.10.017>
53. https://www.utwente.nl/tnw/ims/publication/downloads/CDC_Explained.pdf

APPENDIX A

EIS test

Program that calculates impedance through the use of a synthetic wave

```
% Programma per studiare l'analisi di impedenza via matlab
% su segnali sintetici

clear all
close all
clc

% Impostazione delle frequenze scansionate
fv = logspace(-2,6);          % sono potenze di 10
Nf = length(fv);

% scelta di quali modelli calcolare
%modelli=1:8;
modelli = 4

for model = modelli
% genera un'impedenza per un circuito modello
[Z,tit] = Impedenza(fv,model);

AV = 0.9;      % V, ampiezza perturbazione
V0 = 0;        % V, potenziale di base (verifica per V0>0)

% Ciclo di analisi per ogni frequenza da scansionare
for ifr = 1:Nf

% Generazione del segnale
f = fv(ifr)
% AV(ifr) = fittingMaxV(f);

T = 1/f ;
t = linspace(0, 3*T, 2^12)';      % FFT preferisce vettori lunghi 2^n
%
% figure(5)
% plot(1:ifr,AV(ifr),'-o')
% xlabel('Time, s'),legend('amp di V [V]')
% grid

w = 2*pi*fv(ifr);
V = V0 + AV*sin(w*t);
I = (V0 + AV*sin(w*t + angle(Z(ifr)))) / abs(Z(ifr));

figure(3)
plot(t,V,t,I)
xlabel('Time, s'),legend('V','I'),title(sprintf...
('%s Freq = %6.1f Hz',tit,f))
% figure(4)
% plot(V,I)
%xlim([-0.015 0.015]),ylim([-0.0005 0.0005]);
```

```

%xlim([xmin xmax]),ylim([ymin ymax]);
% hold on

% Analisi dei segnali per mezzo di freqrespmeasure.
% in questo caso i segnali in entrata sono quelli generati con yI e yV
% fittizi.
% In uscita fornisce modulo di Z, sfasamento, Z reale e immaginaria.

[ModZ, PhZ, ZRe, ZIm] = freqrespmeasure(I, V);

% Collezione i dati di ciascuna frequenza

    ModZv(ifr) = ModZ;
    PhZv(ifr) = PhZ;
    ZRev(ifr) = ZRe;
    ZImv(ifr) = -ZIm;

end

figure(2),set(2,'Position',[1 -149 1680 967])
subplot(131),plot(real(Z),-imag(Z),ZRev,-ZImv,'o','Linewidth',2)
xlabel('Re(Z)'),ylabel('-Im(Z)')
legend('original','from I, V')
xlim([-15 15])
ylim([-1 50])

subplot(132),loglog(fv,abs(Z),fv,abs(ZRev+j*ZImv),'o','Linewidth',2)
xlabel('freq'),ylabel('|Z|')
legend('original','from I, V')
title(tit)
xlim([-1 1e6])
ylim([-1 20])

%subplot(133),semilogx(fv,-
angle(Z)*360/2/pi,fv,PhZv*360/2/pi,'o','Linewidth',2)
subplot(133),semilogx(fv,-angle(Z),fv,PhZv,'o','Linewidth',2)
xlabel('freq'),ylabel('phase shift, deg')
legend('original','from I, V')
xlim([-1 1e6])
ylim([-0.2 1])

print('-dmeta',sprintf('N&B_mod%d',model))
end

```

freqrespmeasure

Program for wave data elaboration. Claculation of Z through the use of FFT using I and V waves.

```

function [Amp, Ph, Z_Re, Z_Im] = freqrespmeasure(x, y)

% function: [Amp, Ph] = freqrespmeasure(x, y)
% x - first signal in the time domain (corrente)

```

```

% y - second signal in the time domain (tensione)
% Amp - freq response amplitude
% Ph - freq response phase, rad

% Vist e Iist in forma di vettori colonna
% represent x as column-vector if it is not
if size(x, 2) > 1
    x = x';
end
% represent y as column-vector if it is not
if size(y, 2) > 1
    y = y';
end

% signals length
xlen = length(x);
ylen = length(y);

% window preparation
% comando da comprendere meglio
xwin = flattopwin(xlen, 'periodic');
ywin = flattopwin(ylen, 'periodic');

% define the coherent amplification of the window
Kx = sum(xwin)/xlen;
Ky = sum(ywin)/ylen;

% Dai segnali sinusoidali di V e I istantanei alle trasformate
% fft of the first signal
X = fft(x.*xwin);
% fft of the second signal
Y = fft(y.*ywin);

% INDICI identificati per mezzo della ricerca del massimo del modulo
della
% trasformata dei segnali. (metodo 2)
% spectral peaks detection
[~, indx] = max(abs(X));
[~, indy] = max(abs(Y));

% fprintf ( 1, ' %f %f\n', real ( X(indx)), imag ( X(indx)) )
% fprintf ( 1, ' %f %f\n', real ( Y(indy)), imag ( Y(indy)) )
% frequency response amplitude
Xamp = abs(X(indx))/xlen/Kx;
Yamp = abs(Y(indy))/ylen/Ky;
Amp = Yamp/Xamp; % METODO A: modulo di Z come rapporto tra trasformate

X1=conj(X(indx));
Z = (Y(indy)*X1)/(X(indx)*X1);
Z_Re = abs(real(Z));
Z_Im = abs(imag(Z));

% frequency response phase
Ph =(angle(Y(indy)) -angle(X(indx)));
end

```

Impedenza

Program that returns the impedance value of certain circuital elements as a vector of real and complex numbers.

```
function [Z, tit] = impedenza(f,tipo)

% restituisce l'impedenza di diversi circuiti elementari
% come vettore di numero eventualmente complessi

% paramteri per verifica con
% https://www.gamry.com/application-notes/EIS/basics-of-electrochemical-impedance-spectroscopy/
switch tipo
    case 1
        Rel=12; %Ohm
        Z=Rel * ones(size(f));
        tit='Resistor';
    case 2
        w=2*pi*f;
        C=9e-6; %F
        Z=1./j*C*w;
        tit='Capacitor';
    case 3
        w=2*pi*f;
        L=10e-6; %F
        Z=j*w*L;
        tit='Inductor';
    case 4
        w=2*pi*f;
        Rel=12; %Ohm
        Rct=100; %Ohm
        Cdl=9e-6; %F
        A=1/Rct;
        B=j*Cdl*w;
        Z=1./(A+B)+Rel;
        tit='Randles circuit';
    case 5
        Rel=500; %Ohm
        w=2*pi*f;
        C=200e-12; %F
        Z=1./j*C*w + Rel;
        tit='Purely Capacitive Coating (R+C in serie)';
    case 6
        WC=150; % Warburg coefficient (sigma)
        w=2*pi*f;
        Z=(1-j)*WC./sqrt(w);
        tit='Warburg Impedance (diffusion)';
    case 7
        WC=150; % Warburg coefficient (sigma)
        w=2*pi*f;
        Zd=(1-j)*WC./sqrt(w);
        Rs=20; %Ohm
        Rct=250; %Ohm
        Cdl=40e-6; %F
        A=1./(Rct+Zd);
        B=j*Cdl*w;
        Z=1./(A+B)+Rs;
        tit='mix kin & diff control';
```

```

case 8
    w=2*pi*f;
    Rs=20; %Ohm
    Cc=4e-9; %F
    Rpo=3400; %Ohm
    Rct=2500; %Ohm
    Cdl=4e-6; %F
    A1 = 1/Rct;
    B1 = j*Cdl*w;
    Z3 = 1./(A1+B1);
    Z2 = Rpo+Z3;
    A = 1./Z2;
    B = j*Cc*w;
    Z1 = 1./(A+B)
    Z=Z1+Rs;
    tit='Failed Coating';
case 9
    C=20;
    w=12*pi*f;
    a=0.6
    Z=1./(C*(j*w).^a);
    tit='Constant Phase Element';
case 10
    WC=150; % Warburg coefficient (sigma)
    w=2*pi*f;
    Zd=(1-j)*WC./sqrt(w);
    Rs=20; %Ohm
    Rct=250; %Ohm
    Cdl=40e-6; %F
    A=1./(Rct+Zd);
    B=(j*w).^a*Cdl;;
    Z=1./(A+B)+Rs;
    tit='Modified Randles Circuit';
end

Zr = real(Z);
Zi = imag(Z);

figure(100)
subplot(131),plot(Zr,-Zi)
xlabel('Re(Z)'),ylabel('-Im(Z)')

subplot(132),semilogx(f,abs(Z))
xlabel('freq'),ylabel('|Z|')
title(tit)

subplot(133),semilogx(f,-angle(Z)*360/2/pi)
xlabel('freq'),ylabel('phase shift, deg')

```

EIS measurement 1

Program that generates commands the wave generator in order to produce a wave and subsequently retrieves the I and V data generated by the load in order to calculate Z and compare it to an EEC model.

%Programma per studiare l'analisi di impedenza via matlab.

```

% Programma da utilizzare quando ho a disposizione un generatore d'onda
% non remotable. Come Agilent ---- in prestito dal DISC (Glisenti)
% Il programma imposta la comunicazione con il carico elettronico e ne
% setta i parametri.
% Il programma è impostato in modo da scansionare un set di frequenze
% chiamando la comunicazione con il generatore d'onda DDS-3X25 USB
% ARBITRARY FUNCTION GENERATOR.
% Il programma registra i segnali in uscita al load (diverse prove con
% presenza di circuito eq o di resistenza esterna + alimentatore).
% Il programma chiama poi la Function 'freqrespmeasure' che prosegue
con il calcolo
% dell'impedenza del "sistema di prova"
% Al termine del ciclo il programma genera un file .mat di dati per
% ciascuna frequenza scansionata.
% Per proseguire l'analisi in funzione della frequenza è necessario
% accoppiare l'uso di EIS_measure con la rielaborazione con EIS_exp2.

clear, clc, close all

% Create GPIB objects
% l = carico elettronico (load) Agilent N3300A
l = instrfind('Type', 'gpiib', 'BoardIndex', 7, 'PrimaryAddress', 5,
'Tag', '');

% Create the GPIB object if it does not exist
% otherwise use the object that was found.
% per l (load Agilent N3300A)
if isempty(l)
    l = gpib('AGILENT', 7, 5);
else
    fclose(l);
    l = l(1)
end

% Set Buffer load (per l)
BS = 2^15;
set(l, 'InputBufferSize', BS) % per raccogliere più dati in una query
di misure
disp(sprintf('InputBufferSize %d', get(l, 'InputBufferSize'))) % per
verifica

% Connect to instrument objects and clears the HW buffers
fopen(l); clrdevice(l); % connessione load e clear buffers

% Identification of the instrument object, function generator and
electronic load.
Connection2 = query(l, '*IDN?') % "chi sei?" al load

% load: reset del carico
fprintf(l, sprintf('CLEAR 705'))
fprintf(l, sprintf('ABORT '))
fprintf(l, sprintf('*RST'))
fprintf(l, sprintf('*RCL'))
fprintf(l, sprintf('CURRENT:PROTECTION:STATE ON '))

fprintf(l, sprintf('INITiate:IMMEDIATE'));
% fprintf(l, sprintf('TRIG:DEL 0.5'))
fprintf(l, sprintf('TRIG:SOUR BUS'))
fprintf(l, sprintf('TRIG:IMM'))

```



```

% Impostazioni di dati da usare nella generazione dell'onda
% measurement settings
fsout = 250000; %?
duration = 0.01;
% % preparation of the time vector
xlen = round(duration*fsout)
t = (0:xlen-1)/fsout;

% initialization
h = waitbar(0, 'Please wait...');

fv=[(1.9531:1.92531:9.7655), (19.5313:19.5313:78.1252), (97.6563:97.6563
:10000)];

Nf = length(fv);
Ncicli = 10;      % N di cicli da acquisire
Np = 2^11        % Numero di punti acquisiti nell'analisi

dtf = [(0.0005*ones(1,5)), (0.00005*ones(1,4)), (0.00001*ones(1,Nf-9))]

if Np>BS/2, disp('Input buffer forse insufficiente'),end

% LOAD AGILENT 33022A
% Impostazione dei parametri da settare al carico.
% Per le misure di impedenza il carico si imposta in modalità CC.
% In questo modo è stabilita la corrente che deve transitare attraverso
il
% carico, e quindi attraverso il sistema di analisi.
% Sulla base dei parametri dell'onda fornita dal generatore d'onda e
della
% corrente IL impostata al carico, viene generata una corrente
sinusoidale
% che attraversa il sistema (alla quale corrisponde a sua volta
% un'oscillazione sinusoidale sfasata della tensione).

    VL = 2;          % V, tensione al carico. Solo se si lavora in CV
(non in qst caso)
    IL = 0.015;     % A, corrente al carico. Se si lavora in CC
(questo caso)
    RI = 1          % Range di corrente [(1-3) = Range min, 3A]
    RV = 3          % Range di tensione [(1-7) = Range min, 6V]    %
fine parametri per l'analisi -----

% Settaggio parametri
fprintf(1, sprintf('INPUT ON'))          % predisporre il load
al carico dei parametri
fprintf(1, sprintf('SOURce:MODE CURR'))   % imposta modo current
(CC)
%fprintf(1, sprintf('SOURcce:MODE VOLT')) % imposta modo
voltage (CV)

% IMPORTANTE
% lavorando con tensioni e correnti basse è necessario impostare
range
% minimi. Bisogna impostare sia
% RANGE INGRESSO (SOUR)
% RANGE SENSIBILITÀ ACQUISIZIONE (SENS)

```

```

fprintf(l, sprintf('SOUR:CURR:RANG %f', RI)) % INGRESSO
fprintf(l, sprintf('SOUR:CURR:RANG MIN %f')) % ottengo lo stesso
%risultato della
riga sopra
fprintf(l, sprintf('SOUR:VOLT:RANG %f', RV)) % INGRESSO
fprintf(l, sprintf('SENS:VOLT:RANGE MIN %f')) % ACQUISIZIONE
fprintf(l, sprintf('SENS:CURR:RANGE MIN %f')) % ACQUISIZIONE
fprintf(l, sprintf('VOLT %f',VL)) % se si lavorasse in
CV
fprintf(l, sprintf('CURR %f',IL)) % corente settata al
carico in CC

% Per accertarsi che il load abbia registrato i parametri
interrogo lo
% strumento chiedendo a monitor le impostazioni che ha registrato.

%E = query(l, 'VOLT?'); disp(sprintf('Tensione al carico %5.3f
V',str2num(E))) % se si lavorasse in CV
I = query(l, 'CURR?'); disp(sprintf('Corrente al carico %5.3g
I',str2num(I)))
RangeI = query(l, 'CURR:RANGE?'); disp(sprintf('Current Full Scale
%5.3g A',str2num(RangeI)))
RangeV = query(l, 'VOLT:RANGE?'); disp(sprintf('Voltage Full Scale
%5.3g V',str2num(RangeV)))

%Inizializzazione serie vettori/matrici riempite ad ogni iterazione
Vfist = []; % preparazione matrice Vist
Ifist = []; % preparazione matrice Iist
ModZv = [];
PhZv = [];
ZRe = [];
ZIm = [];
Ph = [];
Zf = [];
model = 4
Np = 1024;
% Ciclo di analisi per ogni frequenza da scansionare
for ifr = 1:Nf
% Generazione del segnale
f = fv(ifr)
% Generazione del segnale
GenInit()
GenSin__Freq_Ampl_Ofs_Phi(f,0.02,0,0)

T = 1/f % s, periodo
% durata = Ncicli*T;
%dt = durata/Np(ifr);
%dt = durata/Np; % s, time period between measurement points.
% It can be from 0.00001 to 0.032 s
% in 10 microsecond increments.
% dt = 0.00005
dt = dtf(ifr);

if rem(dt,1e-5)>0, dt = fix(dt/1e-5)*1e-5,end
durata = dt*Np; % se dt non è multiplo di 10 us lo rende tale
%durata = dt*Np(ifr);
if Np>BS/2, disp('Input buffer forse insufficiente'),end

```

```

OFFs = 0.5;          % s, Specify a delay time from the start of the
trigger until the measurement is taken.
                    % pc: OFFs = 0*dt
fprintf(l, sprintf(...
'SENSE:SWEep:TINterval %f;POINTs %f;OFFset %f',dt,Np,OFFs)) %
verifica

% Inizio registrazione e misura delle onde di tensione e di corrente
che
% transitano nel sistema.
% con Vist e Iist si intendono le tensioni e le correnti istantanee,
cioè
% registarte al passare del tempo, per ciascuna frequenza scansionata

% set trigger
% fprintf(l, sprintf('INITiate:IMMediate')); % prova ad usarlo
interno al ciclo
% % fprintf(l, sprintf('TRIG:DEL 0.5'))
% fprintf(l, sprintf('TRIG:SOUR BUS'))
% fprintf(l, sprintf('TRIG:IMM'))

ci =
textscan(query(l, 'MEASure:ARRay:CURRent?'), '%f', 'Delimiter', ',');
%ci =
textscan(query(l, 'FETch:ARRay:CURRent?'), '%f', 'Delimiter', ',');
%v =
textscan(query(l, 'MEASure:ARRay:VOLTage?'), '%f', 'Delimiter', ',');
v = textscan(query(l, 'FETch:ARRay:VOLTage?'), '%f', 'Delimiter', ',');

Iist = ci{1};
mIist = Iist*1000; % Iist in mA

Vist = v{1};
mVist = Vist*1000; % Vist in mV

Nv = length(Vist);
Ni = length(Iist);
if Ni~=Np | Ni~=Np, disp(sprintf('N dati acq non coerente\n Nv=%d
Ni=%d Np=%d',Nv,Ni,Np)),end

t=(1:Nv)*dt;

% Vfist = [Vfist,Vist]; % colleziono i vettori di Vist in una
matrice Vfist, ogni colonna corrisponde ad una diversa frequenza
scansionata
% Ifist = [Ifist,Iist]; % colleziono i vettori di Iist in una
matrice Ifist, ogni colonna corrisponde ad una diversa frequenza
scansionata
%

% IMPEDENZA DA TEORIA CIRCUITALE
[Z,tit] = Impedenza(f,model);
Zf =[Zf,Z];

% FITTING DATI SPERIMENTALI
mV=Vist-mean(Vist);
mI=Iist-mean(Iist);
[pksV,locsV] = findpeaks(Vist); % identifica tutti i picchi del
vettore tensioni

```

```

indyV = locsV(3); % sceglie il 3 picco come riferimento per indy
tV = t(indyV);
% tiene solo 3 periodi
ton = t < 3*T;
tf = t(ton);
mV = mV(ton);
mI = mI(ton);

fV = fit(tf',mV,'sin1');
fI = fit(tf',mI,'sin1');
Vpar(ifr,:) = coeffvalues(fV);

w = 2*pi*f;
AVin = 0.1;
Vin = AVin*sin(w*tf);
% ricalcola i dati exp interpolando su una ascissa più fitta
t1 = linspace(min(tf),max(tf),2^11);
Ifit = feval(fI,t1);
cfI = coeffvalues(fI);
phiI = cfI(3);
Vfit = feval(fV,t1);
cfV = coeffvalues(fV);
phiV = cfV(3);
ph = phiV-phiI ;
Ph = [Ph,ph];

% Analisi dei segnali per mezzo di freqrespmeasure.
% in questo caso i segnali in entrata sono Vist e Iist misurati dal
carico.
% In uscita fornisce modulo di Z,sfasamento,Z reale e immaginaria.

[ModZ, PhZ, Z_Re, Z_Im] = freqrespmeasure(Ifit, Vfit);
%[ModZ, PhZ, Z_Re, Z_Im] = freqrespmeasure(Iist, Vist);
ModZv(ifr) = ModZ;
PhZv(ifr) = PhZ;
ZRe(ifr) = -Z_Re;
ZIm(ifr) = Z_Im;

% Tensioni e Correnti sinusoidali (istantanee)
figure(1)
subplot(2, 1, 1)
plot(t, Vist,'r', 'LineWidth', 2)
grid on
%xlim([0 0.008]);
%ylim ([]);
set(gca, 'FontName', 'Times New Roman', 'FontSize', 14)
xlabel('Time, s')
ylabel('Vist, V')
title('Voltage and Current Wave response')
grid on

subplot(2, 1, 2)
plot(t, Iist,'b', 'LineWidth', 2)
grid on
%xlim([0 0.008]);
%ylim ([]);
set(gca, 'FontName', 'Times New Roman', 'FontSize', 14)
xlabel('Time, s')
ylabel('Iist, A')

```

```

grid on

filename = [ 'Nome' num2str(f) '.mat' ];
save(filename);
pause(3)

end

disp 'fine analisi'
GenInit()
GenSin__Freq_Ampl_Ofs_Phi(10,0,0,0)
GenClose

figure
subplot(131),plot(real(Zf),-imag(Zf),'-+',ZRe,ZIm,'-o','Linewidth',2)
xlabel('Re(Z)'),ylabel('-Im(Z)')
legend('Calculated','Exp')
xlim([-15 150])
ylim([-10 60])

subplot(132),semilogx(fv,abs(Zf),'-+',fv,abs(ZRe+j*ZIm),'-
o','Linewidth',2)
xlabel('freq'),ylabel('|Z|')
ylim([-1 120]);
legend('Calculated','Exp')

subplot(133),semilogx(fv,PhZv,'-o','Linewidth',2)
xlabel('freq'),ylabel('phase shift')
ylim([-2 2])

```

Model

Program for the fitting of the SOFC data

```

% Programma per studiare l'analisi di impedenza via matlab
% su segnali sintetici

clear all
close all
clc

% Impostazione delle frequenze scansionate
fv = logspace(-2,6);          % sono potenze di 10
Nf = length(fv);

% scelta di quali modelli calcolare
%modelli=1:8;
modelli = 7

for model = modelli
% genera un'impedenza per un circuito modello
[Z,tit] = Impedenza(fv,model);

AV = 0.9;          % V, ampiezza perturbazione
V0 = 0;           % V, potenziale di base (verifica per V0>0)

% Ciclo di analisi per ogni frequenza da scansionare

```

```

for ifr = 1:Nf

% Generazione del segnale
f = fv(ifr)
% AV(ifr) = fittingMaxV(f);

T = 1/f ;
t = linspace(0, 3*T, 2^12)';          % FFT preferisce vettori lunghi 2^n
%
% figure(5)
% plot(1:ifr,AV(ifr),'-o')
% xlabel('Time, s'),legend('amp di V [V]')
% grid

load(strcat('C:\Users\gisel\Desktop\tesis\Impedenza\BEC6\620_10_0005')
)
theta=theta*0.0174533;

end

% figure(2),set(2,'Position',[1 -149 1680 967])
subplot(131),plot(real(Z),-imag(Z),Z_Re,-Z_Im,'o','Linewidth',2)
xlabel('Re(Z)'),ylabel('-Im(Z)')
legend('calc','exp')

subplot(132),semilogx(fv,abs(Z),freq,Z_mod,'o','Linewidth',2)
xlabel('freq'),ylabel('|Z|')
legend('calc','exp')

%subplot(133),semilogx(fv,-
angle(Z)*360/2/pi,fv,PhZv*360/2/pi,'o','Linewidth',2)
subplot(133),semilogx(fv,-angle(Z),freq,-theta,'o','Linewidth',2)
xlabel('freq'),ylabel('phase shift, deg')
legend('calc','exp')

print('-dmeta',sprintf('N&B_mod%d',model))
end

```